

REPORT DOCUMENTATION PAGE			Form Approved OMB No. 0704-0188		
Public reporting burden for this collection of information is estimated to average 1 hour per response, including the time for reviewing instructions, searching existing data sources, gathering and maintaining the data needed, and completing and reviewing this collection of information. Send comments regarding this burden estimate or any other aspect of this collection of information, including suggestions for reducing this burden to Department of Defense, Washington Headquarters Services, Directorate for Information Operations and Reports (0704-0188), 1215 Jefferson Davis Highway, Suite 1204, Arlington, VA 22202-4302. Respondents should be aware that notwithstanding any other provision of law, no person shall be subject to any penalty for failing to comply with a collection of information if it does not display a currently valid OMB control number. <b>PLEASE DO NOT RETURN YOUR FORM TO THE ABOVE ADDRESS.</b>					
1. REPORT DATE (DD-MM-YYYY) May 11, 2012		2. REPORT TYPE Final Report		3. DATES COVERED (From - To) May 1, 2006 - Dec. 31, 2011	
4. TITLE AND SUBTITLE  Final Report to AFOSR DURIP (FA9550-06-1-0326) On "Energy Harvesting and Storage Systems for Future AF Vehicles"			5a. CONTRACT NUMBER		
			5b. GRANT NUMBER FA 9550-06-01-0326		
			5c. PROGRAM ELEMENT NUMBER		
6. AUTHOR(S) University of Washington: Minoru Taya (PI), Co-PIs: S. Jenekhe, G. Cao, P. Feraboli,, Y. Kuga, C.Xu, University of Colorado: M. Dunn, K. Maute, R. Yang. SH Lee, UCLA: S.Ju and T. Hahn, Virginia Tech: D. Inman, and University of Illinois at UC, I. Chasiotis			5d. PROJECT NUMBER		
			5e. TASK NUMBER		
			5f. WORK UNIT NUMBER		
7. PERFORMING ORGANIZATION NAME(S) AND ADDRESS(ES) University of Washington, Department of Mechanical Engineering Box 352600, Seattle, WA 98195-2600			8. PERFORMING ORGANIZATION REPORT NUMBER		
9. SPONSORING / MONITORING AGENCY NAME(S) AND ADDRESS(ES) AFOSR Dr. B. L. ("Les") Lee, 875 Raondolph , Suite 325, Arlington, VA 22203-1768			10. SPONSOR/MONITOR'S ACRONYM(S)		
			11. SPONSOR/MONITOR'S REPORT NUMBER(S) <i>AFRL-AFOSR-VA-TR-2016-0612</i>		
12. DISTRIBUTION / AVAILABILITY STATEMENT unlimited					
13. SUPPLEMENTARY NOTES					
14. ABSTRACT  This MURI project is aimed at designing a set of new energy-harvesting and storage materials (EHSM) and their integration of load-bearing airborne structures. The EHSM that were covered are, (i) organic solar cells based on two designs ,(a) dye-sensitized solar cells (DSSC) and (b) solid state semi-conductor polymer based solar cells(SSSPS), (ii) thermoelectric materials and modules, (iii) piezoelectrics and (iv) electromagnetic generator. This MURI team is composed of several universities, University of Washington (UW) , University of Colorado(CU), UCLA, Virginia Tech(VT) and University of Illinois(UI) at UC. UW team covers energy-harvesting and storage materials, and their integration to structures and supportive electric system, CU covers mainly the hierarchical modeling of EHSM, VT covers the multi-mode energy-harvesting system, UCLA covers mainly the integration of EHSS into load-bearing structures. Finally UI covers the micro-characterization of integrated EHSM into structures.					
15. SUBJECT TERMS					
16. SECURITY CLASSIFICATION OF: unclassified			17. LIMITATION OF ABSTRACT	18. NUMBER OF PAGES  130	19a. NAME OF RESPONSIBLE PERSON Minoru Taya
a. REPORT	b. ABSTRACT	c. THIS PAGE			19b. TELEPHONE NUMBER (include area code) 206-685-2850 , <i>tayam@uw.edu</i>

**Final Report to AFOSR DURIP (FA9550-06-1-0326)  
On “Energy Harvesting and Storage Systems for Future AF Vehicles”**

**For the period of May 1, 2006 – December 31, 2011**



**Principal Investigator: Minoru Taya, Director**  
**Boeing-Pennell Professor**  
**Center for Intelligent Materials and Systems**  
**Department of Mechanical Engineering**  
**University of Washington, Box 352600**  
**Seattle, WA 98195-2600**  
**Phone: 206-685-2850, Fax: 206-685-8047**  
**Email: [tayam@u.washington.edu](mailto:tayam@u.washington.edu)**

**CO-PIs :**

**University of Washington : Sam Jenekhe, Chunye Xu, Gouzong Cao, Yasuo Kuga and Paolo Feraboli**

**University of Colorado: Martin Dunn, Kurt Maute and Ronggui Yang, and SeeHee Lee**

**University of California at Los Angeles: Sungtaek Ju and Thomas Hahn**

**Virginia Tech: Dan Inman**

**University of Illinois at Urbana-Champaign: Ioannis Chasiotis**



**May 11, 2012**



## Executive Summary

This MURI project is aimed at designing a set of new energy-harvesting and storage materials (EHSM) and their integration of load-bearing airborne structures. The EHSM that were covered are, (i) organic solar cells based on two designs, (a) dye-sensitized solar cells (DSSC) and (b) solid state semi-conductor polymer based solar cells (SSSPS), (ii) thermoelectric materials and modules, (iii) piezoelectric materials and (iv) electromagnetic generator.

Research on organic solar cells is still in its infant stage and the power conversion efficiency (PCE) of those is still lower than the commercial Si based solar cells. But the cost and weight of the organic solar cells are lower, thus, providing a good potential for airborne energy-harvesting materials. Jenekhe designed selected SSSPS with PCE being close to 5% while Taya and Cao groups designed DSSC with PCE of 7-10% for liquid base electrolyte, and PCE of 5-6% for gel electrolyte. The DSSC designed by Taya group has two versions; one based on thin glass substrate, the other based on polymer substrate, the PCE of the former with gel electrolyte is 7%, while that based on PET substrate is 5%. Cao group focused on the designing nanostructured nanoparticles with aim of increasing PCE.

Taya group designed new thermoelectric materials based on low-cost and low-weight TE materials, i.e  $\text{Mg}_2\text{Si}$  and  $\text{MnSi}$  for use in the intermediate temperature range, thus higher specific figure-of-merit ( $ZT/\rho$ , where  $ZT$  is the figure-of-merit,  $\rho$  is density) while they used  $\text{BiTe}$  for lower temperature range and assembled segmented TE module whose power density is  $0.75 \text{ W/cm}^2$ . Ju designed thermal switch by which the heat flow can be controlled for more enhanced or more retarded flow control. Feraboli group at UW studied extensively the processing and characterization of the battery and thin film solar cells integrated in composite panels. The results of the Feraboli's group are complimentary to those of Hahn's group work at UCLA.

Hahn group studied experimentally the durability of commercial EHSM embedded in structural composite panels which are subjected cyclic bending, then measured the residual performance of solar cells and Li-ion battery film.

Inman designed a set of new energy-harvesting and storage systems (EHSS) integrated in structural composite panels while the main emphasis was on the mechanical energy harvesting based on piezoelectric and also magnetic system of Faraday principle.

University of Colorado (CU) team made multi-scale modeling and design optimization of EHSM; (i) Electrochemical modeling, (ii) Nano-scale heat propagation model, (iii) optimal design of piezoelectric energy harvesting systems and (iv) UAV test bed design. CU team also studied experimentally the optimum cathodic material of Li-ion battery.

University of Illinois at Urbana-Champaign made micro-characterization of the damages observed in the integrated EHSM components.

The subjects covered by this MURI team are extensive, spanning over nanostructured airborne energy-harvesting and storage materials and their devices, their integration into load-bearing structures. Due to this broad-band research area under the five-year period, we strongly feel that several more research subjects remain to be performed in the near future. They include (i) integration of a thermal energy-harvester into a UAV combustion chamber and (ii) integration of airborne sensors, actuators, energy-harvester and battery systems into a single cohesive system that can be durable under thermo-mechanical use loading.

## Table of Contents

	pages
Chapter 1: Introduction.....	1
Chapter 2: Achievements of various tasks.....	2
Task A: Design Tools for Multifunctional Materials and Structures..... (Dunn, Maute and Yang)	2
Task B: Energy Harvesters based on thermoelectrics ..... (Taya , Yang and Ju)	14
Task C: Energy harvester based on polymer solar cells ..... (Jenekhe , Taya, Cao, Xu)	38
Task D: Integrated EHSM components in load-bearing structures..... (Ju, Hahn, Feraboli and Chasiotis)	52
Task E: Design of Energy Storage System..... (Cao, Taya, Kuga, Xu, Lee)	103
Task F: Electric System Design ..... (Kuga)	109
Task G: Multimode Energy Harvesting for ISR/MAV Missions ..... (Inman)	111
Chapter 3: List of personnel supported by this MURI grant.....	115
Chapter 4: List of publications under this MURI grants.....	116
Chapter 5: Interactions with DoD labs and industry.....	123
Chapter 6: Honors/awards.....	123
Chapter 7: References.....	124



## Chapter 1: Introduction

This annual report covers the progress made on our MURI for the period of May 1, 2006 – December 31, 2011, and covers on the following subject areas,

- Task A. Design Tools for Multifunctional Materials and Structures (Dunn, Maute and Yang)
- Task B. Energy Harvesters based on thermoelectrics (Taya and Yang)
- Task C. Energy harvester based on polymer solar cells (Jenekhe, Taya, Cao, Xu)
- Task D. Integrated EHSS components in load-bearing structures (Ju, Hahn, Feraboli and Chasiotis)
- Task E. Design of Energy Storage System (Cao, Taya, Kuga, Lee and Xu)
- Task F. Electric System Design (Kuga)
- Task G. Multimode Energy Harvesting for ISR/MAV Missions (Inman)

Table 1 shows all the tasks that were performed by the above PI and Co-PIs

Group Names	PI, Co-PIs	Year 1	Year 2	Year 3	Year 4	Year 5
UW	Taya Kuga Xu Cao Jenekhe Feraboli	----- ----- ----- ----- -----	----- ----- ----- ----- -----	----- ----- ----- ----- -----	----- ----- ----- ----- -----	----- ----- ----- ----- -----
CU	Dunn Maute Yang Lee	----- ----- ----- -----	----- ----- ----- -----	----- ----- ----- -----	----- ----- ----- -----	----- ----- ----- -----
VT	Inman	-----	-----	-----	-----	-----
UI-UC	Chasiotis	-----	-----	-----	-----	-----

Table 1. The periods of PI and Co-PIs working for this MURI project

The semi-detailed statements of the above tasks are given in the following pages.

## **Chapter 2: Achievements of various tasks**

### **Task A: Multi-scale Modeling and Design Optimization of EHSS (Dunn, Maute and Yang)**

#### **Objective:**

Conventionally, batteries are designed to provide a single function: to store energy. The battery cell is shielded from mechanical loads by enclosure in a stiff containment and the integration of batteries into structural components, subsystems, and devices is mainly driven by thermal management requirements. Integrating batteries in the load bearing structure of small air vehicles is a promising concept to reduce the weight and storage volume requirement for on-board energy storage systems. The goal of this research thrust was to develop an in-depth understanding of mechanical phenomena in Li-ion batteries across multiple length scales. This insight enables the rigorous design of multi-functional battery architectures, using formal optimization approaches. CU team studied also three more sub-tasks, (i) nano-scale heat propagation model, (ii) optimal design of piezoelectric energy harvesting system, and (iii) UAV test bed design.

#### **A1. Introduction**

This report summarizes the research conducted by the co-PIs Dunn, Maute and Yang under the MURI-EHSS grant at the University of Colorado. The research focused on the development of design tools for advanced energy harvesting and storage materials and the development of a UAV test bed which allows assessing the system-level performance of the EHSS materials and devices. The work on analysis and design methods for advanced EHS materials was concerned with:

- Electrochemical modeling
- Nano-scale heat propagation model
- Optimal Design of Piezoelectric Energy Harvesting Systems
- UAV Test Bed design

#### **A2. Electrochemical modeling**

Integrating batteries in the load bearing structures requires to model batteries as “material”. To evaluate the electro-chemical and the mechanical performance of such materials we have developed a computational simulation framework that couples electro-chemical and mechanical models and applied it to the analysis of a representative unit-cell.

##### *Electro-chemical model and mechanical coupling*

We consider a simple layout similar to a typical Li-ion battery, that is, a separator, or electrolyte, and a cathode. For the sake of simplicity and as a first step, we ignore the effects of time in the model and solve the steady-state equations. Since we are also interested in the mechanical performance of the system, we model electrochemical stresses resulting from the diffusion of the metal Li into the porous cathode structure. This is a one-way coupling, from electrochemistry to mechanical performance.



In an electrolyte part, we are solving the following non-linear diffusion equations:

$$D_e \nabla^2 c_{Li^+} + \frac{D_e F c_{Li^+}}{RT} \nabla^2 \Phi_{Li^+} = 0$$

$$\frac{D_e F c_{Li^+}}{RT} \nabla^2 c_{Li^+} + \kappa_e \nabla^2 \Phi_{Li^+} = 0$$

where  $c_{Li^+}$  is the concentration of Li-ions in the electrolyte,  $\Phi_{Li^+}$  is the electrical potential in the electrolyte,  $D_e$  and  $\kappa_e$  are the diffusivity and the conductivity of the electrolyte, respectively.  $F$ ,  $R$ , and  $T$  are Faraday constant, universal gas constant, and temperature, respectively.

Within the cathode, the electric conduction is decoupled from the (neutral) Li diffusion:

$$D_c \nabla^2 c_{Li} = 0$$

$$\kappa_c \nabla^2 \Phi_{e^-} = 0$$

where  $D_c$ ,  $\kappa_c$  are the diffusivity and the conductivity of the cathode,  $c_{Li}$  is the concentration of the metallic lithium in the cathode, and  $\Phi_{e^-}$  is the electrical potential in the cathode.

“Global” boundary conditions, that is, the conditions on the “outer boundary” of the computational domain are of no critical importance, and are chosen rather arbitrarily so far. For example, on certain boundaries we prescribe  $Li^+$  concentrations, potentials,  $Li^+$  inflows,  $e^-$  inflows, or periodic boundary conditions. “Local,” or electrolyte/cathode interface conditions, are much more important since they determine the electrode kinetics. This part of the model will be refined in the future. The interface dynamics is modeled using the Butler-Volmer relations, which impose the continuity of mass/charge fluxes across the interface; that is no sources or sinks on the boundary. The fluxes depend on the local concentrations of species near the boundary, and some empirical material properties. Namely,

$$i = i_0 \left[ \exp\left(\frac{\alpha_a F}{RT} \eta_s\right) - \exp\left(-\frac{\alpha_c F}{RT} \eta_s\right) \right]$$

where  $i_0$  is the exchange current density,  $\eta_s$  is the surface overpotential, and  $\alpha_a$  and  $\alpha_c$  are respectively empirical anodic and cathodic constants. In our model, we use  $\alpha_a = \alpha_c = 0.5$ ,  $\eta_s = \text{constant}$ . The appropriateness of the choice of these values remains to be verified. The exchange current density is computed by

$$i_0 = k_r (c_{lim} - c_{Li})^{\alpha_a} c_{Li}^{\alpha_c},$$

where  $c_{lim}$  is the limiting Li concentration, and  $k_r$  is the reaction rate ( $5e-7$ [m/s]).

Finally, everywhere in the domain the “usual” linear elasticity equations are solved. In the cathode part, they are coupled to the concentration of Li via electrochemically induced strains:

$$\varepsilon_{ec} = \beta(c_{Li} - c_0) / c_{lim},$$

where  $\varepsilon_{ec}$  is the electrochemically induced strain,  $\beta$  is a material dependent Vegard coefficient, and  $c_0$  is the strain-free Li concentration.

*Unit cell analysis* is the concentration of Li-ions in the electrolyte,  $\Phi_{Li+}$

We apply the above model to the analysis of a 3-D unit cell and consider a 3D cube aligned with coordinate axes. Periodic boundary conditions are imposed in  $y$  and  $z$  directions. The cube is divided into two subdomains, representing the electrolyte and cathode. At  $\mathbf{x}=\mathbf{0}$  we prescribe the inflow of Li-ions in the electrolyte part [thus, Neumann b.c. on  $c_{Li+}$  and  $\Phi_{Li+}$ ] and concentration of metal Li and electric potential in the cathode [Dirichlet b.c. for  $c_{Li}$  and  $\Phi_e$ ]. At  $\mathbf{x}=\mathbf{H}$  we prescribe concentration of  $Li+$  and electric potential in the electrolyte [Dirichlet b.c. for  $c_{Li+}$  and  $\Phi_{Li+}$ ], and concentration of metal Li and electric current in the cathode [Dirichlet b.c. for  $c_{Li}$  and Neumann b.c. for  $\Phi_e$ ]. The considered geometry and computational results are displayed below:

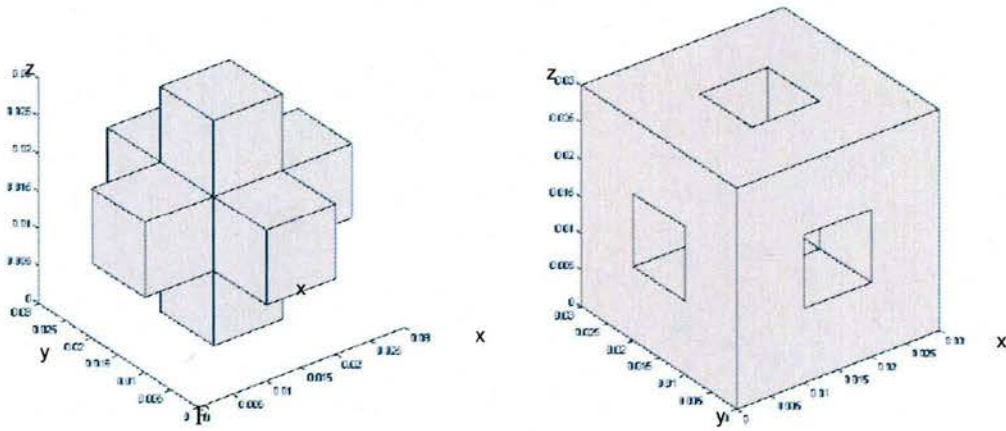


Figure A1. Computational domain. Left: cathode; right: electrolyte.

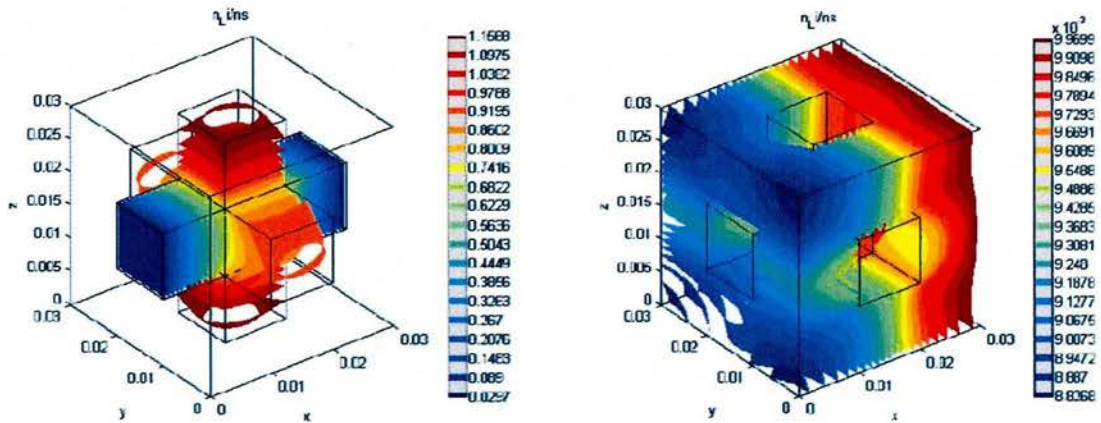




Figure A2. Concentration of Lithium. Left: cathode; right: electrolyte.

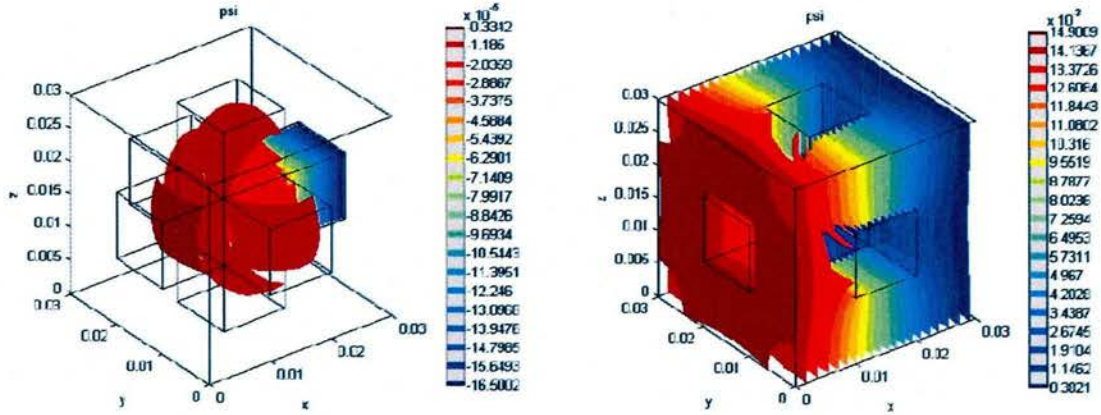


Figure A3. Electric potentials. Left: cathode; right: electrolyte.

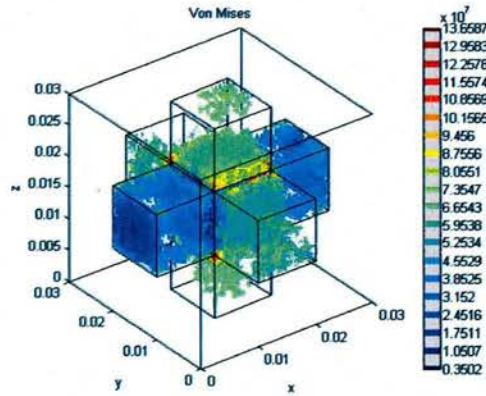


Figure A4. Von Mises stress distribution in the electrode.

We developed a multi-scale finite element model of lithium batteries to study electrochemical-mechanical interaction phenomena at macro and micro scales. We developed a multi-scale approach to analyze the surface kinetics and electrochemical-mechanical phenomena within a single spherical particle of the active material. Homogenization techniques relate parameters in the micro-scale particle model to those in the macro-scale model describing the lithium ion transport, electric potentials and mechanical response based on porous electrode theory. At the macro-scale, we have extended Doyle and Newman's electrochemical porous electrode model to account for elastic deformations. At the micro-scale we have accounted for differences in  $\text{Li}^+$  ion flux into the particles due to interfacial surface conditions using the Butler-Volmer equation and for surface pressures exerted on the particles by the composite electrode matrix. We have introduced a meso-scale aggregate model to relate micro- and macro-scale mechanical effects. This model was implemented into a finite element framework and used to study the influence of loading and design parameters on the electrochemical and mechanical response of the battery cell. The macro- and micro-scale models are discretized in time by an implicit Euler backward

scheme and in space by a Galerkin finite element method. The nonlinear macro- and micro-scale subproblems are solved by Newton's method using analytically derived Jacobians.

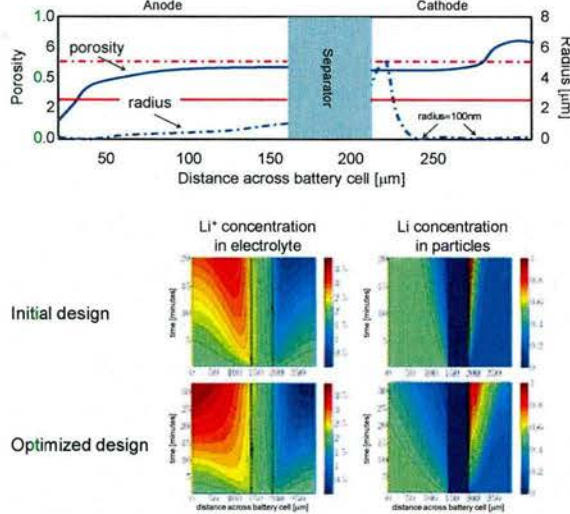


Fig. A5 Maximizing the useable energy density of a Li-ion cell for given discharge rate: The top figure shows the layout of the initial and optimally graded electrodes, varying the porosity, i.e. electrolyte volume fraction, and the size of the active particles across anode and cathode. The plots at the bottom show the Li-ion and Li concentrations in the electrolyte and active particles. This example is for a rather high discharge rate which leads to a poor Li intercalation into the active particles for the uniform porosity and size design. The optimized layout allows for a significantly better utilization of the active material.

To improve the energy and power density of the battery cell we integrated the above multi-scale model into a computational framework for optimizing the layout of electrodes. A key component of the optimization methodology was the formulation of the adjoint sensitivity equations of the multi-scale battery model. The efficient solution of the adjoint equations relies on the decomposition of the multi-scale problem into multiple, computationally small problems associated with the individual realizations of the micro-scale model. This decomposition method was shown to significantly reduce the computational time needed for sensitivity analysis versus numerical finite differencing. The potential of the proposed optimization framework was illustrated with numerical problems involving both macro- and micro-scale performance criteria and design variables. The usable capacity of a lithium ion battery cell was maximized while limiting the stress level in the electrode particles through manipulation of the local porosities and particle radii. We further applied to this optimization framework to tailor the electrode layout to specific energy versus power requirements.

### Accomplishments/New findings

We expanded multi-scale battery models to account for external mechanical loading; we developed a mathematically rigorous computational optimization approach to systematically design the layout of electrodes in multi-functional batteries.

We found that the load bearing capacity of Li-ion batteries is negligible if liquid electrolytes are used but can be significantly improved using an all solid-state architecture; we found that the stresses generated through intercalation of Li into active materials dominates over the ones generated by reasonable levels of external loading; we found that functionally grading electrodes is an efficient approach to optimize both the power and energy density of electrodes and to tailor the power-density behavior to particular application scenarios.

### A3. Nano-scale heat propagation model



At sub-micro- and nano-scales the Fourier's law of heat conduction is no longer valid. This is not especially surprising considering the fact that the Fourier relation between the temperature and heat flux is empirical and is not based on any sound physical principles. Therefore, we resort to modeling heat conduction using statistical mechanics principles, in which we consider statistical properties of heat carriers, such as the electrons and phonons. As a first step in this direction, we have chosen the simplest possible kinetic model, namely, the gray body model. Under the gray body assumption, the only heat carriers considered are the acoustic phonons.

#### *Nano-scale optimal design*

In order to evaluate the potential of using the phonon Boltzmann equation for the purpose of the nano-scale optimal design, we have implemented a pilot numerical simulation code using rapid prototyping packages MatLab and Comsol Multiphysics. Given the boundary heat fluxes, we distribute two given materials in a prescribed control volume in order to minimize a desired performance functional. In our preliminary study we have chosen to maximize the temperature difference between two points; one may for example envision attaching a thermo-electric material at these points, thus maximizing the electric output of the system.

#### *Numerical tests*

Importance of the phase space resolution: Many works on nano-scale heat propagation employ the lattice Boltzmann method (LBM) as an underlying numerical scheme for solving the underlying governing Boltzmann equations. The lattice Boltzmann method is a finite-difference type scheme, in which the velocity space discretization is fixed and is determined by the topology of the considered lattice. In our numerical experiments we found out that proper discretization of the velocity space is essential for obtaining well resolved solutions, and that numerical solutions generated by LBM generally suffer from non-symmetries due to the existence of "dedicated" non-physical space directions aligned with lattice directions. To illustrate this, we have performed the following experiment. A point heat source was placed in a square piece of Si. We solved the problem on a sequence of finite element discretizations, keeping the spatial discretization fixed while increasing the resolution of the velocity space discretization (see Figures A6, A7). One can clearly see gradually improving quality of the temperature resolution.

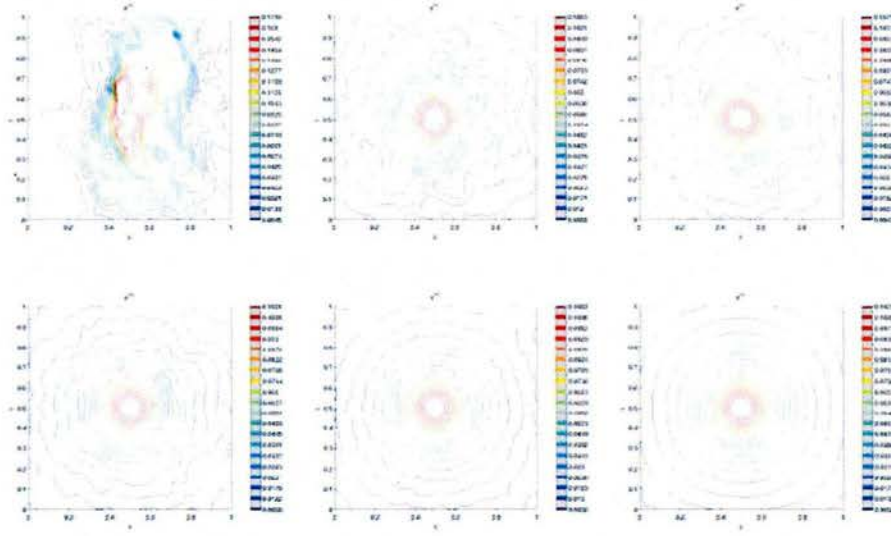


Figure A6. Importance of the proper velocity space resolution: temperature fields.

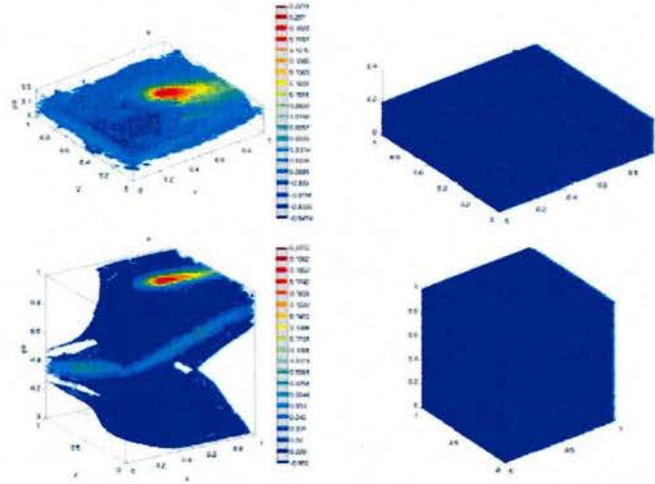


Figure A7. Importance of the proper velocity space resolution: phase space view.

**Length-scale effects:** To justify the computational costs associated with solving the multi-dimensional integro-differential equations, we perform the following numerical experiment. We model a square piece of Si with a square SiO inclusion, heated on the left-hand side. We solve the problem for three different length-scales of the domain:  $10\mu\text{m} \times 10\mu\text{m}$ ,  $1\mu\text{m} \times 1\mu\text{m}$ , and  $300\text{nm} \times 300\text{nm}$ . Assuming the phonon mean-free path in Si is of the order  $300\text{nm}$ , we span multiple heat propagation regimes, namely diffusive (Fourier), transient, and ballistic. We simulate the problem using the standard continuum mechanics steady state heat conduction equations, and steady state gray body phonon Boltzmann equations. As expected, continuum mechanics equations do not “see” the length-scale changes, whereas the Boltzmann equation



starts to capture small-scale phenomena (such as the temperature slip, shading, reflections), see Figure A8.

**Preliminary optimization results:** In order to evaluate the potential of using the phonon Boltzmann equation for the purpose of the nano-scale optimal design, we have implemented a pilot numerical simulation code using rapid prototyping packages MatLab and Comsol Multiphysics. Given the heat fluxes, we distribute two given materials (Si and Ge) in order to minimize a desired performance functional. In our preliminary study we have chosen to maximize the temperature difference between two points; one may for example envision attaching a thermo-electric material at these points, thus maximizing the electric output of the system.

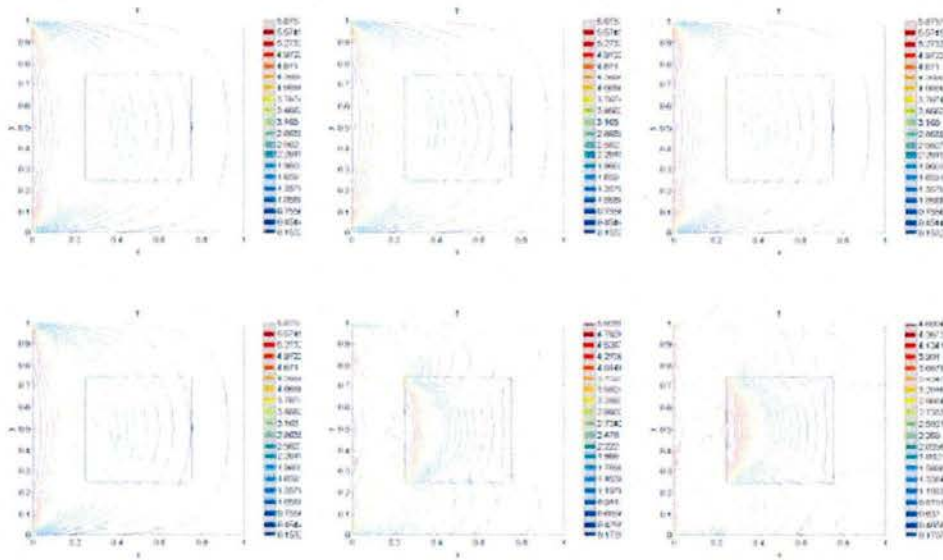


Figure A8. Length-scale effects: square piece of Si with SiO<sub>2</sub> inclusion, heated on the right side. Temperature isolines are shown. Upper row: continuum mechanics modeling; lower row: gray body phonon Boltzmann equation. Domain size: left column: 10μm x 10μm; center column: 1μm x 1μm; right column: 300nm x 300nm.

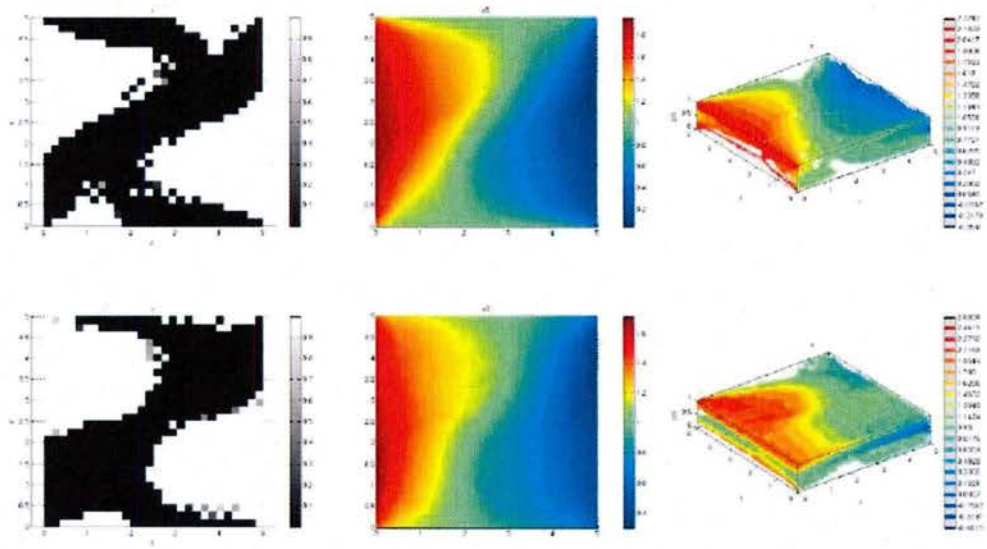


Figure A9. Preliminary optimization results: maximizing the temperature difference between two points in the computational domain with heated left side by distributing two materials (Ge and Si). Top row:  $10\mu\text{m} \times 10\mu\text{m}$  domain; bottom row:  $1\mu\text{m} \times 1\mu\text{m}$  domain; left column: optimal material distribution (black: Ge, white: Si), center column: optimal temperature fields; right column: phase space view of phonon energy density.



#### A4. Optimal Design of Piezoelectric Energy Harvesting Systems

##### Objective:

There is substantial promise in the use of piezoelectric energy harvesting systems to power electronics and devices through the conversion of ambient vibrations into electrical energy. Accurately predicting the energy harvesting capability in these systems is of paramount importance as the harvesting structure and the associated circuit must be “tuned” in concert to the signature of the ambient vibrations. To this end, our objectives were to develop modeling, simulation, and computational design approaches for piezoelectric energy harvesting systems, with goals of: i) exploiting the properties and layout of piezoelectric energy harvesting elements embedded within or mounted on a composite structure, and ii) incorporating a faithful representation of the nonlinear electrical circuit.

##### Brief summary of the CU team progress toward the above objectives

We successfully developed: i) a computational approach to analyze and design piezoelectric energy harvesting systems composed of layered plates and shells connected to an electrical circuit; ii) an approach to simulate the response of realistic nonlinear energy harvesting circuits that can be coupled with a computational design approach, and iii) a new approach to harvest mechanical energy from propagating waves.

##### Accomplishments/New findings

We used the finite element method to model the coupled electromechanics of the piezo-electric harvesting structure and a lumped parameter model for the dynamics of the electrical circuit. We assumed the harvester is subjected to a prescribed harmonic base excitation and that the structural and electrical responses are linear. We developed a topology optimization approach to design the layout of a multilayer structure consisting of structural, piezoelectric, and electrode layers, as well as the electrical circuit. The flexibility of our formalism admits the definition of specific system-level objectives, e.g., maximize the power harvested, in an algebraic fashion. In Rupp et al. (2009) we describe our analysis and design approaches in detail and present examples that demonstrate the versatility of our approach and show how it can be used to explore general behavior of and to develop overarching design principles for piezoelectric energy harvesting devices. For an objective of maximizing the power harvested, we investigated: (i) optimal designs for various piezoelectric to substrate thickness ratios, (ii) the effect of mass loading on optimal design, and (iii) the sensitivity of designs to shape variations. Figure A10 shows an example of a basic problem setup and Fig. A11 shows results.

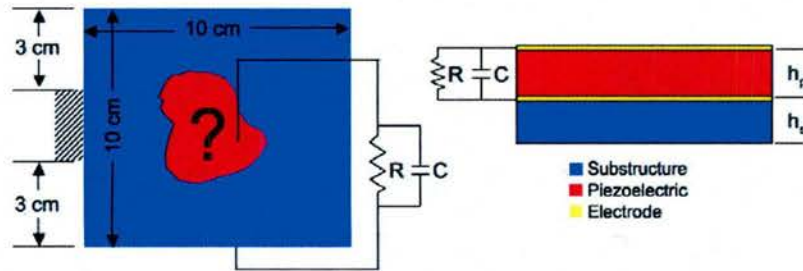


Figure A10. Design problem setup of a square plate subject to harmonic loading.

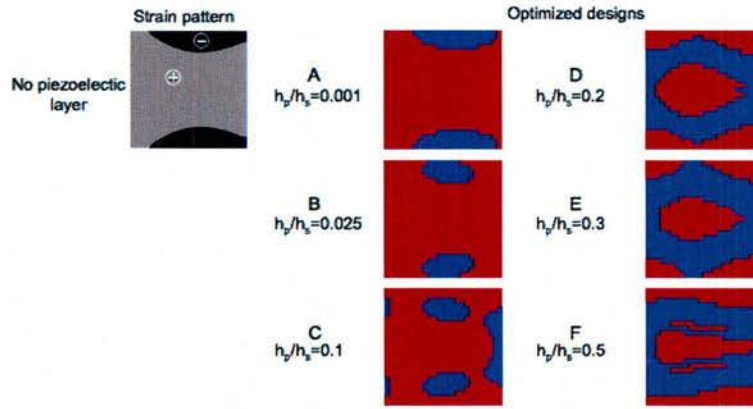


Fig. A11. Comparison of the strain pattern for a plate without a piezoelectric layer with optimal distribution of piezoelectric material (red) on an aluminum substrate (blue) for six different ratios of piezoelectric to substrate thickness

We also developed a numerical simulation methodology for piezoelectric harvesting systems that allows for high-fidelity finite element models of the harvester electromechanics as well as realistic nonlinear circuits models; a typical example is shown in Fig. A12. Our approach synthesizes conventional harmonic finite element analysis and a harmonic balance approach that accounts efficiently for the nonlinear circuit behavior, bypassing the need for computationally expensive time marching schemes. The proposed methodology solves, via an iterative residual reduction scheme, for the coupled electrical output and structural dynamics of the piezoelectric harvesting structure, which is analyzed in the frequency domain. The proposed method is well suited for integration into model-predictive design methods. We illustrated the capability of the proposed approach to predict previously unreported coupling phenomena between the nonlinear circuit response and piezoelectric structural behavior. The increased accuracy in the circuit model and flexibility of this method over current models outweighs the increased numerical costs.

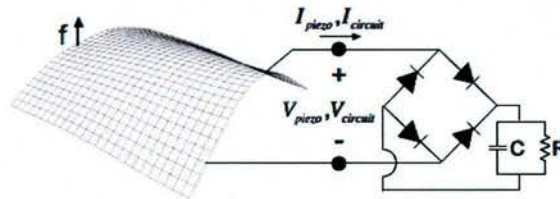


Fig. A12. Schematic of the coupled electromechanical energy harvesting system with a finite element model and full-bridge rectifier with voltage ( $V_{circuit} = V_{piezo}$ ) and current ( $I_{circuit} = I_{piezo}$ ) interface conditions

Finally, we demonstrated the ability to harvest energy from the propagation of phononic (elastic, acoustic) waves in two-dimensional piezoelectric solids by spatially patterning the polarization distribution. We simulated the wave fields by the finite element method and demonstrated the ability to dynamically alter the wave propagation by switching on/off the piezoelectric behavior by operating the electrodes in a closed or open circuit configuration. The piezoelectric



polarization patterns were non-intuitive and were determined by topology optimization. We showed the interesting response of optimally patterned phononic devices with four examples: a filter, a waveguide, an energy harvester, and a wave actuator. Fig. A13 shows a device we designed to harvest energy from elastic waves propagating in a solid via the optimal layout of piezoelectric polarization throughout its volume.

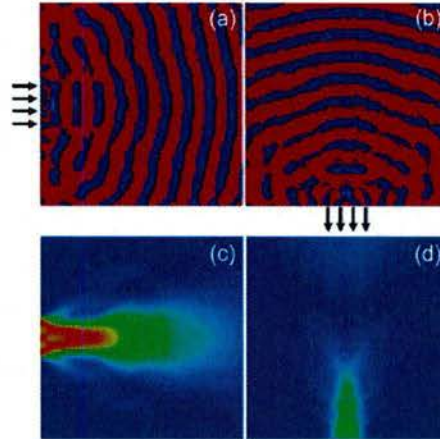


Fig. A13. Piezoelectric polarization pattern for the wave (a) harvester and (b) actuator with corresponding distributions of the (c-d) Poynting vector magnitude

### A5. Design of UAV Test Bed

To evaluate the performance of the EHSS technology developed in this MURI project, we have developed a virtual and a hardware UAV test-bed. This includes a detailed high-fidelity aeroelastic model of a mid-size UAV which has been developed and built at the Research Center for Unmanned Vehicles at the University of Colorado (see A-Figure A14). The numerical model will allow the MURI team to evaluate quickly the improvements of the system-level performance through novel EHS materials and devices and guide the development of the fundamental research. It will further allow us to optimize the integration of one or multiple EHSS devices into the airframe. The UAV hardware will mainly serve as verification platform to test the EHSS in-situ and as technology demonstrator.

In the first year of this MURI project we developed a large aeroelastic model and performed mesh and time-step convergence studies. In collaboration with Dan Inman we are currently using the virtual UAV test bed to quantify the kinetic energy available for mechanical harvesting due to representative wind variations.

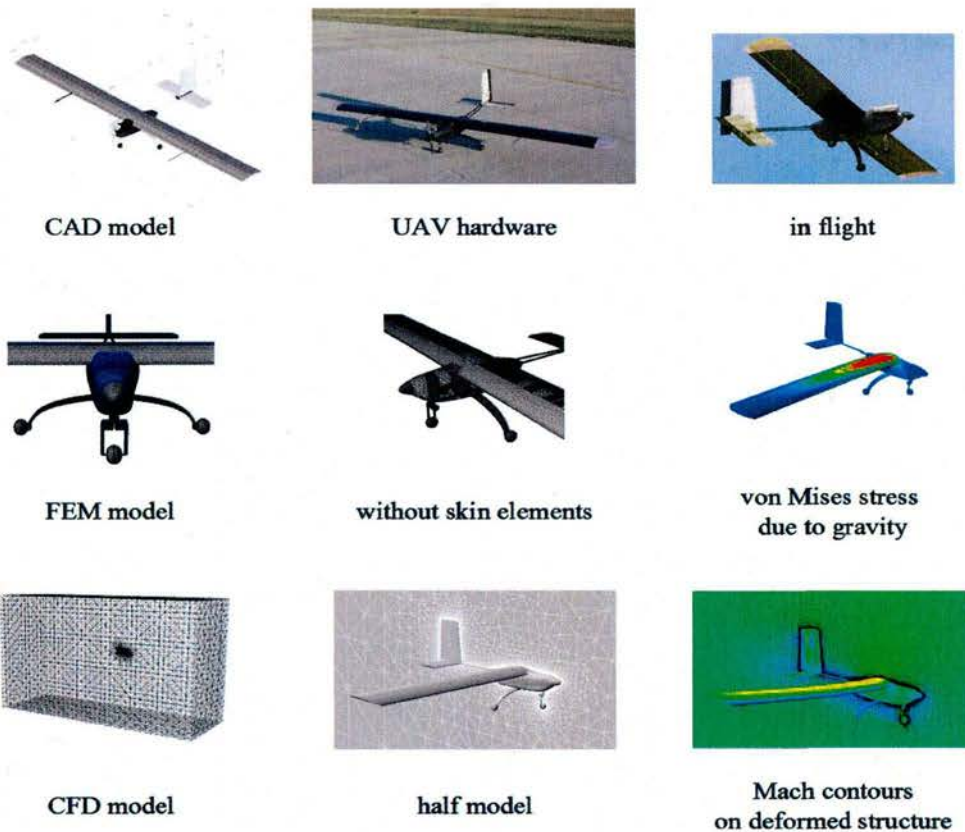


Figure A14. Hardware and virtual UAV test bed. The figures in the upper row show the CAD model of the HAVUC UAV developed by senior aerospace students at the Research Center for Unmanned Vehicles, as well the aircraft on the ground and in flight. The figures in the middle row show the finite element model of the HAVUC aircraft developed in the past year under this MURI grant. The FE model captures accurately the CAD geometry and contains shell and volume elements. The half model has 59,124 nodes leading to 302,253 degrees of freedom. The lower row shows the CFD model and aeroelastic simulation results. In the past year, we have developed a 3-D inviscid model with 373,690 nodes resulting in about  $1.8 \cdot 10^6$  unknowns. The CFD Euler and the FE structure models are coupled using our in-house aeroelastic simulation platform. The figure in the lower right corner shows the Mach contours on the aeroelastically deformed vehicle for a nominal flight speed of  $Ma=0.04$  at sea level.

#### **Task B. Energy Harvesters based on Thermoelectrics (Taya, Yang and Ju)**

Here we report on the progress in the following three subtasks

B1: Design, synthesis, characterization and modeling based on low-cost high specific figure-of-merit TE materials and modules.

B2: Thermoelectric characterization

B3: Thermal switch design



## **B1: Design, synthesis, characterization and modeling based on low-cost high specific figure-of-merit TE materials and modules (Taya).**

### **Introduction**

Thermoelectric phenomena involve the direct conversion between thermal and electrical energy. Due to its solid-state technology, it has unique advantages as an electrical power generator such as high reliability, no vibration and quiet operation. With these advantages, thermoelectric devices have been used in a wide range of applications from waste heat recovery to refrigeration (Goldsmid, 1964). The efficiency of the thermoelectric materials is determined by the dimensionless figure-of-merit ( $ZT$ ), defined as

$$ZT = \frac{S^2 \sigma}{\kappa_{ph} + \kappa_{el}} T \quad (B1)$$

where,  $S$ ,  $\sigma$ ,  $\kappa$ , and  $T$  are the Seebeck coefficient, the electrical conductivity, thermal conductivity which is a sum of lattice ( $\kappa_{ph}$ ) and carrier component ( $\kappa_{el}$ ), and the absolute temperature at which the properties are measured, respectively. For the enhancement of thermoelectric performance, higher values of Seebeck coefficient and electrical conductivity, which give rise to maximized power factor ( $S^2 \sigma$ ), and lower thermal conductivity are required. However, the interdependence of these physical properties makes the improvement of  $ZT$  difficult because an increase of electrical conductivity usually decrease Seebeck coefficient, and increase thermal conductivity by Wiedemann-Franz law.

The majority of research on thermoelectrics are aimed to increase the figure-of-merit ( $ZT$ ) value without considering other factors; weight of TE device, cost-effectiveness, environmental issue, and ease of mass production. The weight of the TE modules can be a critical parameter considering specific energy efficiency particularly airborne applications where specific figure of merit, defined as  $ZT$  divided by mass density, should be emphasized. Recently, thermal energy harvesting based on TE generator modules has been applied to automobiles (Saqr et. al., 2008) and unmanned aerial vehicles (UAV) or micro-aero-vehicle (MAV) (Pogue et. al., 2005), see Fig. B1. In automobile applications, use of TE modules is to improve fuel efficiency by utilizing the wasted heat dissipation which is about 40% in gasoline engine system (Yu et. al., 2009).

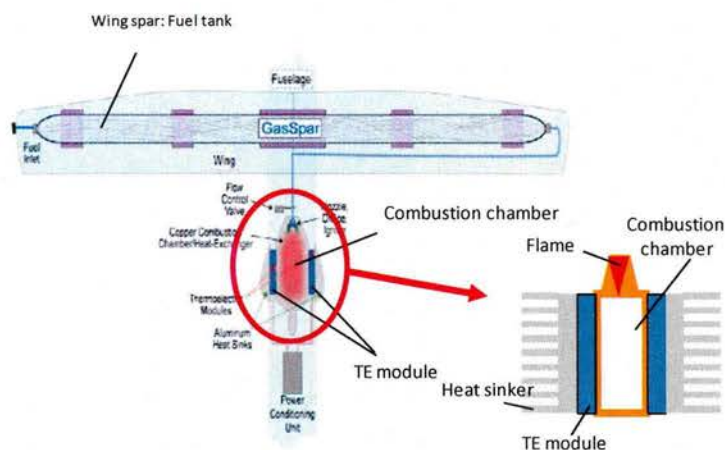


Fig. B1. Conceptual view of combustion engine system and TE generator in UAV (Pogue et. al., 2005)

In this MURI project we focused on

(i) design, synthesis, characterization and validation of TE materials and modules based on low cost and high specific figure-of-merit, and (ii) integration of such TE modules into UAV/MAV combustion chamber.

#### (1) Synthesis of bulk n- and p-type TE alloys based on $Mg_2Si$ compounds

$Mg_2Si$  based TE alloys are light-weight, toxic-free, and cost-effective materials. Popular TE compounds working at intermediate temperature up to  $500^\circ C$  are based on Lead Telluride ( $PbTe$ ) (Crane et. al., 2009),  $AgPb_mSbTe_{2+m}$  (LAST) (D'Angelo et. al., 2011),  $Te/Ag/Ge/Sb$  (TAGS) (Crane et. al., 2009) and  $Co_2Sb_3$  (El-Genk et. al., 2006). Even though these TE materials provide higher ZT values, they have large mass density of more than  $8.0 [g/cm^3]$  which increases the weight of TE modules. In addition, Lead (Pb) is toxic element, and Tellurium compound is classified as poison materials. Regarding the cost effectiveness, The Clarke index of Si and Mg has higher rank of 2<sup>nd</sup> and 8<sup>th</sup>, respectively (Lotka, 1923). Te, one of the key components in TE system, is rare metal element and the common materials such as Ag in LAST is very expensive, resulting in increasing base cost of final module device.

Recently, environmentally-friendly energy harvesting system attracts a great deal of interest. Mg-Si system thermoelectric (TE) materials are one of the promising candidates in an intermediate temperature range (Noda et al, 1992; Aizawa and Song, 2006; Riffel and Schilz, 1998) thanks to its light weight, low-cost, scalable to larger size and non-toxic materials, best suited for future air vehicles. The specific figure of merit (ZT/density) of  $Mg_2Si$  is one of the highest values as shown in Table B1, though its performance is not higher than existing bulk TE materials (Fig. B2). Our goal is synthesis of high specific figure of merit  $Mg_2Si$  and MnSi thermoelectric (TE) materials suitable for airborne energy harvesting through “nanocomposite”.

Most recently, significant advances for increasing ZT have been made based on electron and phonon engineering using nanostructure (Venkatasubramanian, 2001; Halman et al, 2002; Hsu et al, 2004; Sales et al, 1996). The extensive research in thermoelectric properties of superlattices (Venkatasubramanian, 2001; Halman et al, 2002) shows that ZT enhancement comes mainly



from thermal conductivity reduction due to incoherent phonon scattering at the interfaces of periodic superlattice sites while concurrently improving or maintaining electron performance.

TE Material	ZT/density
Mg <sub>2</sub> Si	0.380
SiGe	0.331
MnSi	0.090
Bi <sub>2</sub> Te <sub>3</sub>	0.178
Zn <sub>4</sub> Sb <sub>3</sub>	0.214
Ag <sub>0.89</sub> Pb <sub>19</sub> SbTe <sub>20</sub>	0.210

Table B1. Specific ZT values of selected bulk TE materials.

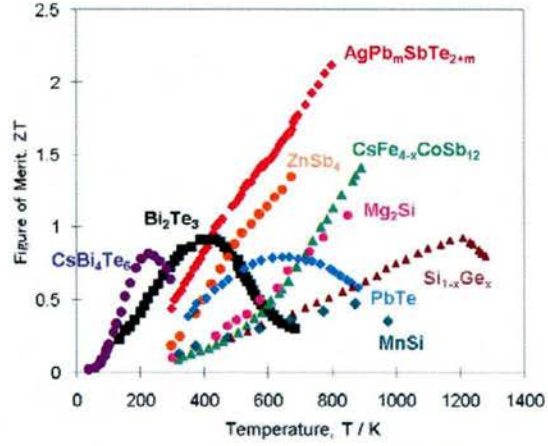


Figure B2. Figure of Merit (ZT) as a function of temperature for some bulk TE materials

### B1-1 Synthesis and characterization of TE materials

#### Processing route

In order to obtain high ZT value, minimizing thermal conductivity is one of the key methods for bulk TE alloy system. This is required to introduce grain size reduction up to nano scale to enhance intensive phonon scattering resulting in the reduction of lattice thermal conductivity. However, conventional processing technology has difficulty in fabricating bulk thermoelectric materials with very fine grains because of grain growth during solidification process. This work enlightened that the high energy mechanical alloy enables large quantities of nanoparticles, and advanced hot-pressing technique can suppress the grain growth compared to traditional sintering method. The idea is nanograins produced by high energy mechanical alloying (planetary ball milling) and rapid sintering technique (spark plasma sintering) can introduce a high density of grain boundary interfaces, which scatter phonons more effectively than charge carrier, and result in reduction of the lattice thermal conductivity. This combination process of mechanical alloying and Spark Plasma Sintering (SPS), see Fig. B3, has an advantage of controlling the exact molar ratio of Mg to Si while the volatilization of Mg via conventional approach such as direct melting method is inevitable since the evaporation temperature of Mg is lower than the melting temperature of Si.

#### Mechanical alloying (MA)

In this study, planetary ball mill, see Fig. B4, was used, which generates strong centrifuge forces to create impacts of high-energy mechanical alloy actions inside the container by introducing the opposite rotating directions of grinding jar and supporting disc. The loading and unloading of raw materials in the milling jar with balls were performed in the glove box system at Ar atmosphere to avoid oxidation of the starting materials, and then the milling jar was set in the planetary ball milling equipment at dry condition followed by wet grinding milling with hexane as the process control agent (PCA). The milling liquid was used because oxygen-free *n*-hexan

( $C_6H_{12}$ ) has the additional advantage to protect the material from oxidation. After finishing alloying process, the milled powders were transferred to the glove box and dried in vacuum environment in antechamber of the glove box, and then finally nanostructured thermoelectric powder was obtained. Fine magnesium particles are flammable elements when it is exposed to air, and it is even more dangerous when high energy mechanical alloying yields nano sized powders. The glove box system is introduced to protect flammable powers from oxidation and other contamination.

### Spark Plasma Sintering (SPS)

Spark Plasma Sintering (SPS) is a pressure sintering method based on high temperature plasma (spark plasma) generated by electrical discharge ON-OFF DC pulse energizing. The key feature of SPS is a high thermal efficiency due to the direct heating of the graphite mold and stacked powder materials by the large spark pulse current. Fig B3 shows the configuration of our SPS system located at UW-CIMS laboratory. The process of SPS in the graphite mold can be described with 5 steps such as spark discharge, a local high temperature state, evaporation, melting, and necking, see Fig. B4. From a spark discharge at the contact point of particles a local high temperature state is generated and then, evaporation and melting on the surface of powders occur, and necking is formed. This noble sintering technique enables nano powders to be consolidated with a high densification and keep still nano sized grains by providing rapid sintering procedure. In the process, mechanically processed nanopowders were set into graphite die, and compressed by single-axis pressurization system in the chamber with vacuum state, and then sintering followed by cooling performed. During the sintering process carbon die set should be inspected frequently because nanopowder can be melt below its melting point at a certain condition or fracture of graphite die can be occurred by heavy pressure at high temperature.

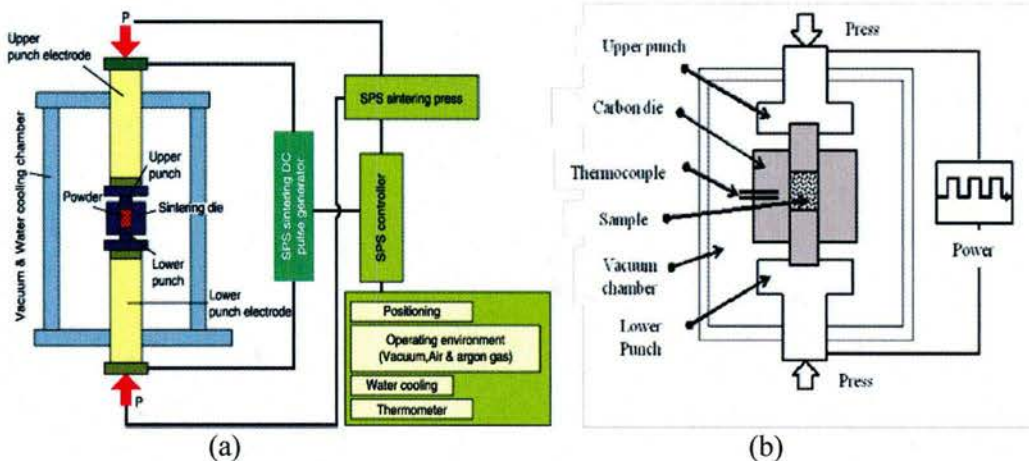


Fig. B3. SPS system configuration: (a) overall SPS system, and (b) a graphite mold (shown in dark color) in the chamber



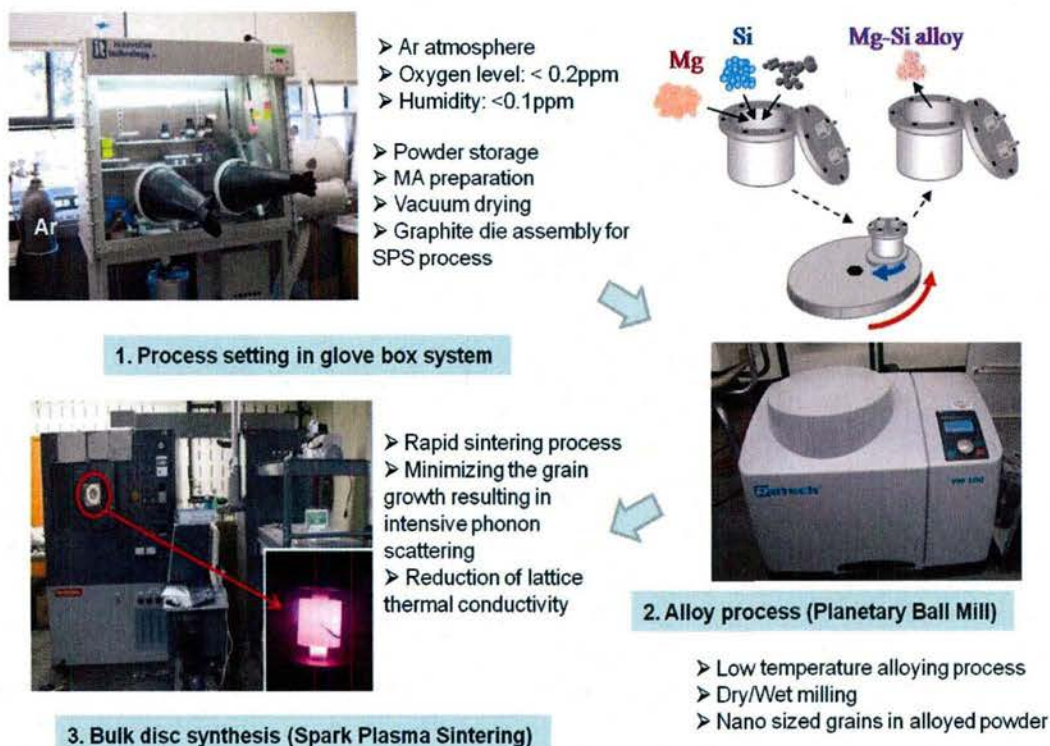


Fig B4. Powder metallurgy route for TE material synthesis

Fig. B4 illustrates the processing steps: (1) the preparation of ball milling process in the glove box (Innovative Technology) by putting raw powers and grinding ball into the jar and sealing, (2) mechanical alloying process (Retsch, PM100) in Ar environment in the milling jar, (3) transferring the alloyed powder in the glove and preparing graphite die assembly for SPS process, and (4) running SPS (Sumitomo Coal Mining Co., Ltd., Dr. Sinter 1020S).

#### Non-doped Mg based TE alloy n-type of $\text{Mg}_2\text{Si}$

Pure  $\text{Mg}_2\text{Si}$  of n-type TE alloy was synthesized via MA followed by SPS process. The initial Mg and Si powders were mixed in alumina milling jar with alumina ball with the ball to powder weight ratio of 40 to 1, and the jar was clamping in the glove box in Ar atmosphere. The milling condition was 100 rpm for 24 hrs. Fig. B5 (a) is XRD pattern of alloyed compound which shows the mixture of Mg and Si together. The Mg-Si compounds were transferred to glove for precise measurement of its weight and control of Mg and Si contents, followed by encapsulation of the Mg-Si powders. The compounds were pressurized by SPS under 50MPa in vacuum chamber and sintered at 700C for 3min holding time with the heating rate of 30C/min. The XRD pattern of solid bulk  $\text{Mg}_2\text{Si}$  shown in Fig. B5 (b) illustrates pure  $\text{Mg}_2\text{Si}$  alloy.

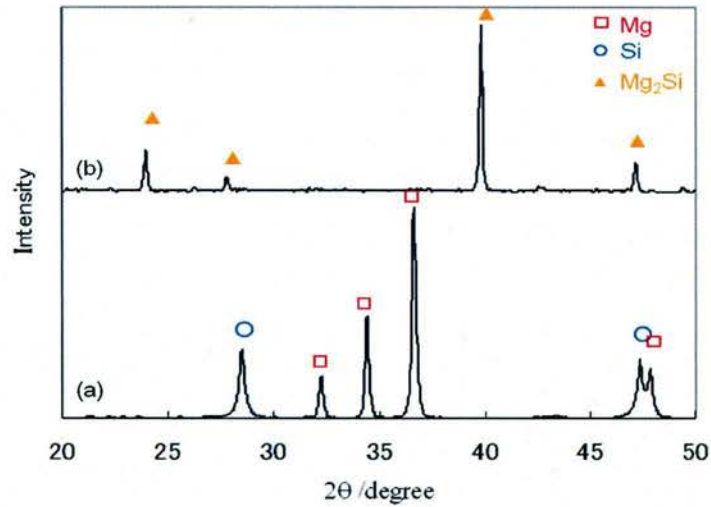


Fig. B5. XRD pattern of n-type  $\text{Mg}_2\text{Si}$ : (a) Ball milled Mg-Si composite powder, and (b) as-SPSed  $\text{Mg}_2\text{Si}$  bulk disk

#### p-type of $\text{Mg}_2\text{Ge}$

As to Mg based p-type alloy,  $\text{Mg}_2\text{Ge}$  behaves p-type TE materials. Similar to synthesizing n-type  $\text{Mg}_2\text{Si}$ , the combination of MA and SPS process was performed. The initial Mg and Ge powders were mixed in alumina milling jar with alumina ball with the ball to powder weight ratio of 40 to 1. The mechanical alloying was run at 100 rpm for 24 hrs. Fig. B6 (a) is XRD peaks of the mixture of Mg and Ge. The graphite die setting was done in the glove box to prevent oxidation and contamination. The SPS was carried out under 50MPa in vacuum and sintered at 500C for 3min holding time with the heating rate of 30C/min. Fig. B6 (b) shows the XRD pattern of solid bulk  $\text{Mg}_2\text{Ge}$ .

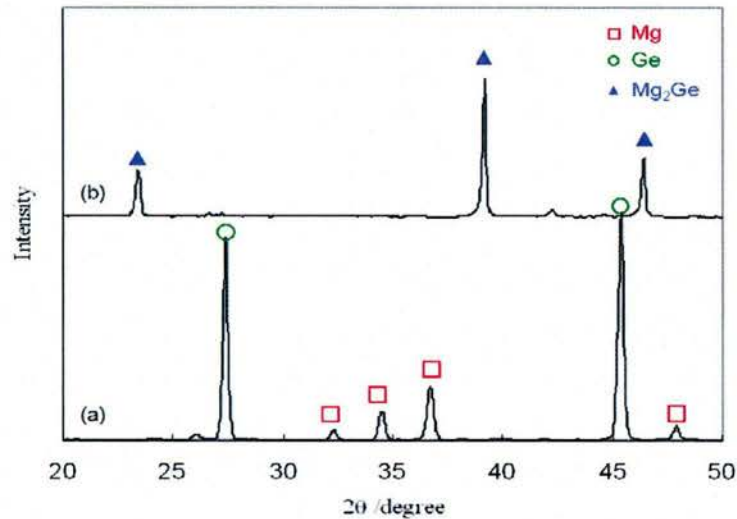


Fig. B6. XRD pattern of p-type  $\text{Mg}_2\text{Ge}$ : (a) Ball milled Mg-Ge composite powder, and (b) as-SPSed  $\text{Mg}_2\text{Ge}$  bulk disk



Both n-type of  $\text{Mg}_2\text{Si}$  and p-type of  $\text{Mg}_2\text{Ge}$  were synthesized successfully via the combination of MA and SPS technique. However, MA process generated only the mixture of initial raw powders, not alloy compounds after milling process, see Fig. B6 (a) which means MA process did not generate nanostructures in the powders as well as grain boundaries to increase intensive phonon scattering to minimize thermal conductivity. Low milling energy of 100 rpm would be the reason of incomplete alloying during MA.

In order to increase the milling energy (speed and time), different types of jar and ball were carried out. Various jar and balls can be selected such as alumina, stainless steel, tungsten carbide, agate and zirconium oxide depending on its purpose and alloying elements. In this study of  $\text{Mg}_2\text{Si}$  alloying, three types of alloying medium have been tried for the suitable selection. Fig.B7 is XRD peak analysis of alloyed powders by using grinding medium of alumina, steel and tungsten carbide. Alumina and steel based milling jar and balls are widely used for crushing to powders and mechanical alloying process, however, iron peak was observed in alloyed powder at 300 rpm for 8 hr, Fig. B7 (a), and  $\text{Al}_2\text{O}_3$  peaks were also detected in synthesized powder at 200 rpm for 24 hr, Fig.B7 (b). This contamination came from the reaction between particles and grinding medium due to the high energy induced by high rotating speed and longer time. Fig. B8 is (a) SEM image and (b) EDAX analysis of iron contamination of Mg-Si-Ge sintered bulk sample at which bright spot indicates metal contents of iron coming from alloy jar and balls.

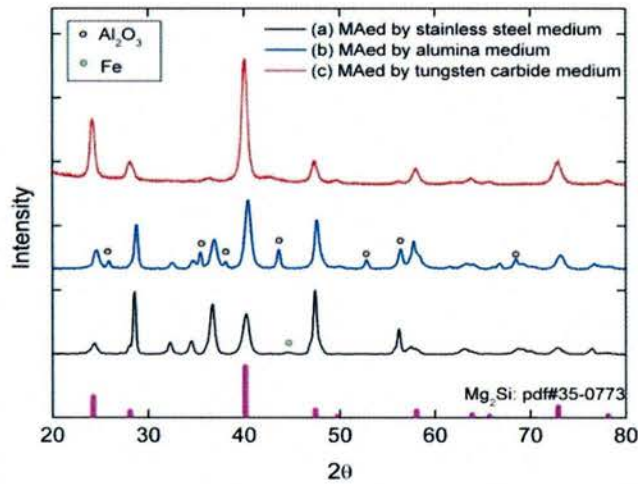


Fig.B7. XRD patterns of three different milling mediums: (a) Stainless steel, (b) alumina, and (c) tungsten carbide

The EDAX result in Fig. B8 (b) shows the amount of iron contamination. For this reason, tungsten carbide jar and balls were selected thereafter for high energy mechanical alloy process. In experiments with tungsten carbide jar and balls, no contamination from grinding medium occurred, which is evidenced from Fig. B7 (c). Therefore, all mechanical alloying processes in this study were performed with tungsten carbide medium under Ar atmosphere.

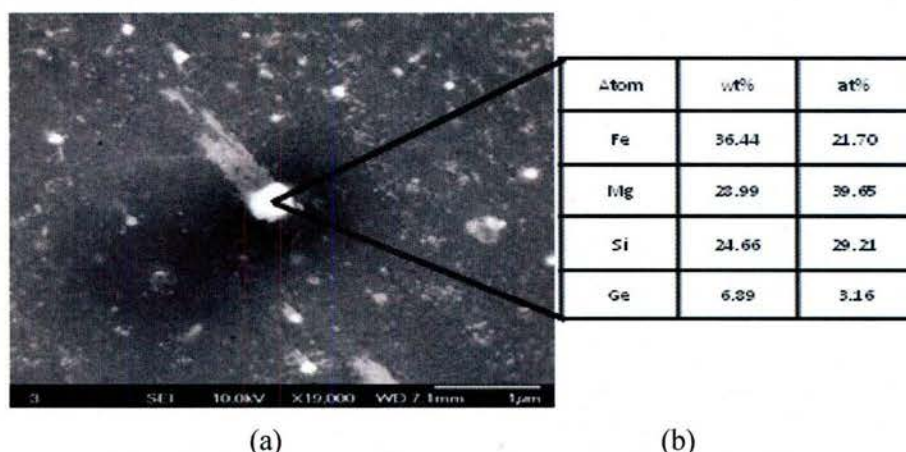


Fig. B8. Fe contamination in MA of stainless steel jar and balls: (a) SEM image of sintered Mg-Si-Ge, (b) EDAX data of the surface

### Doped $\text{Mg}_2\text{Si}$ TE alloy

The typical TE alloys based on solid solution of  $\text{Mg}_2\text{B}^{\text{IV}}$  compounds are  $\text{Mg}_2\text{Si}$  -  $\text{Mg}_2\text{Ge}$ ,  $\text{Mg}_2\text{Ge}$  -  $\text{Mg}_2\text{Sn}$ , and  $\text{Mg}_2\text{Si}$  -  $\text{Mg}_2\text{Sn}$ . Compared to Si element, Ge and Sn have higher mass density, and Ge is very expensive element, so  $\text{Mg}_2\text{Ge}$  and  $\text{Mg}_2\text{Sn}$  compounds are not suitable for airborne TE materials. To meet the requirements of light-weight, non-toxic, and cost-effective TE materials, doped  $\text{Mg}_2\text{Si}$  was selected and studied.

By using tungsten carbide milling medium for higher energy MA process, complete alloyed compounds were synthesized after MA. Fig. B9 is the XRD peaks of alloyed powder with 350 rpm for 5h (Fig. B9a) and 25hr (Fig. B9b) milling, in which complete alloyed  $\text{Mg}_2\text{Si}$  compounds are directly obtained after MA with 25h followed by SPS.

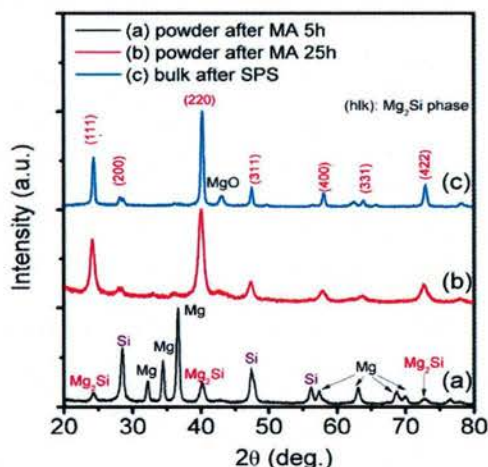


Fig. B9. XRD peaks of alloyed powder and sintered bulk sample

### Bi doped n-type $\text{Mg}_2\text{Si}$

Bismuth (Bi) was selected as doping element because the density of Bi-doped  $\text{Mg}_2\text{Si}$  alloy is lower than that of other solid solutions. To examine the solid solubility of Bi in  $\text{Mg}_2\text{Si}$  alloy for the maximum performance, MA processes with various Bi contents in commercial  $\text{Mg}_2\text{Si}$



powder offered by Union Material Inc. were carried out under 350 rpm – 25 hr of dry MA followed by 250 rpm – 3 hr of wet alloy, and were sintered by SPS method with 80MPa–600C–3 min condition.

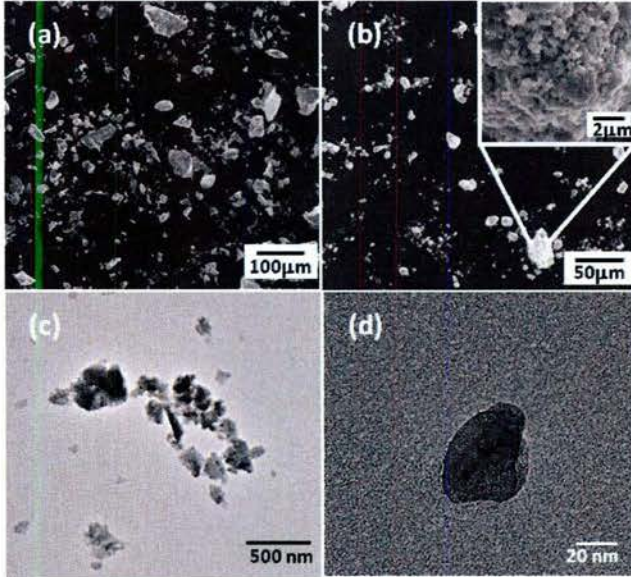


Fig. B10 Microscope images of pulverized powders: (a) SEM image before MA (b) SEM image after MA (400rpm-15hr) (c) TEM image after MA (d) TEM image of nano sized particle

Fig.B10 shows the microscopy images of mechanically alloyed particles of Mg-Si. Particle size was in the range of sub micron to hundred microns (Fig. B10a) before alloying process. Under increasing alloying energy, the size of as-milled particles became finer less than 20 micron at 400rpm for 15hr in MA-2 (Fig. B10b, c). High resolution transmission electron microscopy (HRTEM) image in Fig. B11 (b) shows that the grain boundaries are high angled randomly oriented boundaries. These adjacent grains with random orientation enable more phonon scattering effectively, which gives rise to the reduction of lattice thermal conductivity. Therefore, high energy mechanical alloy process successfully yields nano sized alloyed particles with range of 20nm to 200nm and sub boundary interfaces in the particles with sub nanometers.

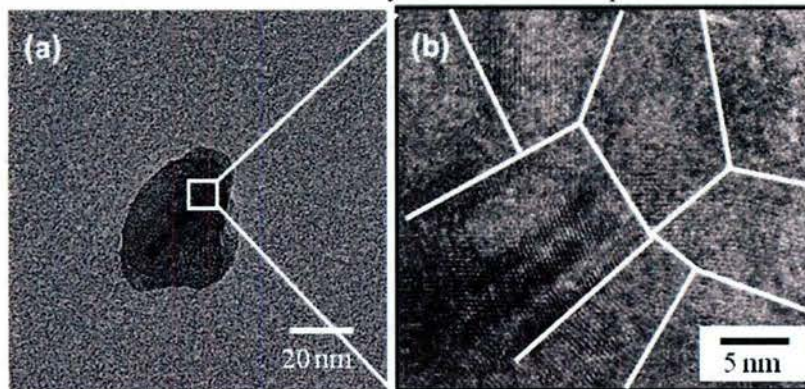


Fig. B11 HRTEM images of *n*-type Bi doped  $\text{Mg}_2\text{Si}$ : (a) nano-particle of diameter of 30 nm (b) which as grain boundaries with different orientation

The electrical conductivity and Seebeck coefficient were measured by commercial equipment (Ulvac, ZEM-3), and thermal conductivity was measured by a laser flash system (Ulvac, TC-

9000) from room temperature to 600°C. The results of the measured thermoelectric properties are shown in Fig. B12. As larger amount of Bi contents (larger  $x$  contents in figures), electrical conductivity was increased (Fig. B12a) while Seebeck coefficient was decreased (Fig. B12b). This is because the carrier mobility was increase by the effect of Bi dopant. Thermal conductivity are little influenced by Bi (Fig. B12c). From the result of the figure-of-merit (Fig. B12d), 3 at % Bi doped  $\text{Mg}_2\text{Si}$  gives the best performance, in which the highest  $ZT$  was obtained of 0.61 at 600°C.

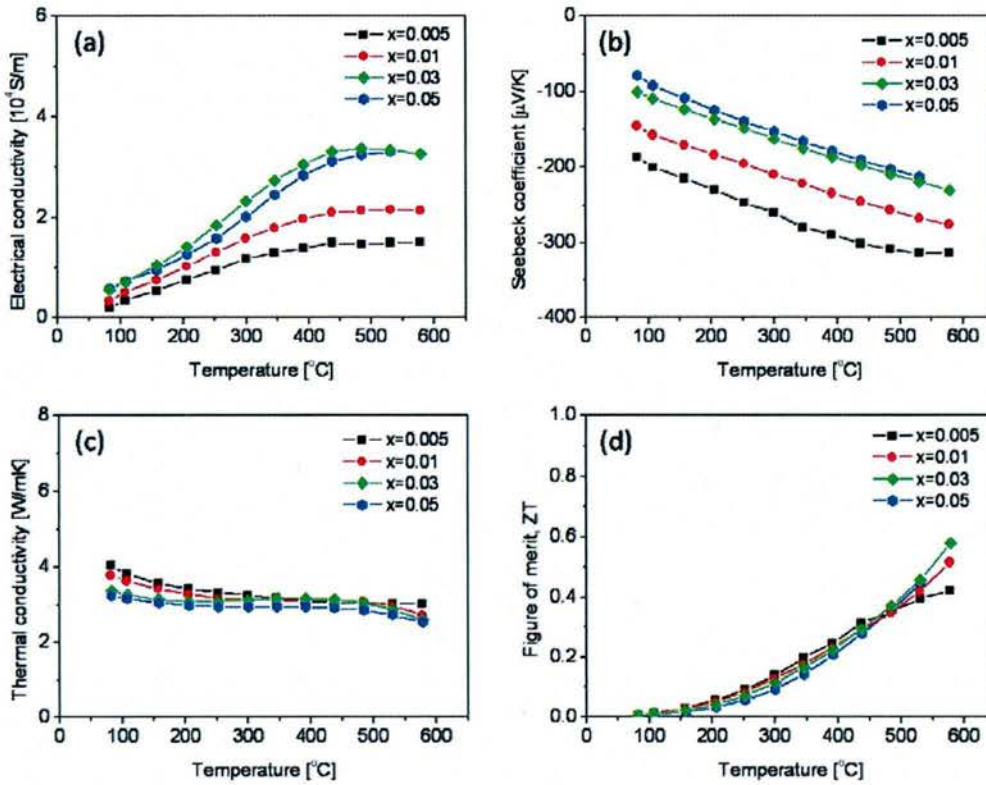


Fig. B12 Thermal properties of  $\text{Mg}_2\text{Si}:\text{Bi}_x$ : (a) Electrical conductivity, (b) Seebeck coefficient, (c) Thermal conductivity and (d) The figure-of-merit

Since Mg is ductile particles, there can be a loss caused by mechanical alloy process. In order to investigate the effect of excessive Mg contents to the thermoelectric properties, mechanical alloy with three different amount of excessive Mg powder, 0 wt%, 2 wt% and 4 wt%, was carried out. In this case, Mg (99.9%), Si (99.9%), and Bi (99.999%) powder were used as the starting materials instead of pre-synthesized commercial  $\text{Mg}_2\text{Si}$  powder. Fig. B13 shows the thermoelectric properties of electrical conductivity (Fig. B13a), Seebeck coefficient (Fig. B13b), thermal conductivity (Fig. B13c) and the figure-of-merit (Fig. B13d), in which 2% surplus Mg gave the highest value of figure-of-merit, 0.44, but the difference is less than 3% each other. This means that MA process can control exact molar ratio by avoiding the loss of Mg contents during alloying process.



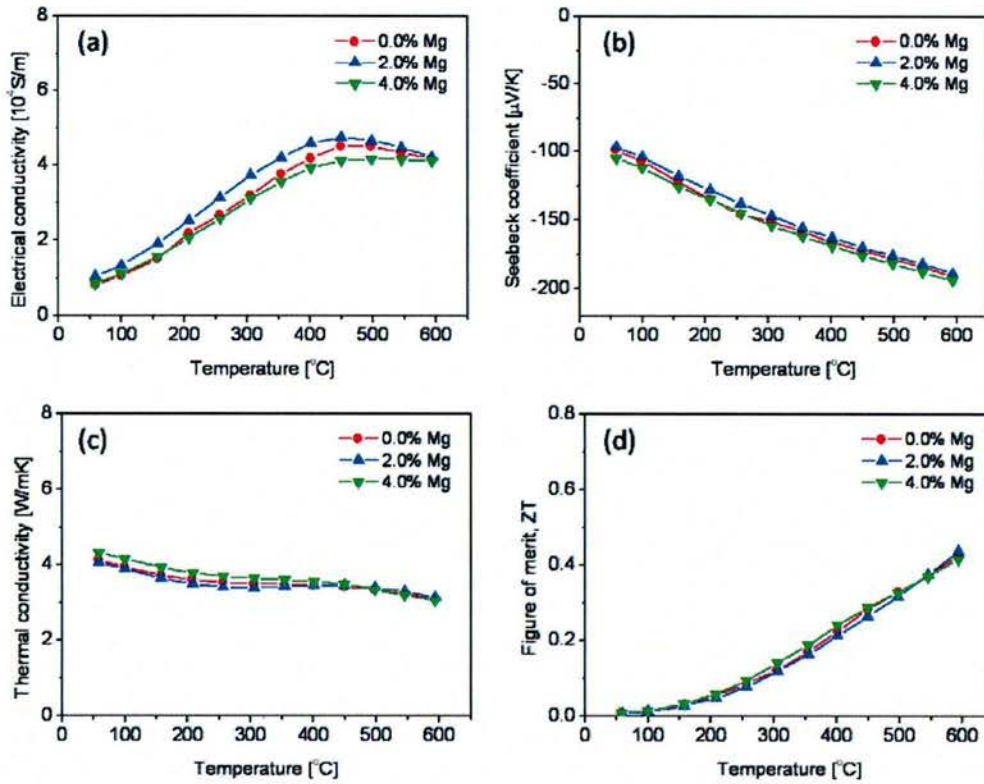


Fig. B13 Thermal properties of  $\text{Mg}_2\text{Si}_{0.97}\text{Bi}_{0.03}$  with excessive Mg powder: (a) Electrical conductivity, (b) Seebeck coefficient, (c) Thermal conductivity and (d) The figure-of-merit

#### Bi-In doped n-type $\text{Mg}_2\text{Si}$

In order to improve electrical properties of Bi doped  $\text{Mg}_2\text{Si}$ , new doping element, Indium, was investigated. In addition, to verify the suppression of grain growth of synthesized alloys via MA and SPS processes, two specimens were prepared. First, Bi doped  $\text{Mg}_2\text{Si}$ , where  $\text{Mg}_2\text{Si}$  powder was offered by Union Material Inc., was prepared as a reference alloys via direct melting process in electric furnace followed by crushing the ingot into powders. Then, the powder is consolidated via SPS process. Second, Bi-In doped  $\text{Mg}_2\text{Si}$  was synthesized via MA followed by SPS.

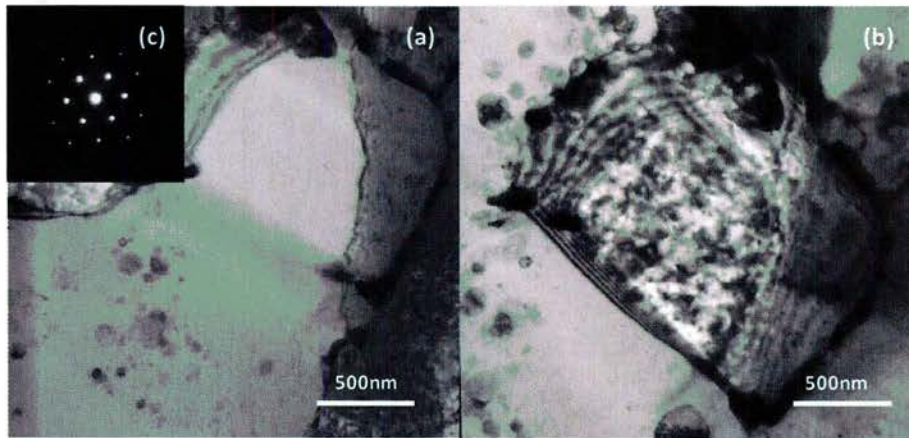


Fig. B14 TEM images: (a) and (b) are two beam bright field images, and (c) diffraction pattern

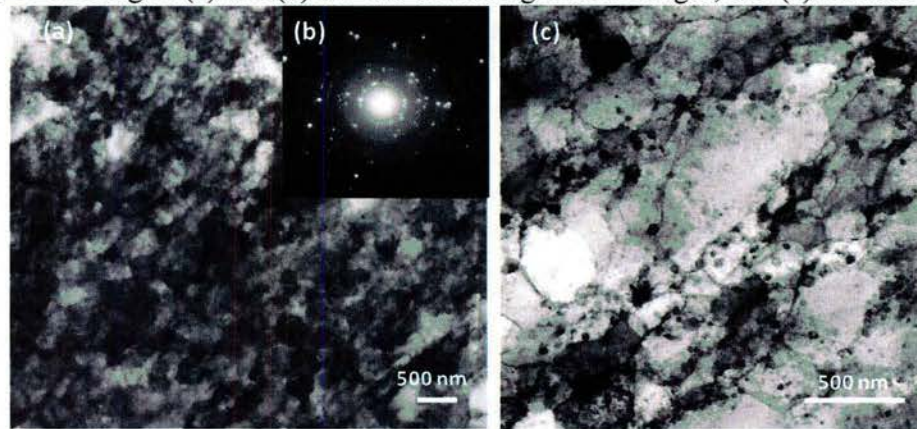


Fig. B15 TEM images: (a) two beam bright field TEM image, (b) diffraction pattern and (c) STEM image

In Fig. B14, two beam bright field TEM images show grains and their boundaries with grain size of more than 2 micron. This large grain is shown in Fig. B14 (a) and diffraction pattern of its grain is in inset figure, Fig. B14 (c). One of the smallest grains which is about 1 micron is shown in Fig. B14 (b). Fig. B15 shows TEM images of Mg-Si-Bi-In alloy and its diffraction pattern. Fig. B15(a) and (b) are TEM and STEM images, respectively, which are showing the size of grains. The size of most grains is smaller than 500nm. The ring pattern of the diffraction pattern in inset figure tells different orientation of grains in the selected area, which means small grains of this sample. Based on TEM observation, it is proved that the combination of MA followed by SPS processing can generate nano size powders and suppress grain growth due to rapid sintering process via SPS. This method for TE material synthesis is good for decreasing thermal conductivity resulting from the reduction of lattice thermal conduction.



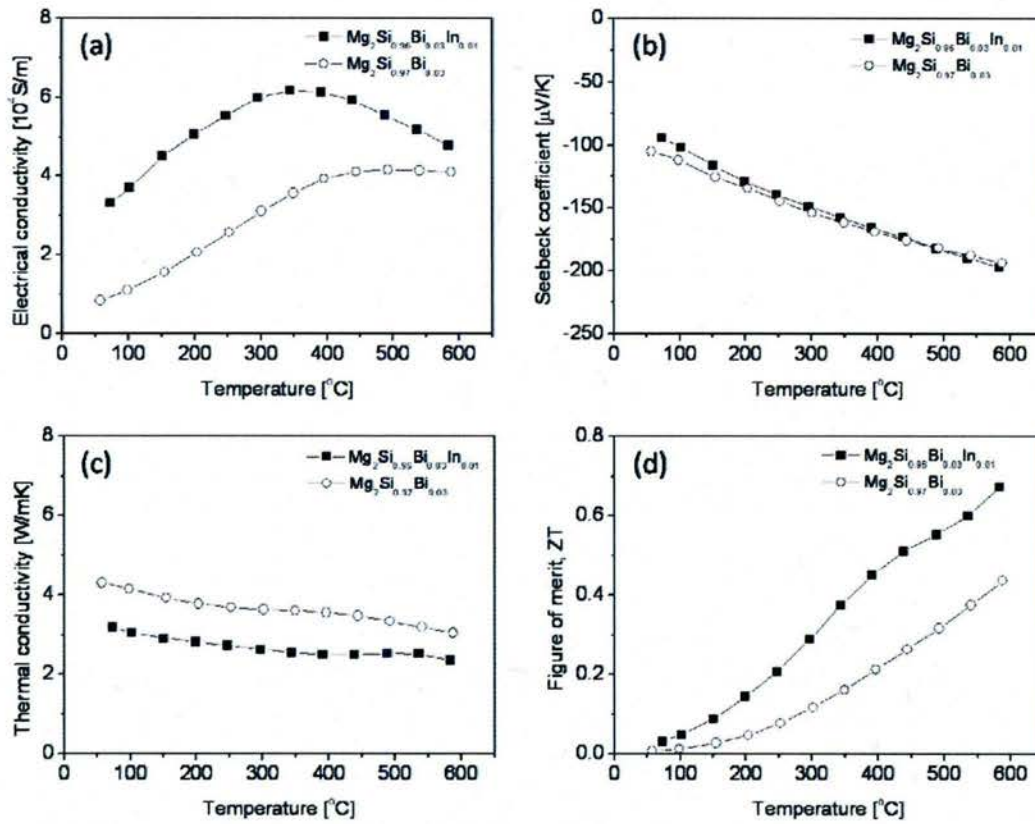


Fig.B16 Thermoelectric properties of  $\text{Mg}_2\text{Si}_{0.97}\text{Bi}_{0.03}$  and  $\text{Mg}_2\text{Si}_{0.96}\text{Bi}_{0.03}\text{In}_{0.01}$ : (a) electrical conductivity (b) Seebeck coefficient (c) thermal conductivity, and (d) the figure-of-merit

Fig. B16 shows electrical and thermal conductivities and Seebeck coefficient of the two alloys. The negative sign indicates *n*-type. While Seebeck coefficient is almost identical each other for the measured temperature range, electrical conductivity (Fig. B16a) of the bulk  $\text{Mg}_2\text{Si}_{0.96}\text{Bi}_{0.03}\text{In}_{0.01}$  is increased by factor of 2 from room temperature to around 350°C compared with  $\text{Mg}_2\text{Si}_{0.97}\text{Bi}_{0.03}$ , and the difference is smaller from 350°C to 600°C. The enhancement of the electrical conductivity is due to the increase of mobility by doping with In. The thermal conductivity of  $\text{Mg}_2\text{Si}_{0.96}\text{Bi}_{0.03}\text{In}_{0.01}$  was decreased compared with  $\text{Mg}_2\text{Si}_{0.97}\text{Bi}_{0.03}$  due to longer alloying time with higher alloying speed, which gives rise to finer grains. Therefore, the figure-of-merit of Bi-In doped  $\text{Mg}_2\text{Si}$  was enhanced up to 0.68, which is 1.5 times larger than that of  $\text{Mg}_2\text{Si}_{0.97}\text{Bi}_{0.03}$  alloy, see Fig. B16 (d).

#### X doped $\text{Mg}_2\text{Si}$ (X=Na, K, Ag)

Various doping elements in  $\text{Mg}_2\text{Si}$  system were studied such as Na, K and Ag. MA was carried out under 350 rpm for 25 hr, and SPS process was performed at 800°C for 3min. Fig. B17 shows TE properties of various doped  $\text{Mg}_2\text{Si}$ . Na is p-type doping element, and K is n-type dopant while Ag doped  $\text{Mg}_2\text{Si}$  has a transition from n-type to p-type at 350°C. ZT of these TE alloys are much lower than that of Bi doped or Bi-In doped  $\text{Mg}_2\text{Si}$ . Thus we have not pursued to use these alloys.

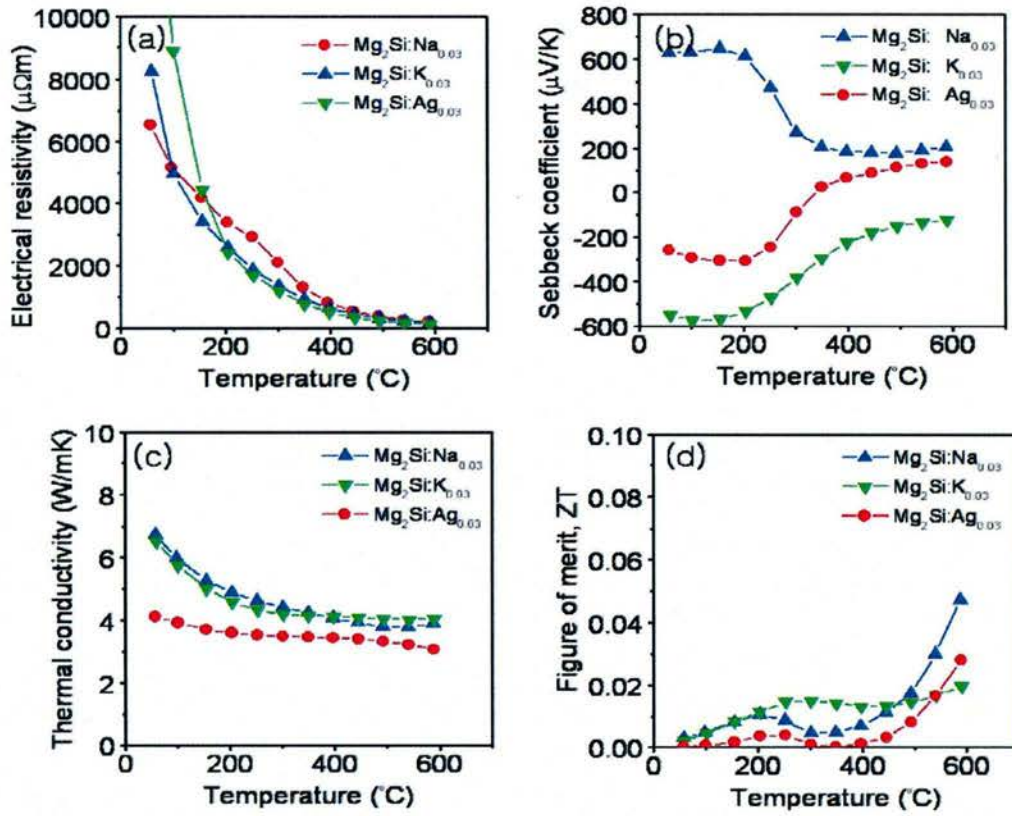


Fig.B17 Thermoelectric properties of X doped  $\text{Mg}_2\text{Si}$  (X=Na, K, Ag) : (a) electrical conductivity (b) Seebeck coefficient (c) thermal conductivity, and (d) the figure-of-merit

### B1-2 TE generator module

#### Preparation of TE materials and characterization

Collaborating with Prof. Iida at Tokyo University of Science for Bi doped  $\text{Mg}_2\text{Si}$  (n-type), and Prof. Itoh at Nagoya University for higher manganese silicide (HMS,  $\text{MnSi}_{2-x}$ ,  $x=0.250-0.273$ ) for p-type materials, segmented TE generator was fabricated where the lower temperature TE leg of commercial Bi-Te based TE compounds (Tellurex Inc.) was used. Fig. B18 (a) through (d) show temperature dependent TE properties of n-type  $\text{Mg}_2\text{Si}$  and p-type HMS for high temperature segments, and n- and p-type Bi-Te for low temperature segments. TE properties of all TE materials used in our TE module are given in Fig. B18 where the high temperature TE materials used are  $\text{Mg}_2\text{Si}$  (n-type) and HMS (p-type), and low temperature TE materials are n-type  $\text{Bi}_2\text{Te}_{3-x}\text{Se}_x$  and p-type  $\text{Bi}_{2-x}\text{Sb}_x\text{Te}_3$ .



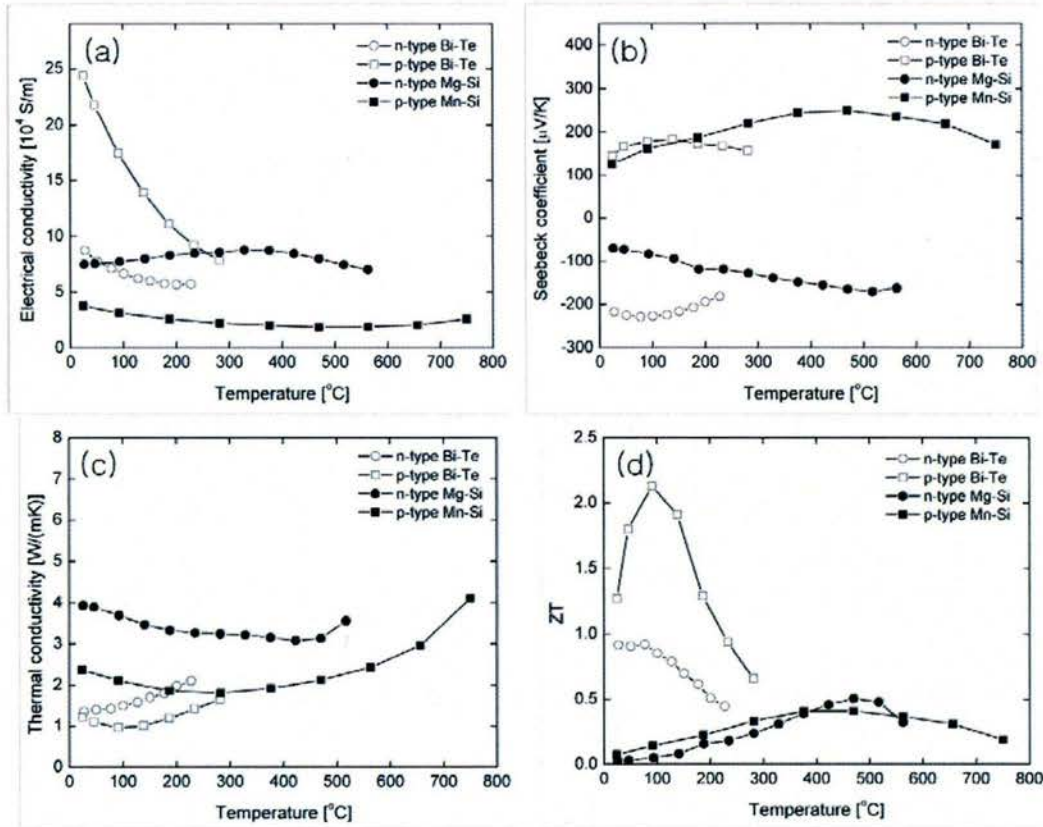


Fig. B18 Temperature dependent TE properties of n-type  $\text{Mg}_2\text{Si}$  and p-type HMS as high temperature segment, and n-type  $\text{Bi}_2\text{Te}_{3-x}\text{Sb}_x$  and p-type  $\text{Bi}_{2-x}\text{Sb}_x\text{Te}_3$  as low temperature segment: (a) electrical conductivity, (b) Seebeck coefficient, (c) thermal conductivity, and (d) Dimensionless the figure of merit, ZT

### Module assembly

For TE module assembly, high temperature TE legs of  $\text{Mg}_2\text{Si}$  and HMS are connected to Cu electrode by brazing technique, and segments of TE materials are soldered each other. Before brazing and soldering process, it is essential that Ti (50nm) and Ag (1 $\mu$ m) layers are coated by E-beam evaporator to increase the interface bonding. Ti is active element, ideal adhesion metallic material between semiconductor blocks and metal coating layer, and Ag has low wetting contact angle which helps the surface stick to bonding alloys. Table B2 shows all solder materials for bonding these interfaces. All bonding process is carried out under the gas flowing (2 l/min) environment of Ar balance + 5% hydrogen to prevent joint interfaces from oxidizing and contaminating during high temperature process. This process with Ti and Ag adhesive layers ensures lower contact resistance and strong bonding. After the assembly of  $\pi$  shape TE module, aluminum nitride (AlN) substrate is attached to the top and bottom sides of pre-assembled TE generator by using ceramic bond. Since AlN is thermally conductive and electrically insulating material, it transfers heat flux from heat source to TE segments, while preventing from short circuit between adjacent n-p pair as well as a heat source.

Alloys	Soldering materials	Bonding layer (A-B)	Processing condition
Alloy 1	Ag-Cu-Sn-Zn	Cu - ( $n_1, p_1$ )	680°C-5min
Alloy 2	Ag-Cd	$n_1-n_2, p_1-p_2$ ( $n_1, p_1$ ) - Cu	425°C-3min
Alloy 3	Sn-Ag	$n_1-n_2, p_1-p_2$ ( $n_1, p_1$ ) - Cu	250°C-3min
Alloy 4	Pb-Ag-Sn-In	$n_1-n_2, p_1-p_2$ ( $n_1, p_1$ ) - Cu	350°C -5min

Table B2 The list of all solder materials for bonding interfaces: alloy 4 is the best solder among alloy 2 ~4 for low temperature junctions

### Contact resistance

Electrical contact resistance plays an important role in a segmented TE module generator. High contact resistance between TE segments as well as at junctions of metal electrodes would decrease the generator's performance by reducing output power generation. Thus, the minimization of contact resistance at all interfaces is highly desired. The contact resistance measurement is carried out based on the four-point probe set up where two current probes are connected to both ends of a sample to generate current flow through the sample. One voltage probe is located at the end of the Cu electrode while the other voltage probe is scanning along the sample length to detect voltage drop depending on distance between two voltage probes, so the electric contact resistance is obtained from ohm's law based on measured current and detected voltage drops across the bonding interfaces between the fixed and the scanning probe. Fig. B19 shows the measured resistance associated with the cross section area of TE segments depending on the distance of two voltage probes. The measured contact resistance at the interface of Cu electrode bonded with n- and p-type TE segments are 4.8 [ $\mu\Omega \text{ cm}^2$ ] and 3.2 [ $\mu\Omega \text{ cm}^2$ ] at high temperature side, and those at low temperature side are 43.2 [ $\mu\Omega \text{ cm}^2$ ] and 73.6 [ $\mu\Omega \text{ cm}^2$ ], respectively. The contact resistance across the interface of high temperature and low temperature TE segments are 75.2 [ $\mu\Omega \text{ cm}^2$ ] for n-type and 94.4 [ $\mu\Omega \text{ cm}^2$ ] for p-type. The measured average electrical contact resistance across the junctions is 49 [ $\mu\Omega \text{ cm}^2$ ], and the measured electrical resistance of 2-pair segmented module is 25 [ $\text{m}\Omega \text{ cm}^2$ ].

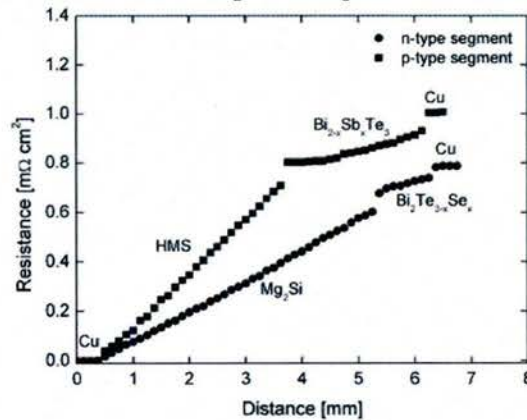


Fig. B19 Electrical resistance as a function of distance through segmented legs of p- and n-type TE column



### B1-3 Power measurement

The assembled TE module generator is tested for its output power performance under temperature difference ( $\Delta T$ ) of up to 500°C. A heat source located at the top of the TE module generator is made of two cartridge heaters insulated by magnesium oxide, which are inserted in metal block. It gives rise to hot side temperature ( $T_H$ ) on top of TE generator module after steady-state temperature is reached, and heat sink is Cu solid block with water flow channel inside for tab water circulation to maintain the bottom side of the TE device at constant cold temperature ( $T_C$ ). Under the heater, Fe plate is inserted to simulate combustion chamber wall, into which TE generator is integrated to utilize temperature gap between chamber temperature and outside air. Then, TE module device is stacked between Fe plate and Cu block on the heat sink. The stacks are surrounded with 2-inch thick insulation wall made of compressed fiberboard to ensure 1-D heat flow vertically, and thermocouples are inserted at each stacked interface as well as Cu electrode to monitor temperatures through heat flow direction.

The measurement tests are carried out under various temperature differences ( $\Delta T$ ),  $\Delta T = 100^\circ\text{C} \sim 500^\circ\text{C}$ . For  $\Delta T = 500^\circ\text{C}$ , the hot side temperature of top AlN substrate of the module is set to  $520^\circ\text{C}$  while the cold side temperature of bottom AlN substrate is kept below  $23^\circ\text{C}$  during the whole measurement process. The measurement at each step of temperature difference is recorded after waiting for the steady-state heat flow reached typically, in 22 hours for  $\Delta T = 500^\circ\text{C}$ . The maximum output power is generated at a half of open circuit voltage under the impedance matching. Fig. B20 (a) shows the output power generation of the module for various  $\Delta T$ 's. At  $\Delta T$  of  $498^\circ\text{C}$ , the maximum output power measured is 0.48 [W] at the load current of 3.4 [A] under load resistance of 41 [ $\text{m}\Omega$ ]. Since the net area of TE materials in 2-pair module device is  $0.64 [\text{cm}^2]$ , the power density of the TE modules (output power per unit area) becomes  $0.75 [\text{W}/\text{cm}^2]$ . Fig. 20 (b) shows the power generation and its power density as a function of temperature difference, which grow parabolically with increasing temperature gap.

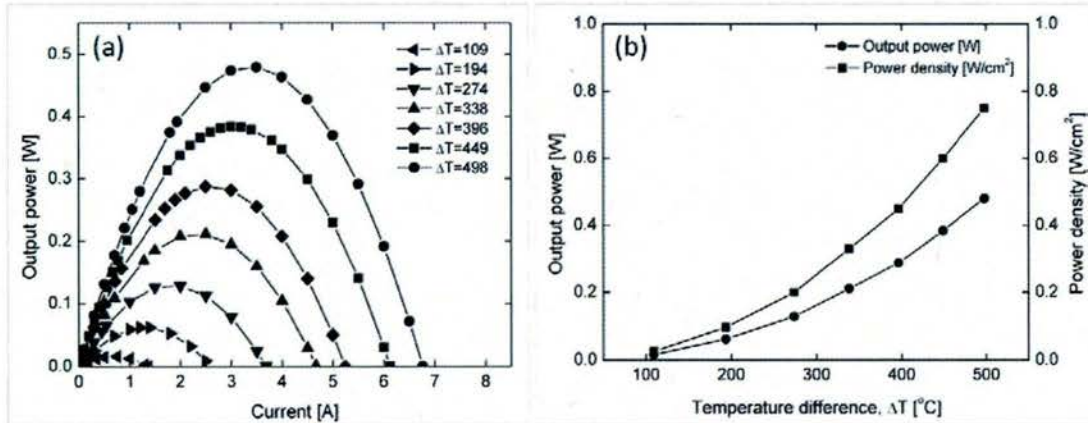


Fig. B20 The experimental results of 2-pair segmented TE module test: (a) Output power generation as a function of load current with various  $\Delta T$ , and (b) The maximum output power generation and power density as a function of  $\Delta T$

#### B1-4 Modeling of segmented TE generator

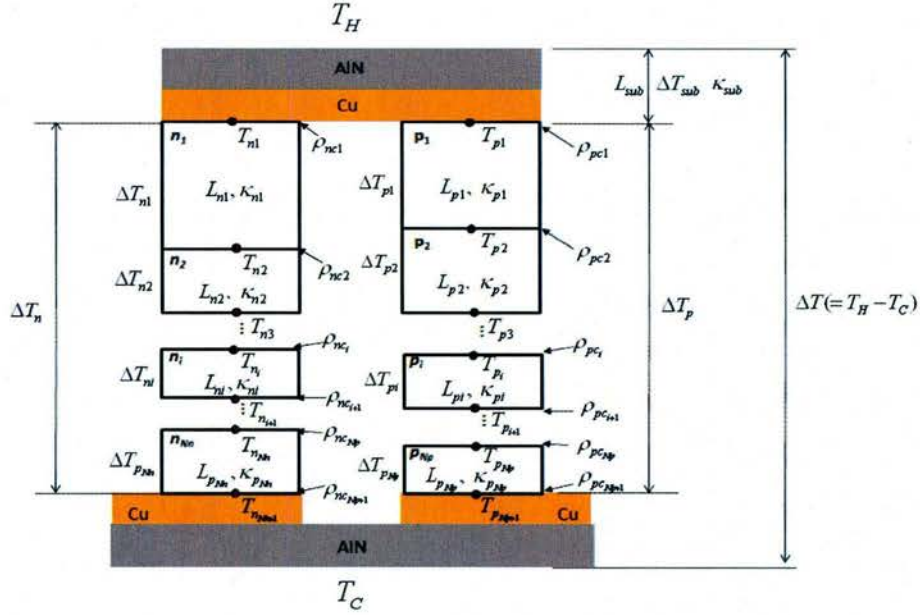


Fig. B21 General segmented TE module with the number of  $N_n$  for n-type leg and  $N_p$  for p-type column

The generalized model of segmented TE module is shown in Fig. B21, and it is made of combined TE legs consisting of the number of n- and p-type segments,  $N_n$  and  $N_p$ , respectively. In addition, typical TE generator is made of connecting  $N$  pairs electrically in series and thermally in parallel.

Open circuit voltage of  $N$  pairs is,

$$V_{OC} = N(S_p^M - S_n^M)(T_H - T_C) \quad (B2)$$

where,  $S_p^M$  and  $S_n^M$  are the effective Seebeck coefficient of  $N_p$  and  $N_n$  number of TE elements, respectively.

$$S_p^M = \frac{\sum_{i=1}^{N_p} S_{p_i} \frac{\kappa_p^E L_{p_i}}{\kappa_{p_i} L_p}}{\sum_{i=1}^{N_p} \frac{\kappa_p^E L_{p_i}}{\kappa_{p_i} L_p} + 2 \frac{\kappa_p^E L_{sub}}{\kappa_{sub} L_p}}, \quad S_n^M = \frac{\sum_{i=1}^{N_n} S_{n_i} \frac{\kappa_n^E L_{n_i}}{\kappa_{n_i} L_n}}{\sum_{i=1}^{N_n} \frac{\kappa_n^E L_{n_i}}{\kappa_{n_i} L_n} + 2 \frac{\kappa_n^E L_{sub}}{\kappa_{sub} L_n}}$$

Current  $I$  obtained by ohm's law is,

$$I = \frac{N(S_p^M - S_n^M)(T_H - T_C)}{(1+m) \left[ N \left( \frac{1}{A_p} \left( \sum_{i=1}^{N_p} \rho_{p_i} L_{p_i} + \sum_{i=1}^{N_p+1} \rho_{pc_i} \right) + \frac{1}{A_n} \left( \sum_{i=1}^{N_n} \rho_{n_i} L_{n_i} + \sum_{i=1}^{N_n+1} \rho_{nc_i} \right) \right) + R_w \right]} \quad (B3)$$

where,  $m$  is the ratio of load resistance to module resistance,  $R_L/R$ .  $A_p$  and  $A_n$  are cross sectional



area of p- and n-type TE element, respectively.  $\rho_{p_i}$ ,  $\rho_{n_i}$ ,  $\rho_{pc_i}$  and  $\rho_{nc_i}$  are electrical resistivity of  $i^{th}$  p- and n-type element and contact resistance between  $i^{th}$  and  $(i+1)^{th}$  of p- and n-type elements, respectively.  $R_w$  is electric resistance of lead wires measured experimentally. Generally, the effect of  $R_w$  diminishes when  $N$  becomes larger since internal resistance is relatively much larger than that of wires, but it cannot be ignored when  $N$  is small. The load voltage can be obtained from Eq. (B2) and (B3),

$$V = - \left[ N \left( \frac{1}{A_p} \left( \sum_{i=1}^{N_p} \rho_{p_i} L_{p_i} + \sum_{i=1}^{N_p+1} \rho_{pc_i} \right) + \frac{1}{A_n} \left( \sum_{i=1}^{N_n} \rho_{n_i} L_{n_i} + \sum_{i=1}^{N_n+1} \rho_{nc_i} \right) \right) + R_w \right] I + V_{OC} \quad (B4)$$

Thus, output power is obtained as,

$$P = I^2 R_L = \frac{N(S_p^M - S_n^M)^2 (T_H - T_C)^2}{\left[ \frac{1}{A_p} \left( \sum_{i=1}^{N_p} \rho_{p_i} L_{p_i} + \sum_{i=1}^{N_p+1} \rho_{pc_i} \right) + \frac{1}{A_n} \left( \sum_{i=1}^{N_n} \rho_{n_i} L_{n_i} + \sum_{i=1}^{N_n+1} \rho_{nc_i} \right) + \frac{R_w}{N} \right]} \cdot \frac{m}{(1+m)^2} \quad (B5)$$

In this study, it is noted that 2 pairs TE module is assembled, i.e.,  $N=2$  and two segments are used at each type, i.e.,  $N_p=N_n=2$ , and  $A_p=A_n=A$ . The maximum output power can be obtained under  $R_L=R$ , i.e.,  $m=1$ . Therefore, output power generation is expressed as,

$$P = \frac{(S_p^M - S_n^M)^2 (T_H - T_C)^2}{A \left( \sum_{i=1}^{N_p} \rho_{p_i} L_{p_i} + \sum_{i=1}^{N_p+1} \rho_{pc_i} + \sum_{i=1}^{N_n} \rho_{n_i} L_{n_i} + \sum_{i=1}^{N_n+1} \rho_{nc_i} \right) + R_w} \quad (B6)$$

The efficiency of the module is estimated as,

$$\eta = \frac{T_H - T_C}{T_H} \left\{ \frac{4}{Z^M T_H} + \frac{2(S_{p_i} T_{p_i} - S_{n_i} T_{n_i})}{(S_p^M - S_n^M) T_H} - \frac{(R_{p_i} + R_{n_i})(T_H - T_C)}{2R_{tot}^M T_H} \right\}^{-1} \quad (B7)$$

#### B1-4 Comparison of experimental data with predictions by model

The measurement results of 2-pair module are compared to the predicted results for the validation. Fig. B22 (a) shows the measured and predicted  $I$ - $V$  curves under  $\Delta T=498^\circ\text{C}$ , in which the solid line is the predicted results by Eq. (B4) while the plotted markers are the measured data points. The measured open circuit voltage [ $V_{OC}$ ] is 285 [mV] and the predicted value is 295 [mV], which is in good agreement within about 3% error. The measured short circuit current [ $I_{SC}$ ] of about 6.7 [A] is close to the predicted value of 6.65 [A] within 1% error. This good agreement is mainly due to the low contact resistance at bonding interfaces. The measured internal resistance of 2 pair module at room temperature is 23.1 [ $\text{m}\Omega$ ], and calculated value is 22.3 [ $\text{m}\Omega$ ]. This explains that reasonably low contact resistance at the bonding interfaces are achieved, and the measured current is in a good agreement with theoretical value by minimizing the current drop. The maximum power output in Fig. B22 (a) is 0.48 [W] measured at the load current of 3.4 [A], and the predicted maximum output power is 0.49 [W]. This measured value and the theoretical calculation for output power generation are in good agreement within error of 2%. As indicated in Fig. B22 (b), the generated power and power density are a parabolic function of  $\Delta T$  ( $=T_H-T_C$ )

in an agreement with the predicted power equation, Eq. (B6). The maximum efficiency of the module as a function of  $\Delta T$  is illustrated in Fig. B22 (c) where the solid line is the prediction by model and the square markers are the measured points. The maximum module efficiency is 4.6% measured at  $\Delta T=498^\circ\text{C}$ , and the predicted efficiency by Eq. (B7) is 4.9%. A comparison between the measured data and predictions by the model demonstrates that the segmented TE module fabrication and its measurement process are carried out correctly while validating the model.

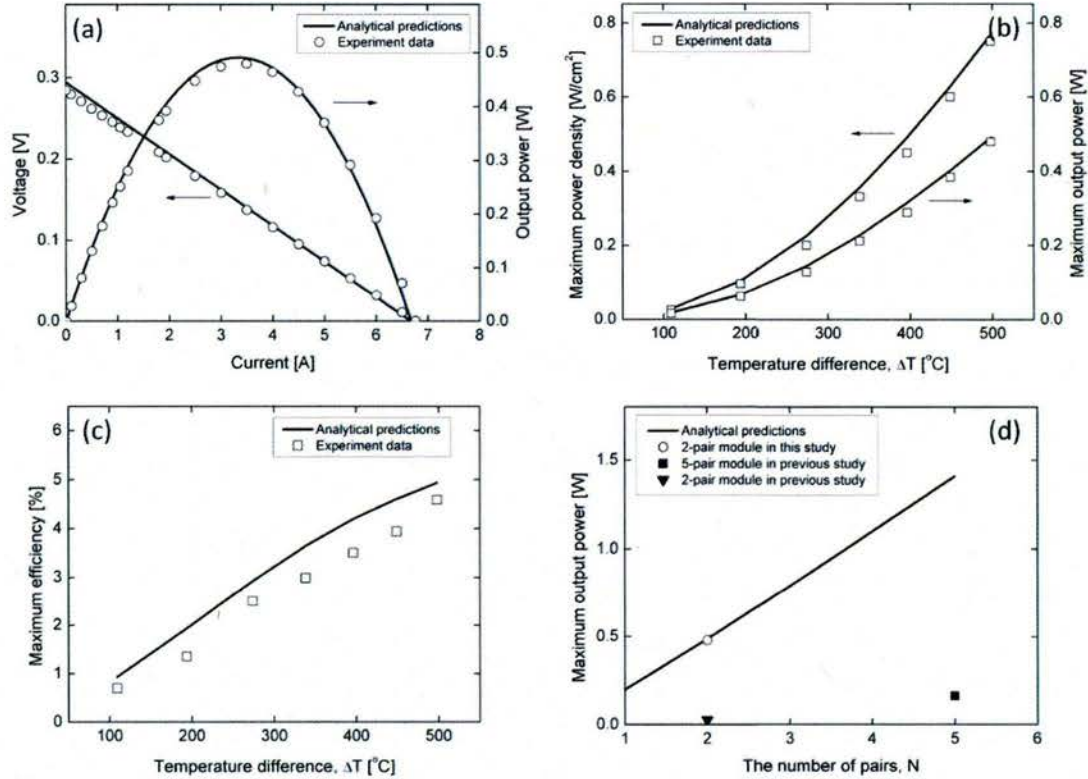


Fig. B22 Comparison of experimental data with prediction by the model: (a) I-V curve and output power as a function of load current, (b) the maximum output power and power density as a function of  $\Delta T$ , (c) the maximum efficiency of the module as a function of  $\Delta T$ . Solid lines are analytical modeling and marks are experimentally measured data, and the maximum output power generation as a function of  $N$ . (Kim et. al. 2012)

### B1-5 Study of TE module design

In this project,  $\pi$  shaped planar TE design was built and performance test was carried out.  $\pi$  shape TE module is a conventional design concept and widely used for TE applications. However, it is unstable if TE legs are not exact parallel each other, and weak to shear stress at the interfaces between TE segment and metal electrode due to large thermal expansion mismatch. Moreover, planar design requires a large number of metal electrodes and big pieces of ceramic plate such as AlN as a thermal conductor and electrical insulator. These parts will increase the total weight of TE module device. Therefore, use of “linear TE module” is better suited for airborne TE generators.

Table B3 shows four possible linear TE module designs. The last row of this Table B3 is the module based figure of merit by accounting for cost, density and energy conversion efficiency



which can be termed as “specific energy conversion per cost (SECC) (defined as efficiency/(cost\*density)”. It follows from Table B3 that linear TE module design (d) gives rise to the highest power density while design (c) provides the highest SECC.





Design type Properties	(a) Linear single 	(b) Linear segmented 	(c) Linear segmented 	(d) Linear segmented 
Materials	n: Bi-Te p: Bi-Te	n: Mg-Si / Bi-Te p: Si-Ge / Bi-Te	n: Mg-Si / Bi-Te p: Mn-Si / Bi-Te	n: Mg-Si / Bi-Te p: Zn-Sb / Bi-Te
Temperature condition	Th=300C Tc=100C	Th=500C Tin=300C Tc=100C	Th=500C Tin=300C Tc=100C	Th=500C Tin=300C Tc=100C
Power [W]	0.21	0.51	0.38	0.57
Power density [W/cm <sup>2</sup> ]	0.66	1.60	1.18	1.78
Specific Power [W/g]	0.28	1.39	0.85	1.14
Efficiency [%]	3.2	4.2	3.3	5.3
Material cost [dollar/g]	0.091	0.195	0.046	0.056
Specific power [W/g/dollar]	3.08	7.12	18.48	10.18

Table B3 Comparison of various TE module designs and their performance in terms of power density, energy conversion efficiency, TE module figure of merit, specific efficiency, material cost of TE module, and the specific energy conversion per cost (SECC)

## B2-2 Thermoelectric Characterization(Yang)

We have built setups for temperature-dependent thermoelectric characterization of nanocomposites. The sample setup, shown in Fig. B23(a), is housed in a high temperature furnace, which can be used for a temperature range between -70C ~1100C. The electrical conductivity and Seebeck coefficient is measured using the four-wire/probe measurement and the thermal conductivity is measured using the Angstrom method.

To study the details of interface effect on phonon and electron transport, we started building a two-color optical pump-and-probe system from Summer 2006, shown in Fig. B23(b). The technique could also probe the ultra-fast non-equilibrium hot electrons, electron phonon interaction and phonon transport to gain fundamental understanding of the electronic and thermal properties at the material interface. Better understanding of the electron and phonon dynamics at the interface will in turn help in synthesizing better thermoelectric nanocomposites. Figure B23(c) shows some preliminary signals we obtained from the system.

A new auto-assembly process has been proposed at CU beyond the original pick and place process for fabricating miniature thermoelectric devices which we termed as “universal fabrication process”. Such a unique process enables fabrication of miniature thermoelectric devices using ultrasonic auto-assembly for mass production. We have designed the masks and started the fabrication process.

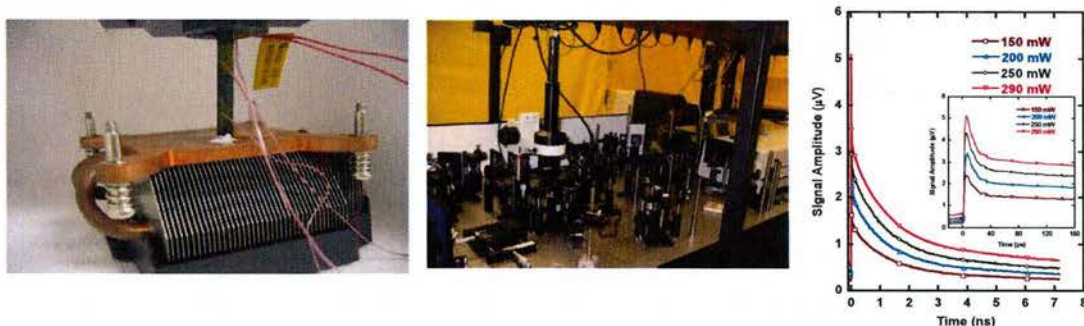


Figure B23. a) sample setup for temperature-dependent thermoelectric characterization of thermoelectric nanocomposites, b) two color optical pump-probe system for studying electron and phonon dynamics at interfaces, c) preliminary signals using the optical pump-probe system.

### B3 Design of thermal switches (Ju)

Thermal conductance switches based on three physical mechanisms were developed. The first switch based on the EWOD (electrowetting on dielectric) phenomenon relies on electric-field induced changes in the shape of liquid droplets to make or break thermal contacts between two planar substrates (Fig. B24a). Thermocapillary flows were found to significantly enhance heat transfer even for dielectric liquids with low thermal conductivities. The second thermal conductance switch is based on reversible morphological transformation of microscale liquid bridges between a thin continuous liquid film (on state) or discrete droplets to form or break thermal contacts (Fig. B24b). It can achieve on-state thermal conductance comparable to that of direct solid-solid contacts at loading pressures several orders of magnitudes smaller while avoiding various reliability challenges (cold welding, fracture/debris, wear). The third switch utilizes the preferential alignments and chain formation of magnetic particles dispersed in an inert liquid under magnetic fields. This design eliminates the need for mechanically moving mechanical supports/substrates but does not provide as high on-state thermal conductance as the second switch design.

We explored an alternative integration strategy where we exploit the unique mechanical characteristics of microscale liquid elements to enable more versatile multifunctional integration of brittle components into mechanical structures. Our basic idea is to mechanically decouple load bearing structures from energy harvesting/storage or other functional devices by using liquid-based mechanical elements (Fig. B25a). Liquid elements offer many intriguing mechanical characteristics. They may break (rupture) but they can be “perfectly” healed. They can withstand significant cyclic deformations without suffering from fatigue and also be designed to change shapes and slip, merge, or split on solid surfaces in response to external stimulations. We developed a rigorous modeling approach based on the surface energy minimization and the virtual work model to predict the shapes and mechanical characteristics of microscale liquid elements (Fig. B25b) and experimentally validate it. We experimentally demonstrated the feasibility of such flexible mechanical interfaces. A silicon chip (thickness of 500 μm) was mounted on a substrate that was subjected to tension and bending. The liquid bridges deformed to accommodate the various mechanical loading while effectively protecting the brittle silicon chip (Fig. B25c).



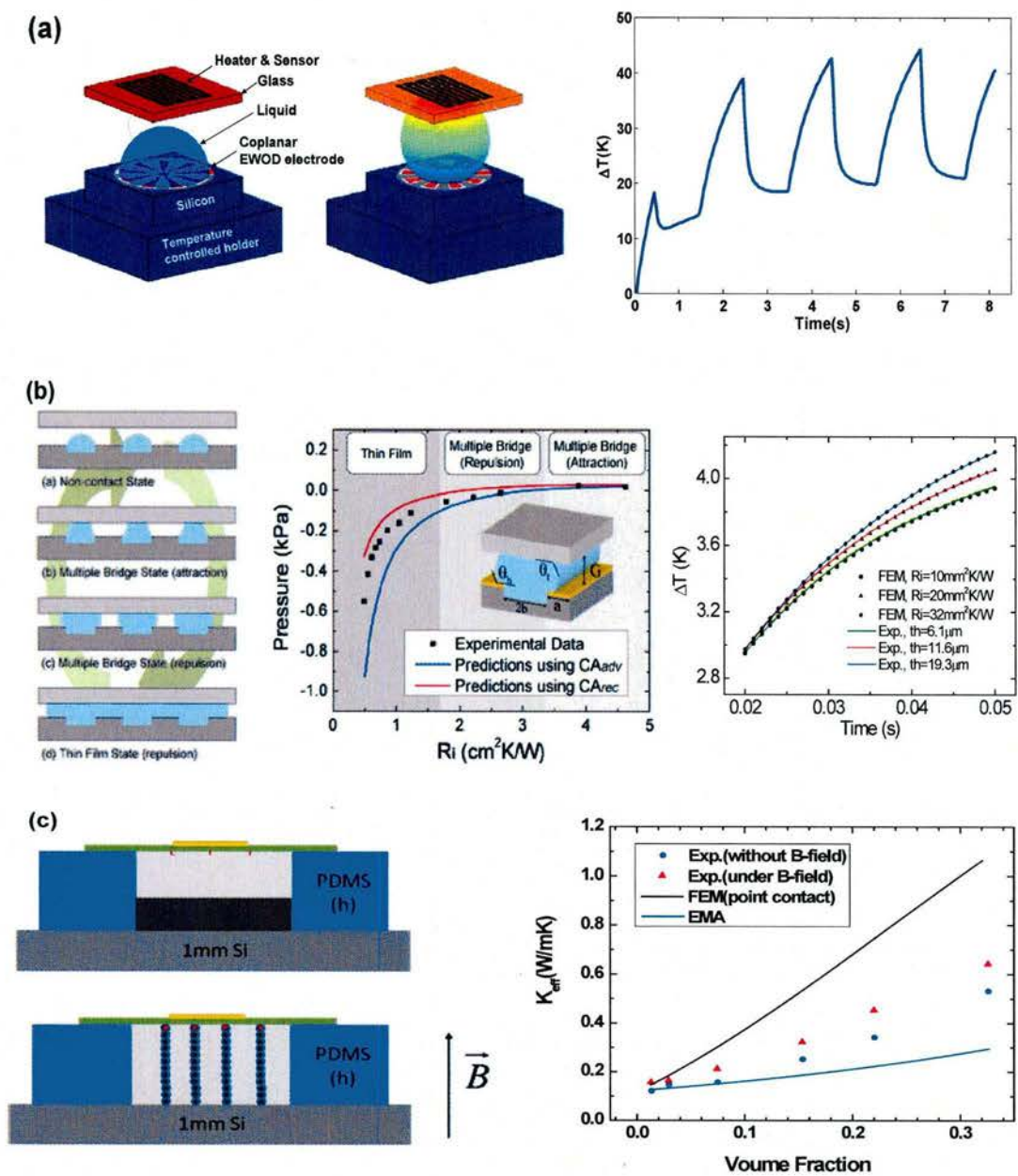


Fig. B24: Thermal switches based on (a) EWOD (b) surface-tension driven reversible morphological transformation (c) magnetorheological instability.

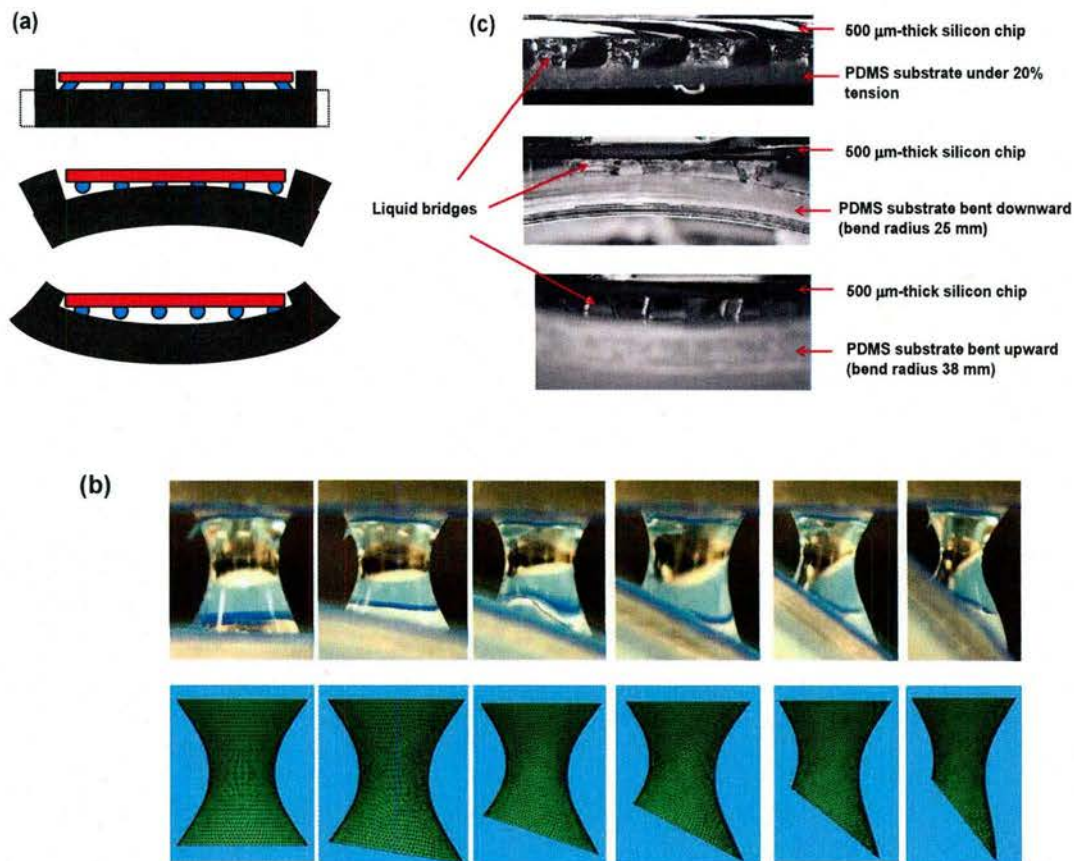


Fig. B25: A conceptual illustration of the mechanical deformation of a functional component (red) integrated onto a load bearing structure (black) using liquid bridges. Liquid bridges (blue) deform or rupture in response to various mechanical loadings. (b) Comparison between the experimentally obtained and predicted shapes of a liquid bridge mounted on a substrate under bending. (c) Optical images of the integrated structures illustrating intact silicon chips mounted on PDMS substrates under three loading conditions.

### Task C: Energy Harvesters based on organic solar cells

Here we report on three subtasks

**C1: Solid state semi-conductor polymer based solar cells (Jenekhe)**

**C2: Dye-sensitized solar cells (DSSC) based on ZnO (Cao)**

**C3: Design of airborne DSSC (Taya)**

**C1: Solid state semi-conductor polymer based solar cells (Jenekhe)**

#### C1a. Objective

The objective of this task of the EHSS MURI effort was to develop high-efficiency polymer or hybrid organic-inorganic solar cells for integration into aero vehicles. Towards this goal we performed the following studies: (i) designed, synthesized, and characterized new donor-acceptor (D-A) conjugated copolymer semiconductors that combine broad absorption spectra with high



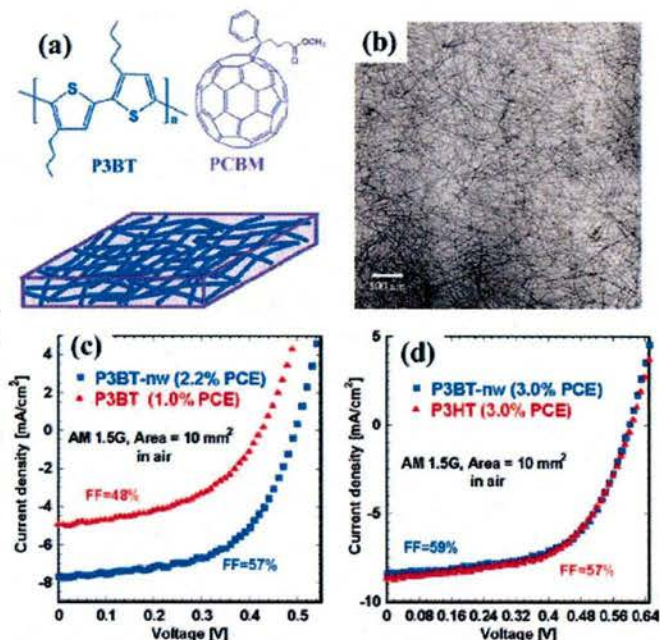
charge carrier mobilities; (ii) fabricated and evaluated bulk heterojunction (BHJ) photovoltaic cells, and (iii) attempted to integrate the organic photovoltaic (OPV) cells with other EHSS components. Our accomplishments during the period we participated in the EHSS MURI are summarized below.

## C1b. Accomplishments

### 1. Highly Efficient Solar Cells Based on Poly(3-butylthiophene) Nanowires.

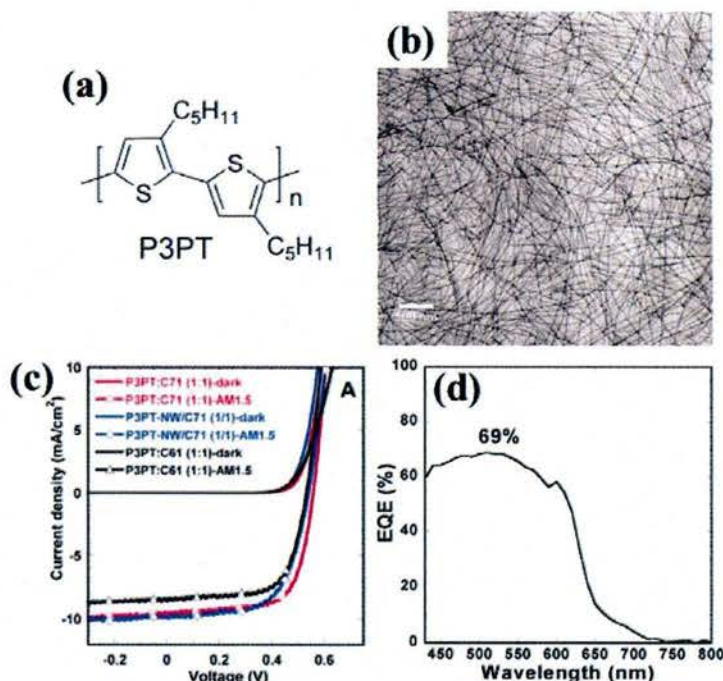
We studied the self-assembly, charge transport, and photovoltaic properties of poly(3-butylthiophene) (P3BT) nanowires, using TEM and AFM imaging, field-effect charge transport, and photovoltaic measurements (Figure C1). We have shown that the fullerene/P3BT-nanowire nanocomposites exhibit an electrically bicontinuous morphology in P3BT nanowire/PC<sub>71</sub>BM bulk heterojunction (BHJ) solar cells. Our results demonstrate the achievement of highly efficient solar cells from P3BT nanowires and that the photovoltaic properties of poly(3-butylthiophene) can be comparable to the much studied P3HT. For example, power conversion efficiencies of 3.3% PCE could be achieved in un-optimized solar cells. This discovery expands the scope of promising materials and architectures for efficient bulk heterojunction solar cells.

We have also studied the *in-situ* self-assembly of P3BT nanowires (NWs) as the donor component in BHJ solar cells. The P3BT NWs, self-assembled in the presence of the fullerene acceptor, formed an interconnected network in the blend films. TEM and AFM imaging revealed P3BT NWs with 11-15 nm width and several micrometer length. High hole mobilities on the order of  $1 \times 10^{-3} \text{ cm}^2/\text{Vs}$  were observed in the P3BT nanowires/PC<sub>61</sub>BM nanocomposites by both SCLC and field-effect transistors. The photovoltaic properties, especially the short-circuit current density, fill factor, and power conversion efficiency were found to depend strongly on blend composition. A power conversion efficiency of 2.52% was achieved from the *in situ* 1:0.5 P3BT: PC<sub>61</sub>BM blend in ambient air. The new *in situ* self-assembly approach provides a means for the rational control of the film morphology in bulk heterojunction polymer solar cells. The performance of the P3BT nanowire/PC<sub>61</sub>BM solar cells is mainly limited by the monomolecular recombination and the high series resistance, which should be addressed in future studies.



**Figure C1.** (a) Molecular structure of poly(3-butylthiophene) (P3BT) and schematic illustration of nanowire network of P3BT/PCBM composites. (b) TEM image of P3BT nanowires. (c) J-V curves of P3BT-nw:PCBM and P3BT:PCBM BHJ solar cells. (d) J-V curves of P3BT-nw:PCBM and P3HT:PCBM solar cells.

## 2. Regioregular Poly(3-pentylthiophene): Synthesis, Self-Assembly of Nanowires, and Efficient Photovoltaic Cells.



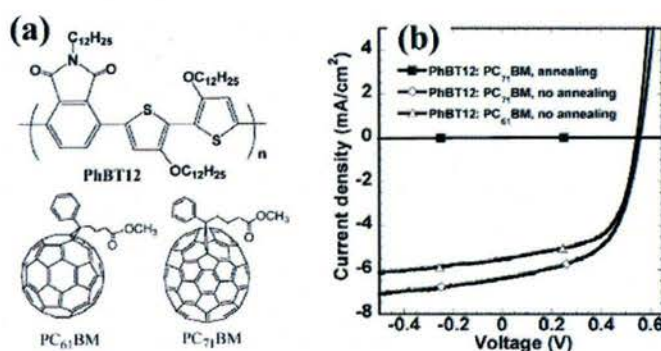
**Figure C2.** (a) Molecular structure of poly(3-pentylthiophene) (P3PT). (b) TEM image of P3PT nanowires. (c) J-V curves of P3PT NW:PC<sub>71</sub>BM BHJ solar cells. (d) IPCE spectra of P3PT NW:PC<sub>71</sub>BM BHJ solar cell.

We have synthesized high molecular weight ( $M_w = 61800\text{--}77\,000$  g/mol, PDI=1.4–1.5) regioregular poly(3-pentylthiophene) (P3PT) and investigated its electronic and optoelectronic properties as well as its self-assembly in solution (Figure C2). P3PT combines good solubility in organic solvents with facile solution-phase self-assembly into crystalline nanowires. P3PT films were found to be highly crystalline, exhibiting a lamellar structure and molecular packing that are characterized by 15.1 Å interlayer  $d_{100}$  spacing and 3.74 Å  $d_{010}$   $\pi$ -stacking distance. The P3PT nanowires (NWs) assembled from dichlorobenzene solution had a width of 16–17 nm and aspect ratios of 70–465, depending on the solution concentration. P3PT had an optical band gap of 1.9 eV and thin film absorption spectrum that are almost identical to those of the well-known P3HT. To demonstrate the potential of P3PT as a p-type semiconductor in organic electronics, we have fabricated and evaluated bottom-contact thin film field-effect transistors and found average and maximum mobility of holes to be 0.04 and 0.10 cm<sup>2</sup>/(Vs), respectively, for the highest molecular weight sample. Bulk heterojunction solar cells based on either P3PT/PC<sub>71</sub>BM blend thin films or P3PT nanowire/PC<sub>71</sub>BM thin films were found to have a maximum 3.33–3.70% power conversion efficiency under 100 mW/cm<sup>2</sup> AM1.5 sunlight illumination in ambient air. The similarity of the electronic, optical, and photovoltaic properties of P3PT to those of P3HT when combined with the higher melting temperature and shorter interchain distances of P3PT make regioregular poly(3-pentylthiophene) a promising p-type semiconductor for organic electronics.



### 3. Efficient solar cells based on a new phthalimide-based donor-acceptor copolymer semiconductor.

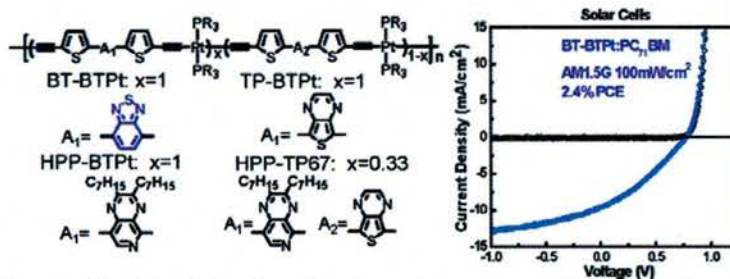
Bulk heterojunction solar cells based on a new small band gap donor-acceptor copolymer, poly(*N*-(dodecyl)-3,6-bis(4-dodecyloxythiophen-2-yl)phthalimide) (PhBT12), have been investigated (Figure C3). PhBT12/fullerene blend films without high temperature (thermal) annealing were shown to exhibit ordered nanoscale morphology by AFM and X-ray diffraction experiments. A space-charge-limited current hole mobility as high as  $4.0 \times 10^{-4} \text{ cm}^2/\text{Vs}$  was measured in the PhBT12/fullerene blend films. A power conversion efficiency of 2.0% was achieved from the 1:1 PhBT12:PC<sub>71</sub>BM blend bulk heterojunction solar cells with a current density of 6.43 mA/cm<sup>2</sup>, an open circuit voltage of 0.56 V, and a fill factor of 0.55. In contrast, thermally (120 °C) annealed PhBT12/fullerene blend films were found to have negligible photovoltaic properties due to severe phase separation which is likely to be caused by the long side chains and resultant PCBM diffusion. The performance of phthalimide-based donor-acceptor copolymers likely has large room for further improvement by modification of polymer side chain and device processing methods to control film morphology as well as the absorption efficiency. These results demonstrate that phthalimide-based donor-acceptor copolymers, exemplified by PhBT12, are promising low band gap candidates for developing efficient bulk heterojunction solar cells.



**Figure C3.** (a) Molecular structures of poly(*N*-(dodecyl)-3,6-bis(4-dodecyloxythiophen-2-yl)phthalimide) (PhBT12), PC<sub>61</sub>BM, and PC<sub>71</sub>BM. (b) The current density-voltage characteristics of PhBT12/PC<sub>71</sub>BM (1:1) and PhBT12/PC<sub>61</sub>BM (1:1) blend solar cells with and without annealing.

### 4. Organometallic Donor-Acceptor Polymer Semiconductors for Solar Cells.

Eleven Pt-bridged organometallic donor-acceptor conjugated polymers, incorporating various electron acceptors have been synthesized by a Sonogashira-type coupling polymerization and characterized (Figure C4). Most of the polymers had weight-average molecular weights ( $M_w$ ) exceeding 10000, while some had  $M_w$  as large as 21000–58000, with polydispersity index around 2. By varying the electron-accepting strength in the donor-acceptor architecture, we demonstrate molecular engineering of the optical absorption bands, electronic band structure (HOMO/LUMO levels),



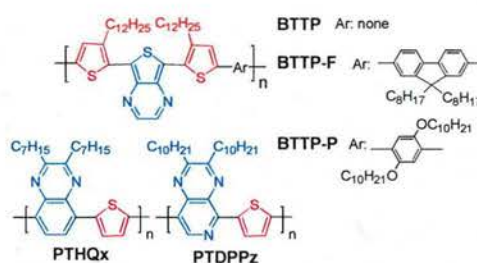
**Figure C4.** (a) Molecular structures of organometallic D-A polymer semiconductors. (b) J-V curves of BT-BTPt:PC<sub>71</sub>BM BHJ solar cells.



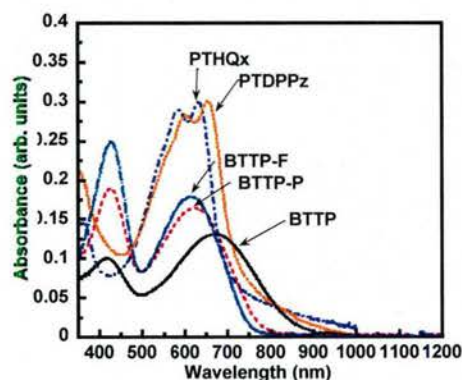
charge transport, and photovoltaic properties. Although the absorption spectra of thienopyrazine-containing copolymers (MTP-BTPt, TP-BTPt, and PTP-BTPt) were broader than BT-BTPt due to the stronger effect of ICT, the improved light harvesting did not translate into improved photovoltaic properties. The observed ionization potentials of  $5.823$  eV facilitated the injection and transport of holes in the polymers, which showed field-effect hole mobilities of  $3.87 \times 10^{-7}$  to  $3.32 \times 10^{-5} \text{ cm}^2/(\text{V s})$ . Electron transport was not observed and this is likely a result of the small electron affinities (2.95–3.28 eV). The highest photovoltaic power conversion efficiencies were observed in blends of the polymers with PC<sub>71</sub>BM, ranging from 0.68–0.71% for HPP-BTPt and BT-T50 to 2.41% in BT-BTPt. Our observed 2.41% PCE for bulk heterojunction solar cells based on BT-BTPt as the donor is significantly lower than the previously reported 4.4–5.0% PCE but is much closer to the theoretically estimated 2.2% PCE for this polymer.

## 5. Donor-Acceptor Copolymer Semiconductors for Solar Cells.

Several D-A copolymers based on thieno[3,4-*b*]pyrazine as the acceptor were synthesized by Stille and Suzuki copolymerizations (Zhu et al, 2006). In addition, thiophene-quinoxaline and thiophene-pyridopyrazine D-A copolymers were also synthesized by Stille copolymerization (Zhu et al, 2008; Kulkarni et al, 2008). The molecular structures of these D-A copolymer semiconductors are shown in Figure C5. As expected, strong intramolecular charge transfer between the electron donor and acceptor moieties in the copolymer chains resulted in broad absorption in the visible-near-IR region (Figure C6). Some of these copolymers, e.g. BTTP, BTTP-F, and BTTP-P, had broad optical absorption bands that extend into the near infrared region with absorption maxima at 667–810 nm, and optical band gaps of 1.1–1.6 eV (Zhu et al, 2006). The other copolymers with quinoxaline and pyridopyrazine acceptor moieties (PTHQx and PTDPPz) also have broad optical absorption with absorption maxima at 630–657 nm, and optical band gaps of 1.75–1.83 eV (Kulkarni et al, 2008). The cyclic voltammograms of the copolymers showed reversible redox peaks, implying that the materials may be capable of ambipolar charge transport.



**Figure C5.** Molecular structures of some the D-A conjugated copolymers synthesized.



**Figure C6.** Absorption spectra of the D-A copolymers as thin films.

The other copolymers with quinoxaline and pyridopyrazine acceptor moieties (PTHQx and PTDPPz) also have broad optical absorption with absorption maxima at 630–657 nm, and optical band gaps of 1.75–1.83 eV (Kulkarni et al, 2008). The cyclic voltammograms of the copolymers showed reversible redox peaks, implying that the materials may be capable of ambipolar charge transport.

We have evaluated the charge transport properties of all the D-A copolymers by using the field-effect transistor as a platform and gold source and drain electrodes (Zhu et al, 2006; Zhu et al, 2008; Kulkarni et al, 2008). The results showed that BTTP-F, PTHQx and PTDPPz have good field-effect mobilities of holes with values of  $1.6 \times 10^{-3}$ ,  $8.5 \times 10^{-3}$ , and  $4.4 \times 10^{-3} \text{ cm}^2/(\text{Vs})$ , respectively. However, n-channel field-effect characteristics and thus electron transport were not observed in any of the copolymers. This means that the materials are not ambipolar

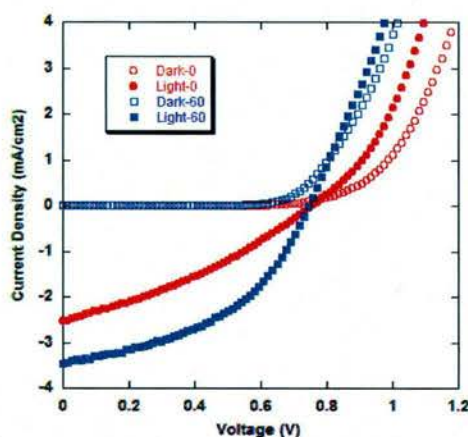


semiconductors when using the gold source/drain electrodes for charge injection under ambient air conditions. Nevertheless, the high carrier mobility the copolymers suggest that they are promising candidates for plastic solar cells if combined with a suitable acceptor material.

The photovoltaic properties of the new D-A copolymers and those of poly(3-hexylthiophene) (P3HT) were investigated by making bulk heterojunction OPV cells through blending with the [60]-fullerene derivative PCBM. The OPV cells were tested at AM 1.5 and 1

**Table C1.** Solar Cell Parameters of Solvent Annealed BTTP-F/PCBM OPV Cells Tested at 1 Sun.

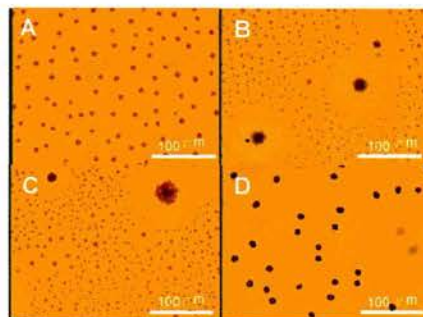
SVA Time	V <sub>oc</sub> (V)	J <sub>sc</sub> (mA/cm <sup>2</sup> )	FF	PCE(%)
0min	0.743	2.52	0.32	0.597
30min	0.748	3.02	0.41	0.931
60min	0.743	3.35	0.44	1.11
90min	0.745	3.16	0.42	0.984



**Figure C7** I-V curves of the best BTTP-F:PCBM (1:3) cells with 60 min solvent vapor annealing (blue) and without annealing (red).

efficiency of the solar cells compared to the untreated devices, from 0.6% to 1.2%. Upon examination of the thin film morphology, the appearance of ~10  $\mu\text{m}$  (diameter) and 70 nm (height) regions formed during the initial stages of solvent vapor annealing. At longer times, crystallites appeared and after 2 hrs, the entire film consisted of these large PCBM crystallites. The device parameters for the 2 hr-annealed device are not shown in the Table 1 because the crystallites were so tall that they reached the cathode, resulting in a much lower PCE (0.4%). We conclude that the optimal solvent vapor annealing time for BTTP-F:PCBM thin films in OPV cells is around 60 min. In contrast, the usual thermal annealing approach reported in the literature did not improve the device performance in the BTTP-F:PCBM cells.

sun under ambient air conditions. The P3HT:PCBM cells had a power conversion efficiency (PCE) of 2.38 % ( $J_{sc} = 7.1 \text{ mA/cm}^2$ ,  $V_{oc} = 0.6 \text{ V}$ ,  $FF = 0.55$ ). Among the D-A copolymers, we found the BTTP-F:PCBM (1:3) cells to be the most promising because of the superior thin film quality and higher molecular weight of the copolymer. The thermally annealed BTTP-F:PCBM (1:3) devices had a 0.84% PCE ( $J_{sc} = 3.20 \text{ mA/cm}^2$ ,  $V_{oc} = 0.69 \text{ V}$ ,  $FF = 0.38$ ). We discovered that solvent vapor (chlorobenzene) annealing of the photovoltaic cells significantly improved the performance (Figure C7). The solvent vapor-annealed BTTP-F:PCBM (1:3) devices had a 1.21% PCE ( $J_{sc} = 3.35 \text{ mA/cm}^2$ ,  $V_{oc} = 0.743 \text{ V}$ ,  $FF = 0.44$ ). The device performance at different solvent vapor annealing stages are shown in Table C1 and their corresponding surface morphology was observed under the optical microscope, as shown in Figure C8. For example, the I-V curves in Figure C7 show that 60 min of solvent vapor annealing process has doubled the power conversion



**Figure C8.** Optical images of at different solvent annealing stages: A) 0.5hr, B) 1hr, C) 1.5hr, D) 2hr.

### C2: Dye-sensitized solar cells (DSSC) based on ZnO (Cao)

**For dye-sensitized solar cells:** We developed and elaborated the hierarchically structured photoanodes for much enhanced power conversion efficiency. Although we started with zinc oxide photoanodes, we quickly moved to titania photoanodes and also studied the atomic layer deposition to stabilize the surface of zinc oxide photoanodes, Fig. C9. In addition to the wet chemical processing, we explored other approaches including electrospray for the fabrication of hierarchically structured photoanodes.

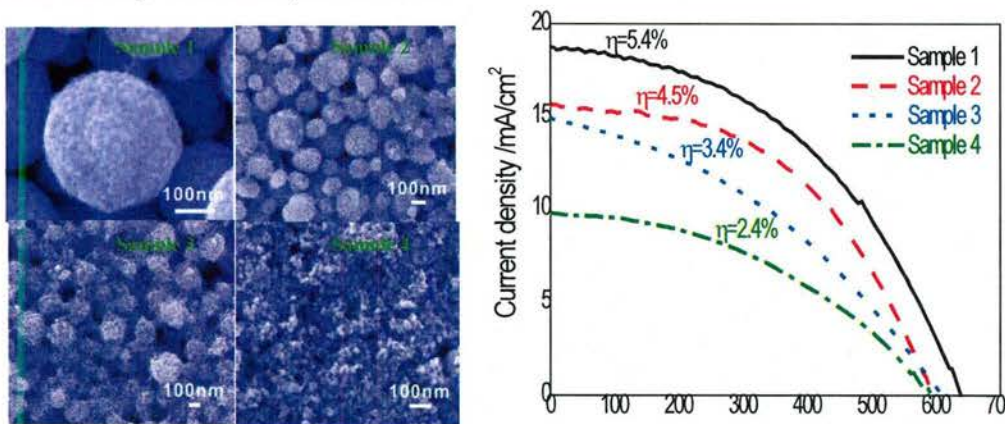


Figure C9: SEM images of ZnO nanocrystallites with perfect aggregation (top left, sample 1) to no aggregation at all (bottom right, sample 4) and the I-V curves of ZnO nanocrystallites with different degree of aggregation showing the markedly different power conversion efficiency (right). (Zhang, et al., 2008)

### C3: Design of airborne DSSCs (Taya)

In the nature, photosynthetic membrane enables the efficient conversion from light to electron and into chemical energy (Figure C10a). The photosynthesis made the fossil fuel over 200 million years by sunlight. The study of molecular assembly of chlorophyll derivatives using the light-harvesting polypeptides can be useful as a model of the natural conversion (Figure C10b). The mechanism of DSSC is similar to photosynthesis where photo conversion is carried out by the photo-excitation electron transfer of natural dyes.

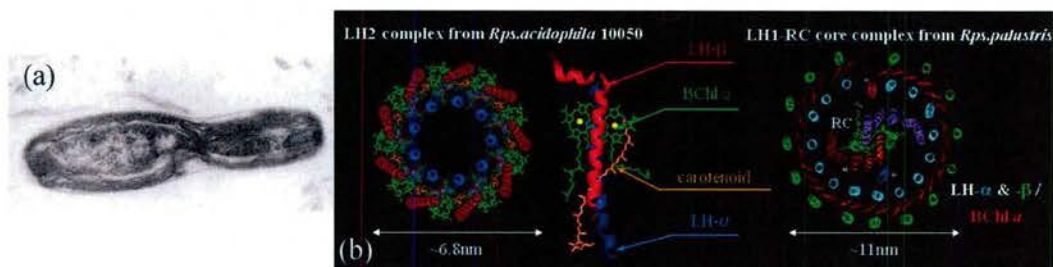


Figure C10. Bio-photo harvester (a) photo of purple bacteria, (b) show the nanostructure of hybrid structure of LH1, LH2, folding material.



The DSSC comprise four major parts: nanocrystalline titanium oxide ( $\text{TiO}_2$ ) semiconductor film, dye sensitizer, redox electrolyte, and counter electrode (Figure C11). Usually, the  $\text{TiO}_2$  with Ru complex dye can harvest the photon energy for the visible light region. In the first year, we established the processing route of DSSC samples, and the characterization of DSSC data scientifically (Figure C12), and developed DSSC with higher energy conversion efficiency close to 8 % (Figure C13).

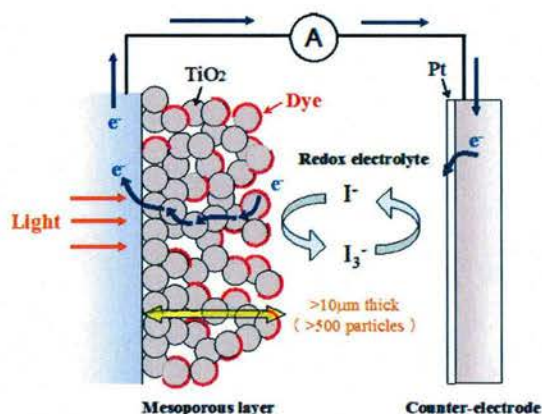


Figure C11. Schematic model and Working mechanism of DSSC

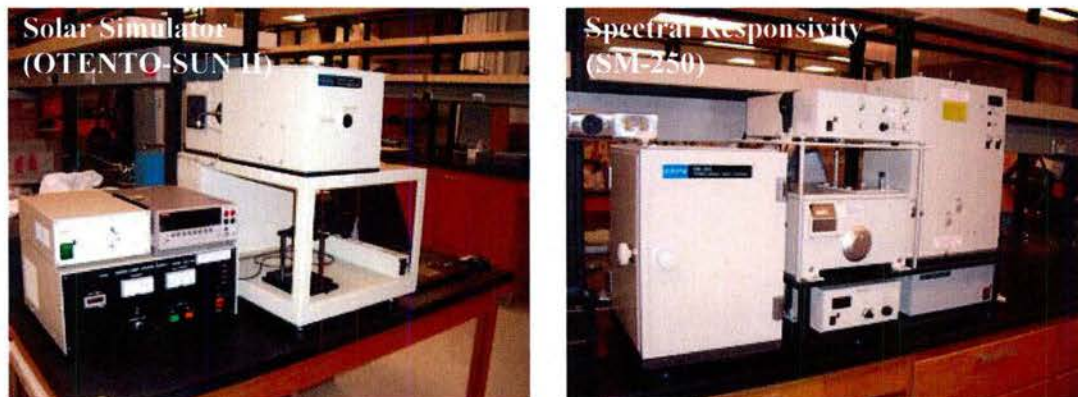


Figure C12. Photos of several new equipment.

However, the main drawback of ruthenium-based sensitizers is their lack of absorption in the red region of the visible spectrum. Phthalocyanine and naphthalocyanine dyes are well known for their intense absorption in the red and near-IR regions, therefore they are an excellent candidate as dye sensitizer of DSSC. In the first year, we synthesized phthalocyanine (Dye2) and naphthalocyanine (Dye3) (Figure C14). The dyes have absorption in the red and near-IR regions and adsorb to  $\text{TiO}_2$ . The function of the carboxylic acid group of the dyes is to graft the sensitizer onto the semiconductor surface and to provide intimate electronic coupling between dyes and  $\text{TiO}_2$ .

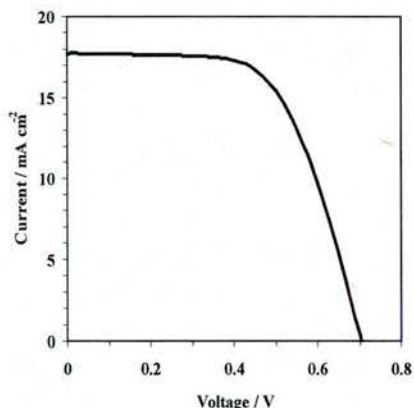


Figure C13. Current–voltage characteristic of the DSSC sensitized with the Ru complex. Conversion efficiency is 7.7%.

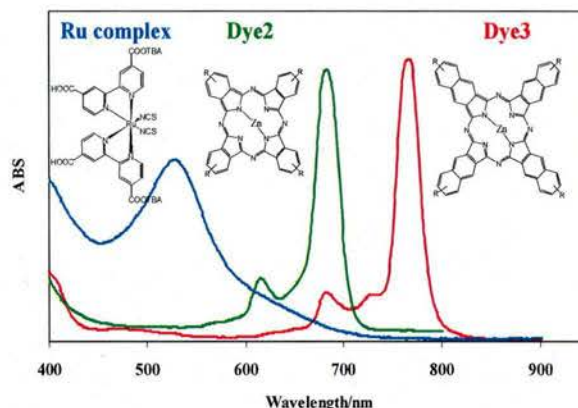


Figure C14. Absorption spectra of the dyes in a solution

TiO<sub>2</sub> film which combined Ru and Dye3 can absorb broad light waves. However the efficiency of the DSSC with such a multi-dye system was still low (2.6%), because the energy transfer between dyes occurred, whose dyes are aggregated. The aggregation of dyes in DSSC could be controlled by a ligand or a coadsorbent like a proteins or a carotenoid of photosynthesis.

Learning from this experience, we synthesized three unsymmetric ZnPc dyes, PcS2, PCS5 and PcS6, shown in Fig. C15.

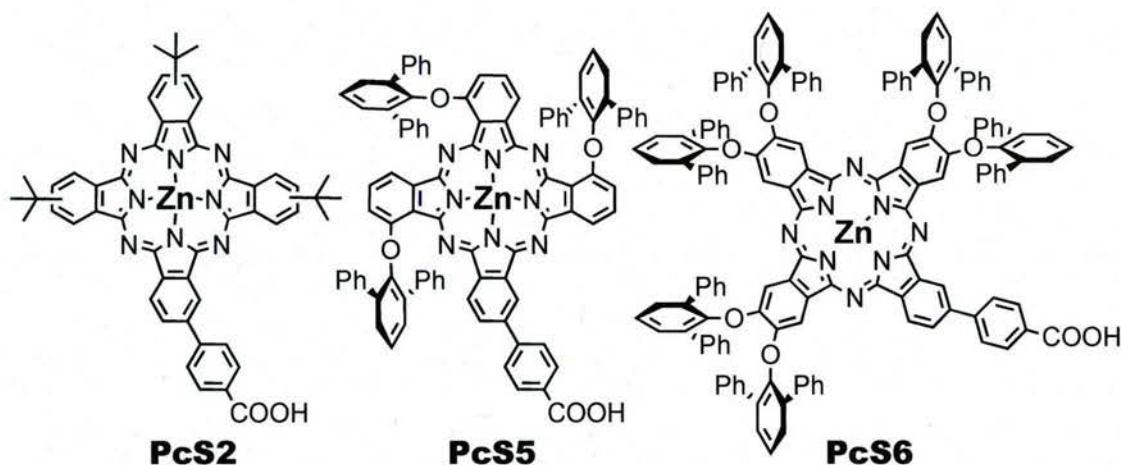


Fig. C15 Chemical structures of 3D Phthalocyanine dyes for use in the sensitizers of DSSC(Mori et al, 2010).

Figure C16 shows the absorption spectrum of **PcS2** and **PcS6** in solution and on nano-porous TiO<sub>2</sub> films without 3 $\alpha$ , 7 $\alpha$ -Dihydroxy-5 $\beta$ -cholonic acid (CDCA) as co-adsorbant. **PcS2** on the TiO<sub>2</sub> shows border absorption spectrum around 600 nm, suggesting the formation of aggregation on the surface. On the other hand, **PcS6** showed sharp Q band both in the solution and on the TiO<sub>2</sub>, showing significant decrease of the aggregation.



Table 1 summarizes I-V characteristics of the DSSCs under one sun conditions (short-circuit currents ( $J_{sc}$ ), open-circuit voltages ( $V_{oc}$ ), fill factors (FF), and conversion efficiencies ( $\eta$ )), Fig. C17 shows intrinsic power conversion efficiency (IPCE) of those dyes.

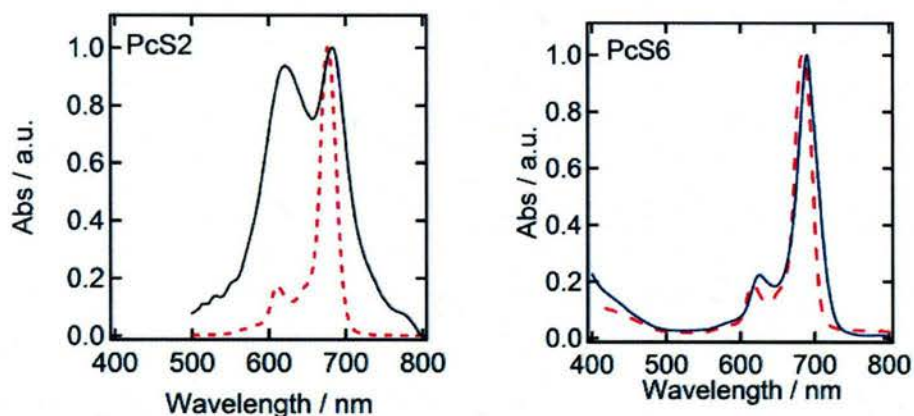


Fig. C16 Absorption spectrum of two dyes, PcS2 and PcS6 (Mori et al, 2010)

dye	$J_{sc}$ (mA/cm <sup>2</sup> )	$V_{oc}$ (V)	Fill Factor	PCE (%)	IPCE(%)
PcS2 <sup>b</sup>	5.3	0.58	0.74	2.3	30
PcS5 <sup>b</sup>	4.8	0.58	0.77	2.1	52
PcS6 <sup>c</sup>	10.4	0.63	0.70	4.6	78
N719 <sup>c,d</sup>	14.4	0.71	0.67	6.9	86

Table C2. I-V characteristics of DSSCs<sup>a</sup> with various dyes under one sun conditions and the values of maximum IPCE. <sup>a</sup>: TiO<sub>2</sub> electrode consisted of a 7-8 nm thick nanoporous layer with a 5-6 nm scattering layer with TiCl<sub>4</sub> treatment. The electrolyte was 0.1 M LiI, 0.6 M DMPII, 0.05 M I<sub>2</sub> and 0.5 M tBP in acetonitrile. The measurement used an aperture mask with area of 0.17 cm<sup>2</sup>. The area of TiO<sub>2</sub> was ~ 0.14 cm<sup>2</sup>. <sup>b</sup>: with 10 mM CDCA in the dye solution. <sup>c</sup>: Without CDCA, <sup>d</sup>: N719 is a Ru complex dye.

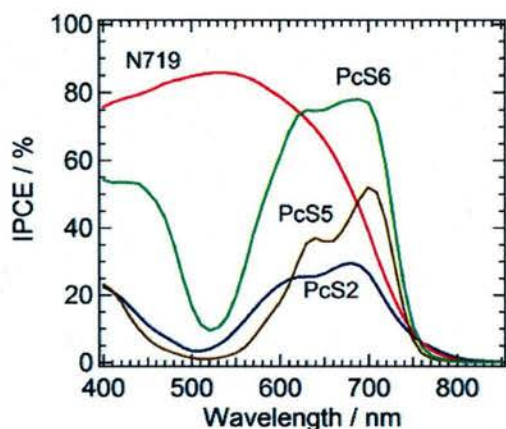


Figure C17. IPCE of Dye-sensitized solar cells with four different dyes. The cells were the same examined on Table C2 (Mori et al, 2010)

In contrast to **PcS2**, **PcS6** showed the high performance,  $\eta$  of 4.6 % under one sun conditions. To the best of our knowledge, this  $\eta$  value is the highest efficiency reported so far among the DSSCs using ZnPcs as a light harvesting dye.

We used commercial dye N719 to design two glass-based DSSCs and a flexible PET film based DSSC where we used standard solution iodine electrolyte, see Table C3. A comparison of these designs is shown in Table C4. The I-V curves of these three DSSCs are shown in Fig. C18.

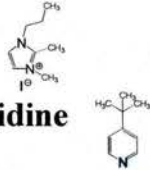
<b>0.05M</b>	<b>Iodine</b>		} <b>0.8M I<sup>-</sup></b>
<b>0.1M</b>	<b>Lithium iodide</b>		
<b>0.6M</b>	<b>DMPIImI</b>		
<b>0.5M</b>	<b>4-tert-Butylpyridine</b>		
in acetonitrile CH <sub>3</sub> CN			

Table C3 Electrolyte solution used to evaluate DSSC performance of Table C4.

	<b>Glass DSSC</b> (2.5mm FTO)	<b>Glass DSSC</b> (1.1mm ATO)	<b>Flexible DSSC</b> (125 $\mu$ m ITO-PET)
<b>Efficiency (PCE)</b>	<b>10.3%</b>	<b>9.6%</b>	<b>6.0%</b>
<b>Thickness</b>	<b>5 mm</b>	<b>2.2 mm</b>	<b>0.3 mm</b>
<b>Weight</b>	<b>0.88 g / cm<sup>2</sup></b>	<b>0.33g / cm<sup>2</sup></b>	<b>0.053 g / cm<sup>2</sup></b>
<b>Sintering Temp.</b>	<b>~500°C</b>	<b>~500°C</b>	<b>~130°C</b>
<b>Specific PCE (PCE/weight)</b>	<b>12 % (cm<sup>2</sup>/g)</b>	<b>29 % (cm<sup>2</sup>/g)</b>	<b>113% (cm<sup>2</sup>/g)</b>
	<b>1</b>	<b>:</b>	<b>2.4</b>
		<b>:</b>	<b>9.4</b>

Table C4 The power conversion efficiency (PCE)s and thickness of substrate, weight, sintering condition and specific PCE of two glass based DSSCs, one flexible PET film based DSSC

It is noted from Table C4 that the flexible PET based DSSC has the highest specific PCE thanks to its lowest weight as compared with glass substrates, even if the PCE of the flexible DSSC is the lowest among these.



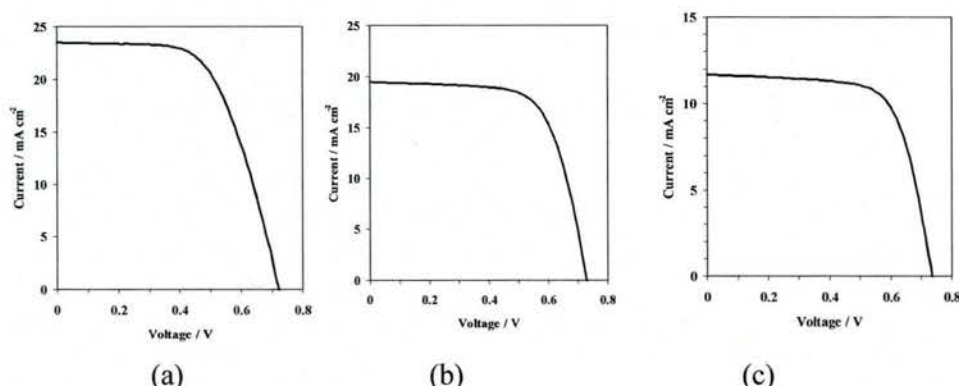


Fig. C18 I-V curves of three different DSSCs corresponding to three designs in Table C3, based on three different substrates, (a) thick FTO glass, (b) thin ATO glass and (3) thin flexible PET.

Even if we demonstrated high PCE of DSSCs based on both glass and flexible PET substrate in Table C4 and Fig. C18, they are all based on liquid electrolyte of Table C3, thus, they may not be durable for longer flight time of a MAV or UAV mounted with such DSSCs. Therefore, we developed a new gel electrolyte which is in form of gel (or solid state), thus least likely for leakage from the DSSC package. Table C5 shows the DSSC performance based on several different electrolytes, (i) solution electrolyte, (ii) ionic electrolyte and (iii) gel electrolyte.

### Electrolyte for DSSC

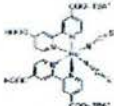

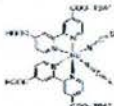
Electrolyte	operating temperature limit	Dye	PCE
<b>Liquid base</b> mixture of acetonitrile and valeronitrile (85:15)  $T_m = -48^{\circ}\text{C}$ $T_m = -96^{\circ}\text{C}$ $T_b = 81-82^{\circ}\text{C}$ $T_b = 139-141^{\circ}\text{C}$  0.6M BMII, 0.03M $\text{I}_2$ , 0.1 M guanidinium thiocyanate, and 0.5M tert-butylpyridine	( $-50^{\circ}\text{C} \sim 80^{\circ}\text{C}$ )	<b>N719</b>  Md. K. Nazeeruddin et. al, JACS, 127, 16835 (2005)	11.18%
<b>Ionic liquid base</b> 1-ethyl-3-methylimidazolium tetracyanoborate (EMI-TCB)/  $T_m = \text{less than } 0^{\circ}\text{C}$  DMII / EMII / $T_m = 81-83^{\circ}\text{C}$ $T_m = 79^{\circ}\text{C}$  $\text{I}_2$ / N- butylbenzimidazole / guanidinium thiocyanate (molar ratio: 16/12/12/1.67/3.33/0.67)	(more than $0^{\circ}\text{C}$ )	<b>C103</b>  D. Shi et. al., J. Phys. Chem. C, 112, 17047 (2008)	8.5%
<b>Gel base</b> 10wt% PVDF-HFP with 3-methoxypropionitrile (MPN)  $T (\text{brittleness}) = -62^{\circ}\text{C}$ $T_m = -62.9^{\circ}\text{C}$  $T_m = 140-145^{\circ}\text{C}$ $T_b = 164-165^{\circ}\text{C}$  0.6M DMPII, 0.1M LII, 0.1M $\text{I}_2$ , 0.45M N-methyl-benzimidazole, 10wt% $\text{TiO}_2$ nano powder (P25)	( $-60^{\circ}\text{C} \sim 160^{\circ}\text{C}$ )	<b>N719</b>  Z. Huo et al, Solar Energy Materials & Solar Cells, 91, 1959 (2007)	7.18%

Table C5 DSSCs based on three different electrolytes

We optimized the gel electrolyte so as to increase the PCE of the DSSC where the requirement of the use of such DSSC in lower temperature (up to  $-160^{\circ}\text{C}$ ) is met with this gel electrolyte, the results of which are shown in Table C6 where the comparison is between the DSSC based on liquid and gel electrolytes.

### Electrolyte of Glass based DSSCs

Liquid	Gel
<b>Efficiency (PCE)</b>	
<b>10.3%</b>	<b>7.8%</b>
<b>Thickness</b>	
<b>5mm</b>	<b>1.4mm</b> (1.1mm ATO + ITO-PET) thinner glass
<b>Weight</b>	
<b>0.88 g / cm<sup>2</sup></b>	<b>0.19 g / cm<sup>2</sup></b>
<b>4.6</b>	<b>1</b>
<b>Sintering</b>	
<b>~500°C</b>	<b>~500°C</b>
<b>Specific PCE (PCE/weight)</b>	
<b>12 % (cm<sup>2</sup>/g)</b>	<b>41% (cm<sup>2</sup>/g)</b>
<b>1</b>	<b>3.4</b>

**Gel electrolyte:**

$\left[ \text{CF}_2 - \text{CF}(\text{CF}_3) - \text{CF}_2 - \text{CF}(\text{CF}_3) \right]_x$   
 $\left[ \text{CF}_2 - \text{CF}(\text{CF}_3) - \text{CF}_2 - \text{CF}(\text{CF}_3) \right]_y$   
**5wt% PVDF-HFP**

H3COCH2CH2CN  
**MPN**

**0.12M I<sub>2</sub>, 0.2M TBP**  
C1CCN(C1)C(C)C

**0.7M MPImI, 0.1M TBAI**  
C1CCN(C1)C(C)C

Table C6 Two different electrolytes, (i) liquid and (ii) optimized gel electrolyte.

### Larger sized DSSCs

If the proposed DSSC is to be used for top surface of wings in UAV, use of larger surface DSSC is desired. To this end, we developed a processing route for making larger sized glass substrate with Ni mesh pattern, shown in Fig. C19. This substrate was processed first making the meshed groove lines by using Si-lithography with polymer resist, followed by the electroplating of Ni into the groove, then removing the polymer resist to complete the final Ni-meshed pattern on FTO glass substrate. Similar scheme was applied to Flexible ITO film.

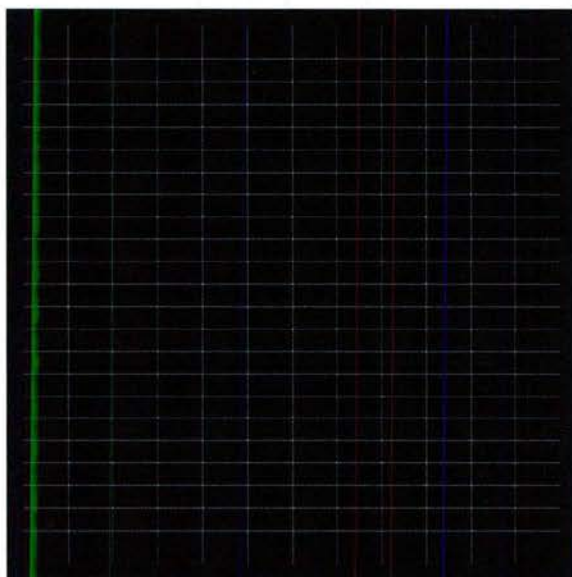


Fig. C19 Large sized DSSC of 12 cm x 12 cm with Ni meshed line where unit rectangular cell size being 10 mm x 5 mm.



## Bioinspired moth-eye surface for airborne DSSCs

In order to harvest the solar energy over the entire daylight time when sun is out, we employed Bioinspired design of anti-reflection coating, so called, moth-eye film to be placed on the top of the airborne DSSC plate.

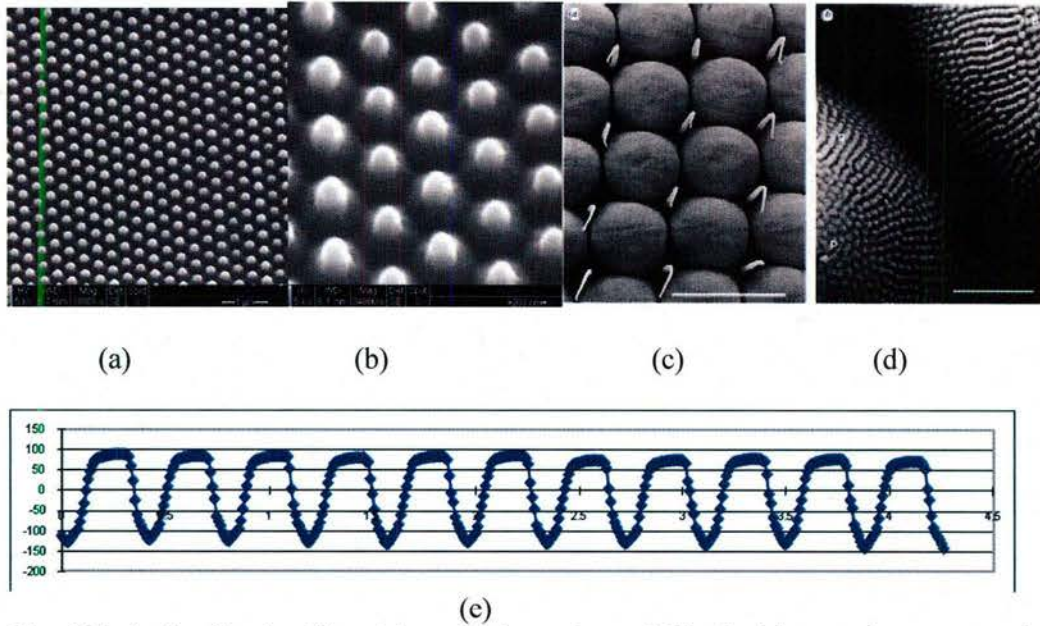


Fig. C20 Anti-reflection film, (a) synthetic moth-eyed film by blue-ray laser processing, (b) its enlarged view, (c) and (d) are the corneal surfaces of the Eocene Fly (Parker et al 1998), (e) the measured profile of the moth-eye of (a), (b) indicating the height and pitch being 250 nm and 200 nm, respectively.

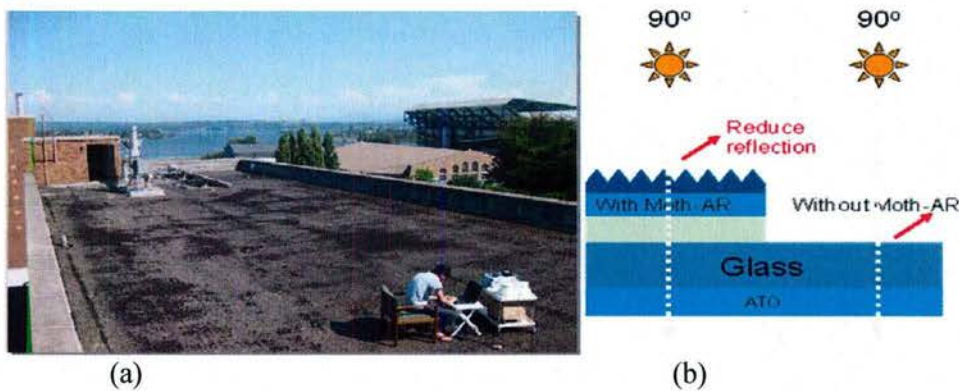


Fig. C21 (a) Field Experimental set up to measure the effectiveness of using moth-eye anti-reflection (AR) film on glass substrate (b) glass substrate with and without moth anti-reflection (AR) film.

We did study experimentally the transmittance of the film with and without the above moth-eye film under realistic sun light in Seattle. Fig. C21 shows the experimental set up. The results of transmittance of the substrate glass with and without moth-eye film are shown in Fig. C22 which indicates the higher transmittance through the moth-eye film.

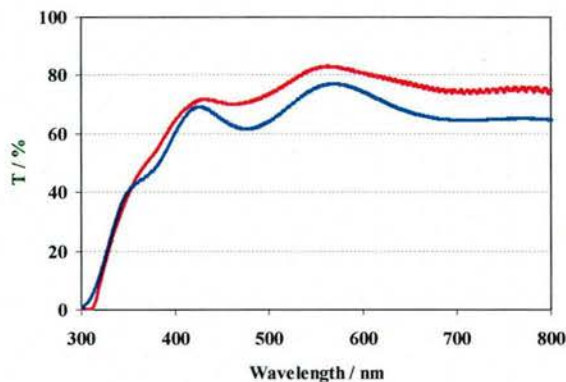


Fig. C22 Transmittance of solar light through glass with (red, top curve) and without (blue bottom curve) moth-eye AR film.

#### Task D: Integration of EHSS components into load-bearing structures(Hahn,Taya, Feraboli and Chasiotis )

##### D1 UCLA achievements

Multifunctional integration of solar and thermal energy harvesting structures is expected to play a key role in powering a wide variety of devices and systems of interest to the Air Force, including sensors for structural health monitoring and unmanned aerial vehicles (UAVs). However, little work has been reported in the literature on the performance of energy harvesting structures under mechanical stress.

During the first project year, we have developed multifunctional characterization capability for solar energy harvesting devices and performed a systematic investigation of the performance of commercially available solar modules under tensile loading. Our effort resulted in one MS thesis, one manuscript submitted for presentation at a workshop, and one manuscript in preparation for submission to an archival journal.

##### 1) Structural/mechanical characterization of solar modules

We have developed expertise to use SEM, EDX, in combination with optical microscope to identify device structures at microscopic levels. Since few mechanical properties of solar modules are available in the literature, we have also developed mechanical testing setup/procedures to determine the Young's modulus and fracture strength of solar energy harvesting modules.

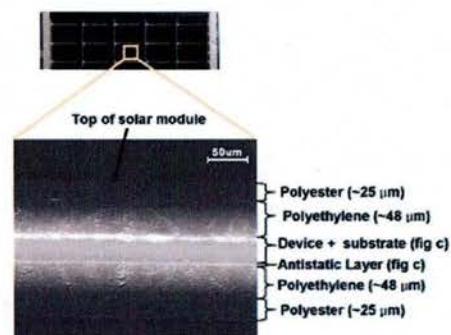


Figure D1 SEM micrograph of a commercial a-Si solar cell module.



## 2) Multifunctional characterization of solar modules

We have developed a specialized experimental setup consisting of a versatile mechanical tester (Instron 4483), a light illuminator, a precision current-voltage source-meter, and a data acquisition system for strain measurements. This setup allows us to determine functional (energy harvesting) characteristics of a module under various mechanical loading conditions. Tests can be performed under monotonically increasing load or cyclic load conditions.

From the I-V characteristics measured at different load conditions, we extract key metrics of solar modules, including the short circuit current, open circuit voltage, fill factor, and maximum power point. Under the monotonic load condition shown in Figure D2 (left), the short circuit current first decreased approximately linearly with increasing strain for commercial a-Si solar cells we tested. Immediately preceding fracture, the degradation in the short circuit current accelerated.

Under cyclic loading conditions, the short circuit current density stayed relatively constant and equal in both the stressed and relaxed state up until approximately 1.4% strain. Above 1.4% strain, the current density did not fully recover when the load was removed due presumably to plastic deformation.

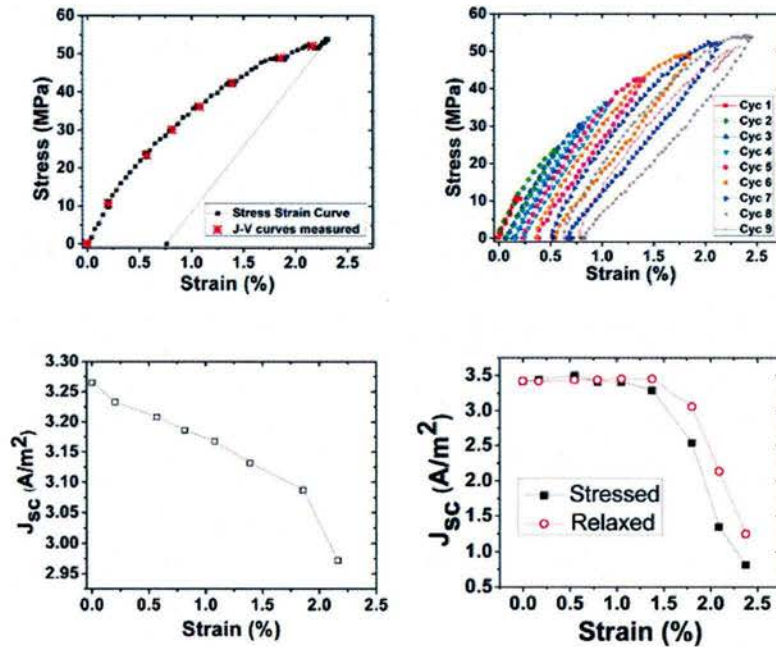


Figure D2 Stress-strain relations and short-circuit current density of a-Si solar modules under monotonic (left column) and cyclic (right column) loading

### 3) Characterization of microstructural changes

We used optical and SEM characterization to relate the observed performance degradation to micro-structural changes in the form of cracking under applied stress. We custom-built a long-working distance optical microscope with x-y-z translation capability that is compatible with our multifunctional characterization facility.

Localized cracks are believed to initiate in the brittle device layers of the solar cell modules at a strain level as small as 0.3%. The performance does not degrade significantly because there is still a clear current path in the device. When the load is removed, the cracks can be closed, allowing the device performance to be recovered. At strains larger than approximately 1%, large cracks develop at the interface between two adjacent segments through the entire width of the module, which cannot be completely “healed” after the load is released due to the viscoelastic behavior of the polymer encapsulation layers. An image of the fractured solar module show that the polymer layers did not fracture and that the cracks propagate from the inner device layers.



Figure D3 Custom-built long-working distant video microscope.

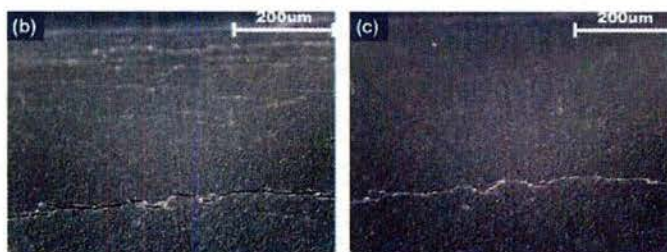


Figure D4 (b) Typical microscope image at approximately 1.40% in the stressed state (c) and the relaxed state showing the cracks getting smaller as stressed is released from the cycle test. The large crack extends throughout the entire width of the solar module.



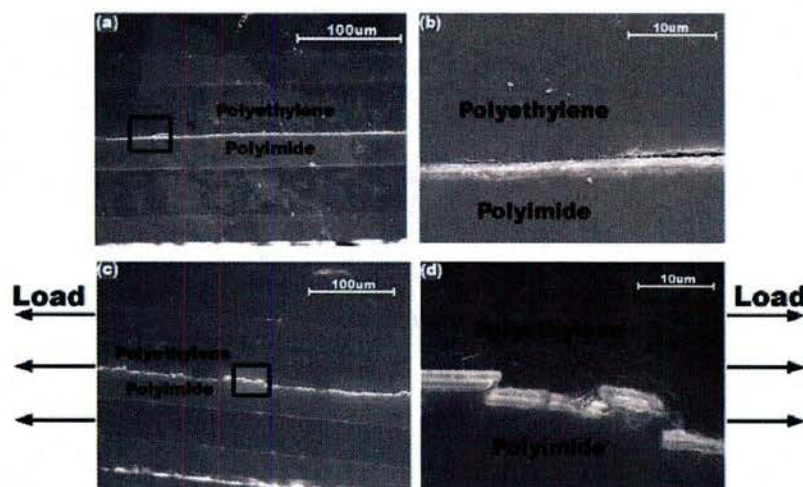


Figure D5 (a) Cross section of an unstressed solar module where (b) is zoomed in on the device layers. (c) Cross section after the cycle test where (d) shows the cracks in all of the device layers. The arrows indicate the load direction.

#### Accomplishments and Discoveries

- c-Si solar cells are very brittle; a failure occurs below 0.2%-tensile strain.
- A functional performance of the  $\alpha$ -Si solar cell was gradually degraded due to cracks on a zinc oxide and amorphous silicon layers above 0.38%-strain. (Fig. D6)
- After a uniaxial pressure of 0.83 MPa, the capacity of solid-state thin-film lithium batteries started to drop. For deflections higher than 0.25 mm for the linear span length of 19 mm, the charging and discharging capacity of the solid-state thin-film lithium batteries decreased. These were due to the breakage of packaging materials and internal layers such as lithium phosphorus oxynitride (LiPON) solid electrolyte, and the oxidation of active materials. Solid-state thin-film lithium batteries can be embedded into graphite/epoxy laminates if the curing temperature does not exceed 122°C. The functional performance of the solid-state thin-film lithium batteries deteriorates rapidly with mechanical fatigue cycles. The maximum fatigue strain that can be applied without degrading the functional performance up to 1000 cycles is only 0.07%. (Fig. D7)
- A conductive path was made using inkjet printing of copper ink. Resistivity of printed electrode using our copper nanoparticles was 36.7 n $\Omega$ ·m. The printed electrodes remain fully functional up to the maximum strain of 1%. (Fig. D8)
- A power laminate has been fabricated by first mounting a thin-film solar module and a thin-film battery on a BT core with the desired printed conductive pattern, and then co-curing the resulting assembly with a graphite/epoxy composite laminate. (Figs. D9 and D10)

- The energy harvesting/storage characteristics of the developed multifunctional composite structure were measured under the mechanical static loading condition. From the experiment, it was found that the power laminate was reliable until 0.45% of the static strain. After 0.45% of the strain level, the active layers of the solid-state thin-film lithium battery was failed.
- The Li-ion polymer battery by Dow Kokam was characterized. This battery was able to achieve 100% depth of discharge at a low temperature of  $-27^{\circ}\text{C}$  under 1/12 C-rate. Under compression, the packaging of the battery was able to withstand 22.8 MPa, and under tension, these batteries were able to endure 1.655% strain without decrease in its capacity. The Li-ion polymer battery should not be embedded by co-curing method inside a CFRP composite laminate because its capacity decreased under fatigue loadings. When the Li-ion polymer battery was charged, the thickness of the Li-ion polymer battery was increased by  $48 \pm 5 \mu\text{m}$  on average, compared to the thickness of the completely discharged Li-ion polymer battery. In contrast, when the Li-ion polymer battery was discharged, the thickness of the Li-ion polymer battery decreased by  $46 \pm 5 \mu\text{m}$  on average, compared to the thickness of the completely charged Li-ion polymer battery.
- An IPL system was developed to sinter different materials instead of a thermal chamber. Both semiconductor and metallic nanoparticles can be sintered on a composite laminate using an intense pulsed light. This opens up an avenue for fabricating solar cells and conducting circuits directly on composite laminates. (Fig. D11)
- The IPL can sinter the copper nanoink. The sintered copper film has a grainy structure with neck-like junctions. The film has  $5 \mu\Omega\cdot\text{cm}$  of electrical resistivity which is one third that of previously reported thermally sintered copper nanoink.
- A silver conductive pattern made by inkjet printing was sintered IPL. Using a lumped capacitance method, it was found that IPL irradiation of  $50 \text{ J/cm}^2$  increases the temperature of the printed silver nanoink pattern by  $500^{\circ}\text{C}$ . The average resistivity of the fully sintered silver pattern was  $49 \pm 3 \text{ n}\Omega\cdot\text{m}$ . IPL sintering is more appropriate for protecting the substrate rather than a conventional thermal sintering process. (Figs. D12 and D13)
- CIGS films were prepared from CIG metallic alloy and Se nanoparticles using the IPL technique without toxic selenization or vacuum conditions. (Fig.D14)
- Unidirectional stretching was applied to improve the optical and electrical properties of a dilute CNT mat. After the dilute CNT mat on a polyvinyl chloride film was stretched by 80% strain, it reached the average sheet resistance of  $213 \Omega/\square$ .



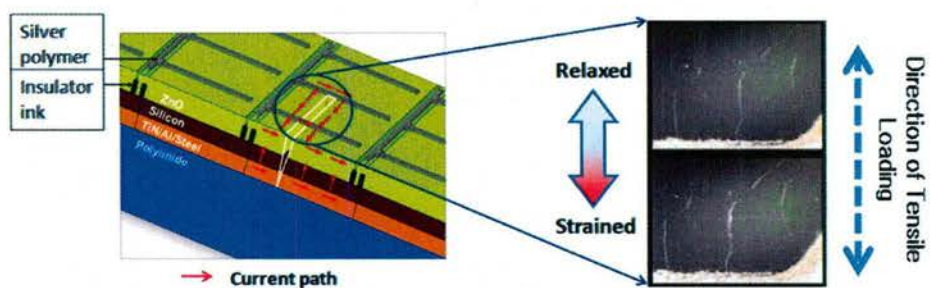


Fig. D6 Crack propagation on amorphous silicon layer due to tensile loading.

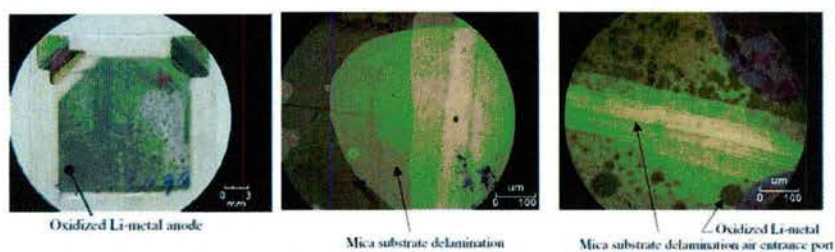


Fig. D7 Thin-film solid-state lithium battery.

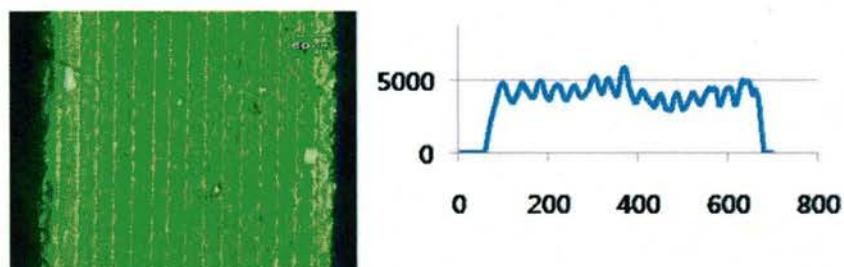


Fig. D8 (a) Optical microscope image, and (b) profilometer results of a printed electrode.

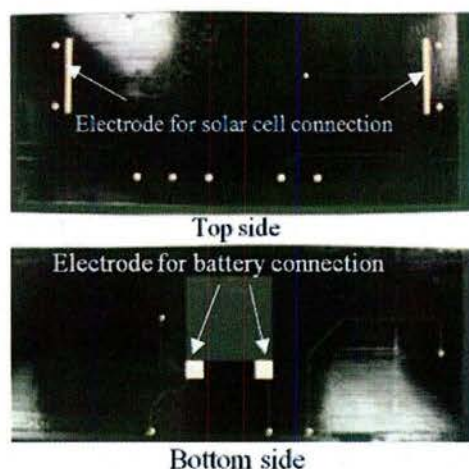


Fig. D9 Printed and sintered conductive circuit for power laminate.

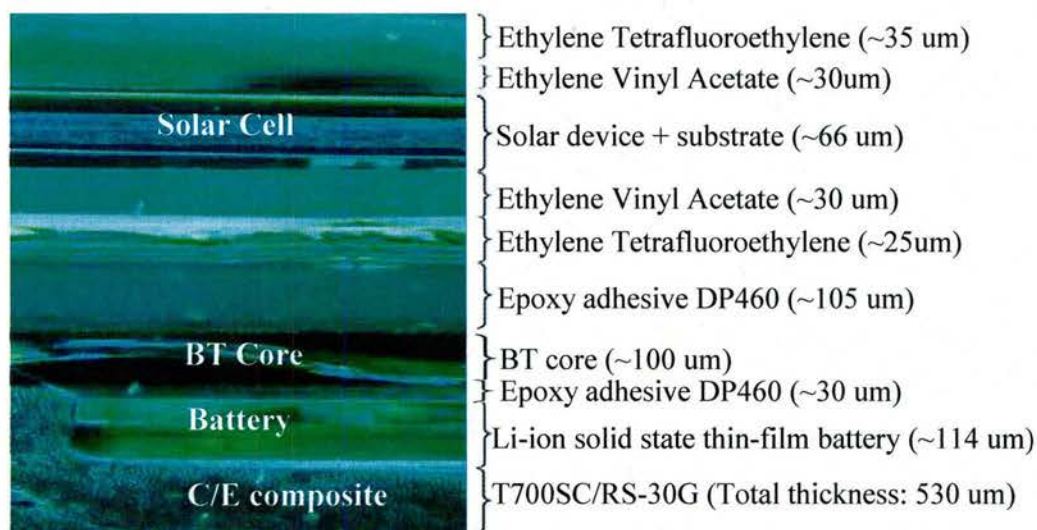


Fig. D-10 Cross sectional view of the composite laminate with integrated solar cell and embedded battery.

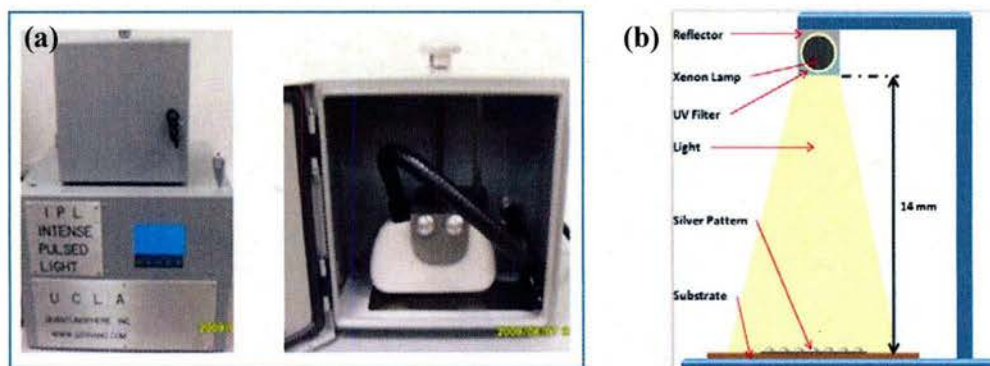


Fig. D11(a) Actual IPL system, and (b) schematic drawing of IPL system.



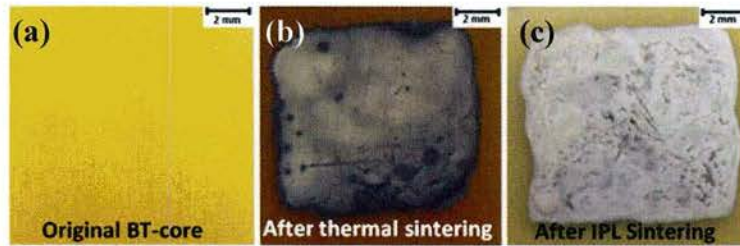


Fig. D12 (a) Original BT core, (b) BT core after thermal sintering at 200°C, and (c) BT core after IPL sintering.

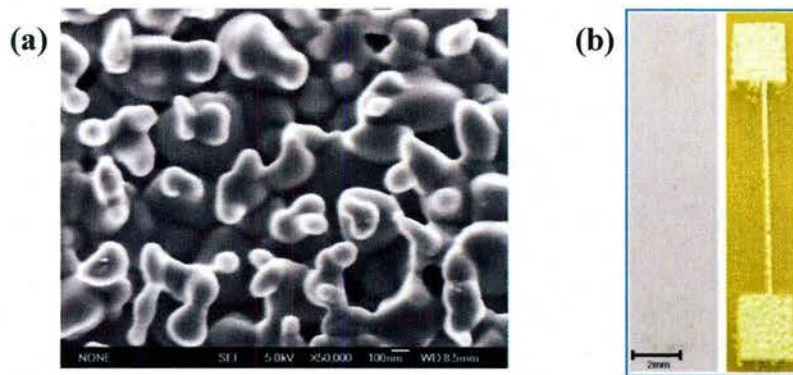


Fig. D13 (a) SEM image of the surface, and (b) adhesive tape test of the silver nanoink pattern after three consecutive IPL pulses at 50 J/cm<sup>2</sup>.

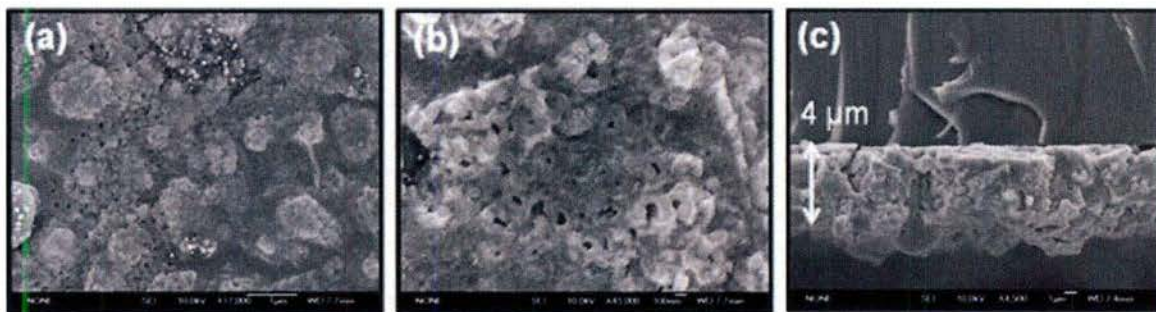


Fig. D14 (a) Overall surface morphology SEM image, (b) image at higher magnification, (c) cross-section SEM image of CIGS film prepared on glass substrate after IPL pulse at 20 J/cm<sup>2</sup>.

## D2 University of Washington achievements

### D2-1 Integration of DSSC to structures(Taya)

Taya group at UW studied experimentally the residual solar cell performance of a DSSC which was subjected to mechanical fatigue loading where two different bonding conditions are used, (1) bonding condition 1 : each DSSC is strongly bonded to the substrate surface, (2) bonding condition 2: top polymer film covering all DSSCs are bonded only along its periphery while each

DSSC is merely compressed by the top polymer film. In our experiment, we mounted only one DSSC sample on the substrate which is then subjected to bending strain test, see Fig. D16.

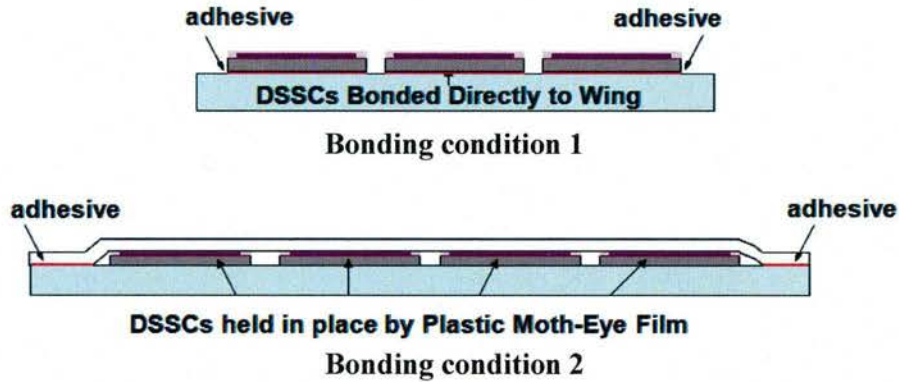


Fig. D15 Two different bonding of DSSCs on the substrate, (1) each DSSC is bonded strongly to the substrate surface, (b) polymer adhesive covering all DSSCs is bonded in its periphery while each DSSC is just mechanically compressed to the substrate.

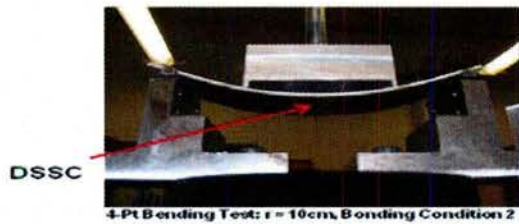


Fig. D16 Four-point bending test on the substrate attached with DSSC at its bottom.

The results of the cyclic bending tests of the DSSC mounted on the substrate are given in Table

	Sample #	Failure Strain ( % $\epsilon$ )				Average
		1	2	3	4	
Bonding Condition 1	Tension	0.06%	0.16%	0.10%	0.06%	0.08%
	Compression	0.10%	0.06%	0.16%	0.24%	0.11%
Bonding Condition 2	Tension	0.24%	0.24%	0.24%	0.24%	0.24%
	Compression	0.24%	0.24%	0.24%	0.24%	0.24%

Table D1 Failure strain of the DSSC mounted on the substrate subjected to one time static bending test, indicating that the DSSC with bonding condition 2 has higher failure strain, better design.

Then we made cycling bending test of the glass-based DSSC with bonding condition 2 to study the durability of the DSSC . The results are given in Fig. D17 to find that the glass DSSC has longer life with even its PCE slightly increasing.



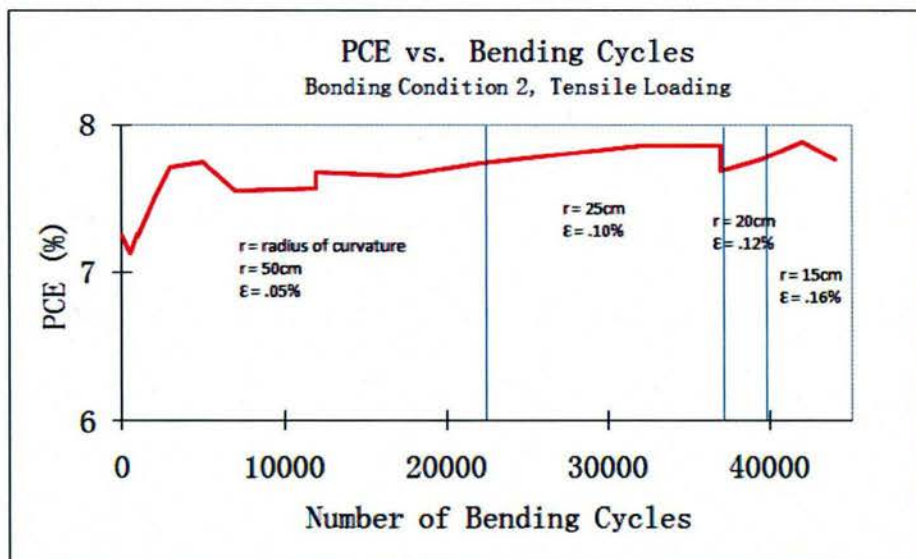


Fig. D17 Residual performance (power conversion efficiency (PCE)) of the DSSC subjected to cyclic bending up to 40,000 cycles with bending strain of 0.1 %.

We also performed similar cyclic test on flexible PET DSSC sample, the results of which are summarized in Fig. D18.

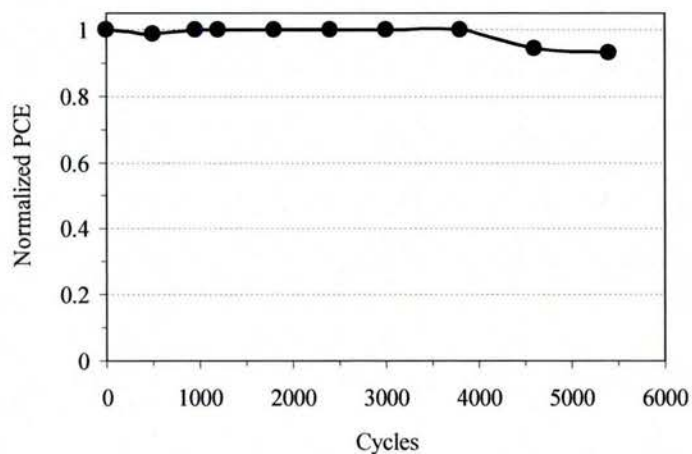


Fig. D18 Normalized PCE of flexible PET based DSSC subjected to cyclic bending loading of up to 5,500 cycles with little degradation of the residual PCE of the DSSC.

## **D2-2 Integration of thin film Li-ion batteries into structural laminated composites: limits of process-ability and electromechanical performance (Feraboli)**

### **1. INTRODUCTION**

The flight endurance of an electric propeller-driven unmanned aerial vehicle (UAV) is significantly improved by reducing the weight more so than increasing the battery capacity (Thomas, 2002). Moreover the structure and the battery each contribute typically 20-40% to the total UAV mass (Thomas, 2002; Thomas, 2004). The integration of battery and structure can theoretically reduce the total weight by reducing the sum of the structure and the battery weight. This would be accomplished by exploiting the battery components as load bearing elements and by eliminating battery fittings or supports. In addition, rather than bulky, centralized batteries, the integration of multiple lightweight batteries into the structure enables distributed power supply and storage, thereby reducing the amount of wiring. However, to date, system performance improvements achieved with such integration have been documented only for low mechanical stress demanding applications (Thomas, 2005), and the current battery technology, based on micro-structured lithium intercalation compounds, is such that high specific energy, as well as specific power, and good mechanical properties cannot be contemporary achieved (Thomas, 2005; Qudway, 2005; Liu, 2008; Snyder, 2009(a); Snyder, 2009(b)). In order to meet the requirements for the next generation of airborne, load bearing batteries, thin film Li-ion batteries (TFB) have been recently proposed (Xu, 2008; Pereira, 2006; Pereira, 2008(a); Pereira, 2008(b); Pereira, 2009). The thin film structure maximizes the specific contact surface between electrodes and electrolyte, thereby increasing the electric energy and power stored per unit mass by increasing the fraction of reactants and the rate of the electrochemical reaction respectively. Moreover scalable manufacturing processes for nanostructured materials, such as electrospinning, chemical vapor deposition (CVD), atomic layer deposition (ALD), are suitable for TFB manufacturing. The nano-scale technology applied to the battery active components can potentially lead to several advantages. It allows further increase of TFB capacity and power by decreasing the path length of Li-ion and electronic transportation (Liu, 2009; Wang, 2008; Scott, 2011). It can also enable the simultaneous implementation of electric energy storage and load bearing capabilities through engineered composite electrodes comprised of electrochemically active particles or fibers bound by a structural matrix with electrically conductive filler. Lastly it allows better accommodation of the cycling strain induced by Li-ion insertion and removal, which causes low durability and capacity fading during operation of conventional bulk material electrodes, in particular if Silicon is used as anodic material for high specific capacity (Chan, 2008; Trevey, 2011; Son, 2011). The low TFB thickness, typically less than 300  $\mu\text{m}$ , facilitates the integration within thin section structures, but it implies that a significant weight fraction is constituted by the packaging layers, which provide mechanical support for the battery manufacturing process, electrical insulation and sealing of the highly reactive cell components, Figure D19-20.



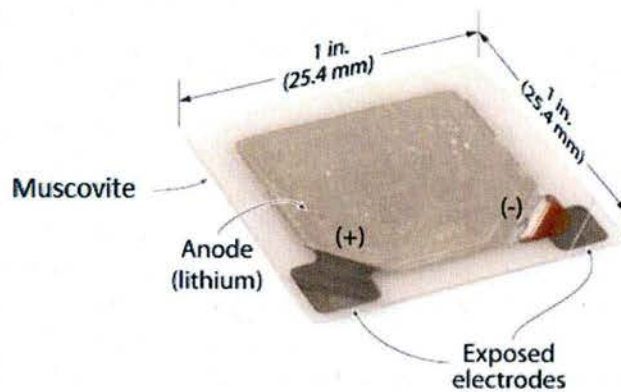


Figure D19. Perspective photo of all-solid state thin film Li-ion battery (TFB) with dimensions. Manufactured by FrontEdge Technology Inc.

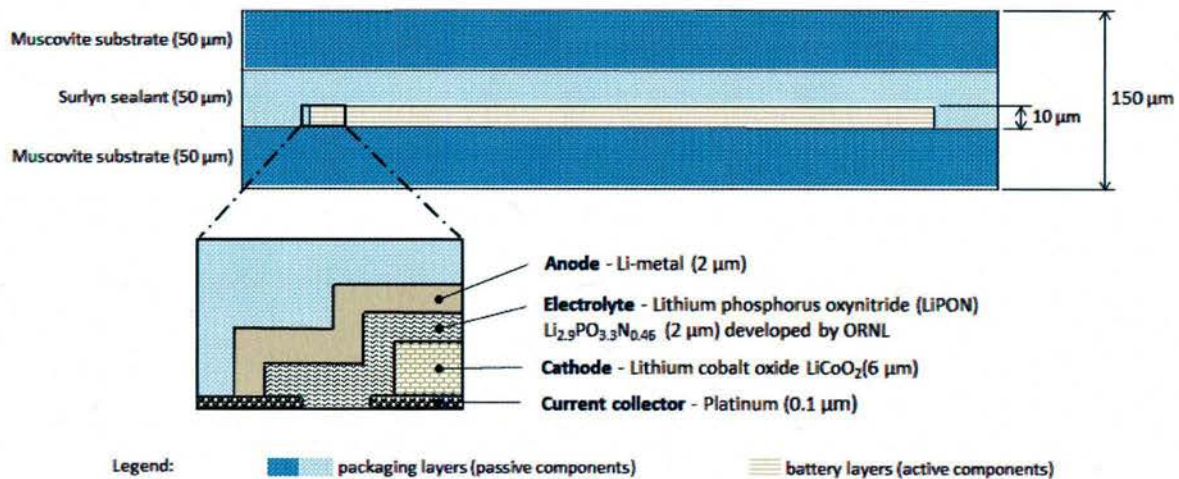


Figure D20. TFB Cross-sectional schematic

This is a deterrent for most large-scale applications of TFBs, which are indeed employed as power sources for memory chips, microelectromechanical systems (MEMS) and medical implantable devices. However if the packaging is by design an active load bearing element, instead of a passive battery mass, then this technology becomes an appealing multifunctional system for electric propelled air vehicles. Low-power applications such as, for example, integrated power source for an embedded health monitoring system of smart composite structures, can also be enabled without the need of a load bearing battery design. The manufacturability and functionality of the integration between structural composite laminates and TFBs have to be proved in terms of physiochemical compatibility of TFB materials to the composite curing environment, durability of the electrodes, laminate structural integrity and TFB packaging integrity under applied loading. Mechanical tests conducted on a commercially available TFB by (Pereira, 2008) show that the battery is capable to withstand uniaxial transverse

pressure up to 830 kPa without any detrimental effects on the electric functionality, thereby proving that the TFB is compatible with the autoclave curing pressure of epoxy-based composite materials. The aforementioned result has been corroborated by this laboratory. The same TFB has been successfully embedded in a carbon/epoxy composite laminate cured at 121°C, while failure has been documented for a 177°C embedding (Pereira, 2008), giving evidence that the processing temperature is an influential parameter for battery survivability. The TFB ability to tolerate the exposure to curing temperature, which ranges from 121°C to 177°C, in a quiescent status (e.g. with no electric current flow) is neither fully covered by scientific literature, nor by commercial electronics standards. On the other hand the ability to operate from -55°C to 100°C has been extensively investigated because of the relevant commercial applications. High temperature characterization of TFB, having the same chemistry of the batteries tested in the present study, has been performed under charge/discharge cycling (e.g. not in a quiescent status) and permanent capacity reduction has been detected at 80°C (Nagasubramanian, 2004). In (Van Sluytman, 2006) cycling at 100°C and 150°C causes permanent capacity reduction associated to a decrease in grain dimension of the  $\text{LiCoO}_2$  cathode. When the battery is processed at the same temperatures in a quiescent status and brought back to room temperature, no change in capacity and no cathode crystallographic change are noted. However the state of charge of the quiescent battery is unknown. The increasing detrimental effect of temperature exposure at increasing state of charge (Thomas, 2003) up to thermal runaway (Roth, 2003) has been studied only for conventional 18650 Li-ion cells, not for TFBs. The objective of this study is to experimentally assess the limits of process-ability of a commercially available TFB within composite curing temperature, pressure and liquid resin environment, in order to enable the manufacturing of composite laminates with embedded or externally bonded TFBs. The research covers the 121°C to 199°C temperature range at two states of battery charge, corresponding to the higher and lower limit of the operating charge level. The second part of the research aims at investigating the electromechanical performance of new structural configurations, such as external bonding, and adding new loading conditions, such as combined curvature and strain, to the existing results previously obtained by (Pereira, 2008; Pereira, 2009). Differently from (Pereira, 2008) and (Pereira, 2009) the battery is co-bonded or secondary bonded to the composite without pre-encasing it in a protective vinyl ester case, but only with a localized application of silicon conformal coating at the battery leads to ensure electrical insulation and prevent shorting with carbon fibers.

## 2. METHODOLOGY

### 2.1 SOLID STATE, THIN FILM LI-ION BATTERY

All TFBs utilized in this research are manufactured by FrontEdge Technology under license from the Oak Ridge National Laboratory (ORNL), Figure D19. The same batteries have been utilized in (Pereira, 2006; Pereira, 2008(a); Pereira, 2008(b); Pereira, 2009). The cathode material is lithium cobalt oxide ( $\text{LiCoO}_2$ ), the anode is lithium metal (Li) and the solid state ceramic electrolyte is LiPON ( $\text{Li}_{2.9}\text{PO}_{3.3}\text{N}_{0.46}$ ) (Bates, 1992). This battery chemistry has been electrically characterized in (Bates, 2000). The active components are encased by two muscovite substrates bound by a thermoplastic layer of Surlyn sealant, leading to a total TFB thickness of 150  $\mu\text{m}$ , Figure.D20. Critical temperature thresholds for the TFB materials are summarized in Table D2.



Component	Material	Temperature	Property
Sealant	Surlyn	98°C	Melting point
Anode	Lithium	181°C	Melting point
Electrolyte	$\text{Li}_{2.9}\text{PO}_{3.3}\text{N}_{0.46}$ (LiPON)	300°C	Maximum operating temperature <sup>1)</sup>
Cathode	$\text{LiCO}_2$	700°C	Annealing temperature <sup>2)</sup>
Substrate	Muscovite	700°C	Calcination temperature
Current collector	Platinum	1768°C	Melting point
1) Yu X. et al. <i>J. Electrochem. Soc.</i> 147(2), 517 (2000)			
2) Bates J. B. et al. <i>J. Electrochem. Soc.</i> 147, 59 (2000)			

Table D2. Relevant temperature thresholds for TFB components

All the active components are grown by physical vapor deposition (PVD) performed in-situ over the muscovite substrate. The cathode is fabricated through RF magnetron sputtering and annealing at high temperature (typically 700°C) to obtain a crystalline microstructure with large grains and uniform preferred crystalline orientation to maximize ionic conductivity (Bates, 2000). The muscovite substrate ensures dimensional stability during the in-situ cathode annealing, avoiding cathode cracking or dis-bonding due to thermal stresses. The patented process is described in (Krasnov, 2011). The electrolyte is deposited by RF magnetron sputtering in  $\text{N}_2$  atmosphere (Krasnov, 2005) according to the ORNL process (Bates, 1992). The Li anode is deposited by thermal evaporation (Bates, 2000). These materials are highly reactive. Li-metal reacts with  $\text{N}_2$  (Bates, 1992) and  $\text{O}_2$  (Bates, 2000), while all the three active component materials, react with  $\text{H}_2\text{O}$  (West, 2002). Therefore TFB has to be hermetically sealed. The battery cell is a 25.4 mm by 25.4 mm square with nominal voltage of 4.2V, and a capacity of 1 mAh. In order to calculate the actual energy density, the energy delivered by one battery during a full discharge has been measured according to the method described hereinafter, and subsequently the active components of the same battery have been separated from the substrate and sealant and weighted with a Mettler Toledo XS64 analytical balance. The active mass, given by the sum of cathode, electrolyte, anode and current collectors, is 0.0113 g, which leads to an energy density of 353  $\text{Wh kg}^{-1}$ , while the energy density calculated with respect to the total mass is 22  $\text{Wh kg}^{-1}$ .

## 2.2 MANUFACTURING OF THE MULTIFUNCTIONAL COMPOSITE LAMINATE

Battery survivability is monitored through discharge and charge cycling prior to and post thermal processing test. The same survivability check is additionally conducted two months following the treatment. An automated circuit board featuring a charge-discharge electronic circuit, Figure D21, is connected to a National Instruments BNC-2120 connector and controlled via a LabView program.

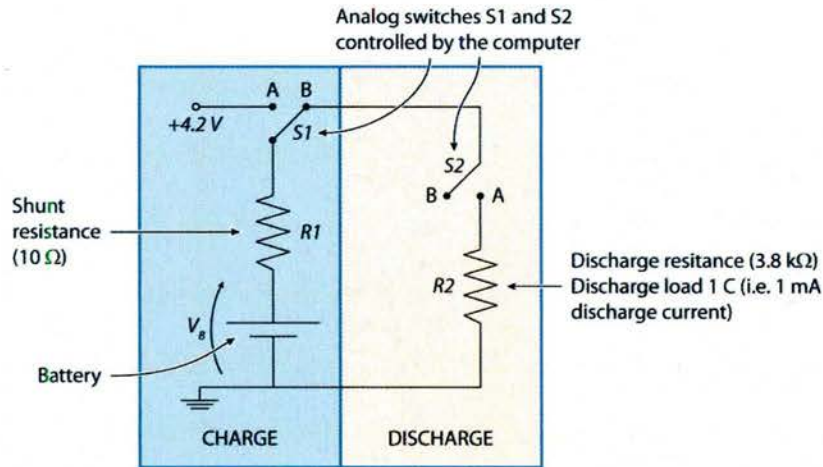


Figure D21. Schematic of the circuit used to test a battery's survivability by monitoring charge and discharge performance before and after processing

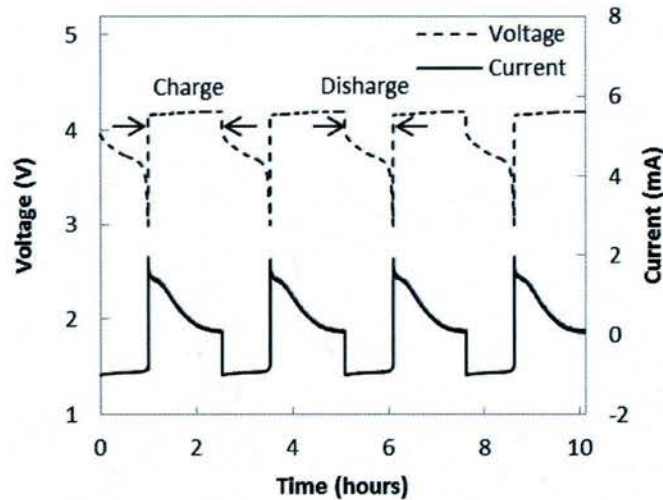


Figure D22. Description of the four discharge and charge cycles for the survivability test

Current and voltage readings are collected every three seconds. Discharging occurs under a constant load of  $3.8 \text{ k}\Omega$  which gives a discharge current of about  $1 \text{ mA}$ . The TFB is considered fully discharged when the voltage reaches  $3 \text{ V}$ . The current can be considered constant over the entire discharge process, as shown in Figure D22, leading to a discharge rate of  $1 \text{ C}$ . Immediately following a discharge, charging is performed at a constant voltage of  $4.2 \text{ V}$ , applied by a Hewlett-Packard 6632A System DC Power Supply. A shunt resistance of  $10 \text{ }\Omega$  is utilized to measure the current. The battery is considered fully charged when the current drops below  $50 \text{ }\mu\text{A}$ . For each battery, five charge-discharge cycles are performed; the first is used to condition the battery and the following four provide the average discharge capacity, Figure D22. The capacity is obtained by numerical integration of the discharge current, as a function of time, over a



discharge cycle. TFBs are subjected to pressure, temperature and liquid resin environment representative of composite curing cycles. Batteries are exposed to a one hour isothermal hold at 121°C, 149°C, 177°C and 199°C. At each temperature, one battery is tested at ambient pressure, a second is placed under a 26 mm Hg vacuum and a third is embedded in a 50.8×50.8×3.8 mm pool of Fiberlay Pro Glas 1300 series neat epoxy resin under a 26 mm Hg vacuum. The vacuum is established within a flexible nylon bag in order to apply a hydrostatic pressure to the resin, Figure D23.

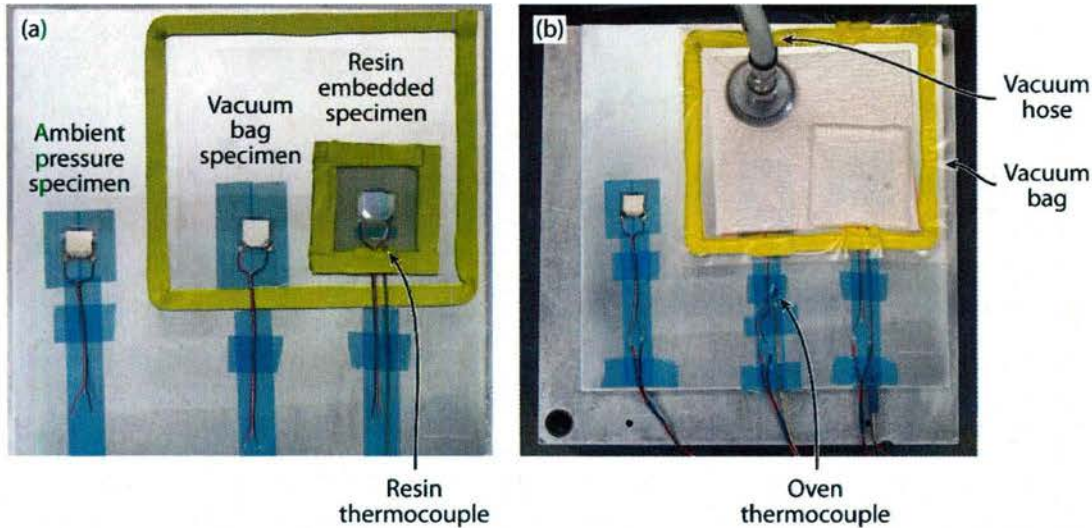


Figure D23. Simultaneous thermal treatment of batteries under ambient pressure, in a vacuum bag and embedded in a neat resin pool. (a) Location of batteries before addition of (b) the vacuum bag

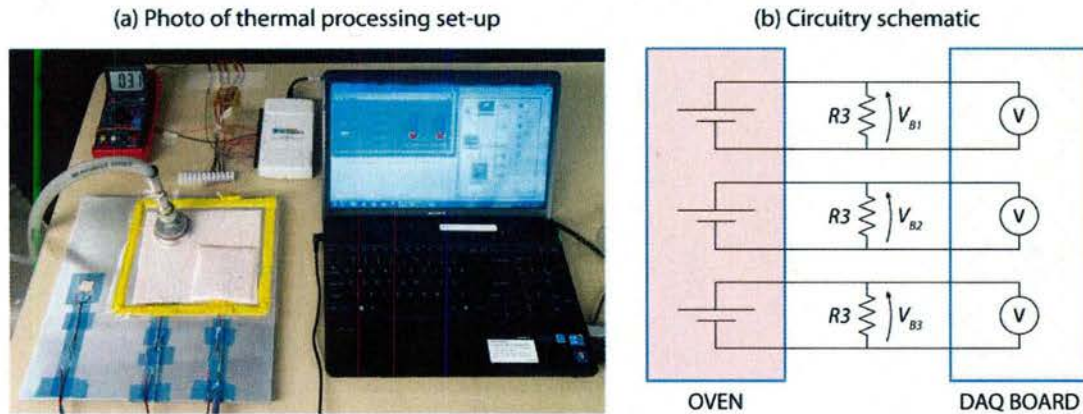


Figure D24. Voltage drop across the battery and thermocouple voltages are recorded by a LabView program via the DAQ board during thermal testing under electrical load. (a) Set-up before the specimens tray is placed into the oven. (b) Circuit schematic include TFB inside the oven and resistive load (R3) outside the oven

A series of batteries are first thermally processed at 121°C in a fully charged state and in a partially charged state to determine if the state of charge affects battery survivability. In order to

avoid overdischarge, as recommended by FrontEdge, the partial state of charge is reached by discharging to 3.9 V<sub>OC</sub> (open circuit voltage) prior to thermal processing. Based on the results of the 121°C, only partially charged TFBs are tested at higher temperature. The temperature is recorded by a LabView program, which monitors the oven temperature and the resin temperature from two independent thermocouples via a National Instrument USB-6210 multifunctional data acquisition (DAQ) module. A Despatch LAC bench-top ventilation oven heats the specimens at a rate of 5°C min<sup>-1</sup> from room temperature to the test temperature. Moreover the test is conducted under an electrical load of 108 kΩ (R3) for better TFB failure detection. The current is small enough to consider the state of charge constant throughout the test. Voltages and currents are recorded by the DAQ and LabView program with a frequency of one measurement every 3 seconds, Figure D24. In total 18 batteries have been subjected to the thermal processing test. Based on the aforementioned tests results a cure cycle is designed and validated through TFB embedding tests in glass fiber/epoxy (GFRP) and carbon fiber/epoxy (CFRP) composite laminates. The TFB is embedded at the midplane of the laminate. Two slits in the top layers of the laminates allow for the Flat Flexible Cables (FFC), Nicomatic 254PW01E6095 polyester coated single copper conductor, to exit the laminate, Figure D25. FCCs are 0.25 mm thick and 5.12 mm wide, and they are rated for operation up to 150°C for short durations and to 100°C for continuous use.

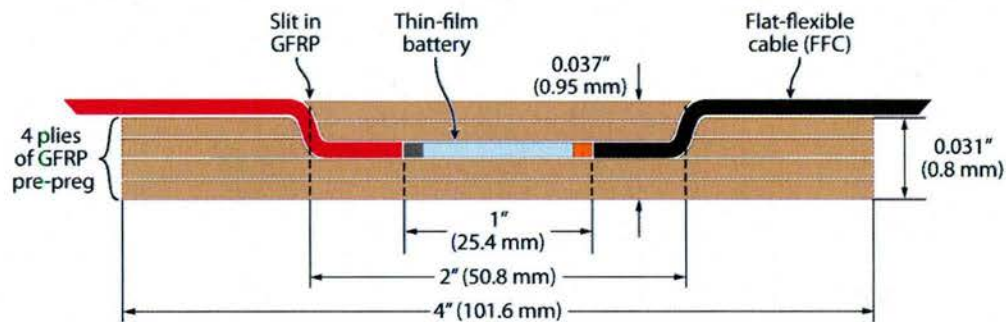
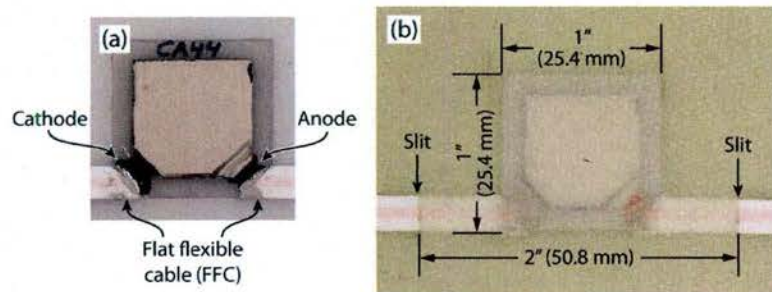


Figure D25. Cross-sectional schematic of a thin-film battery embedded at the mid-plane of a four ply GFRP laminate. Two slits in the top two layers allow for the FFC to exit the panel





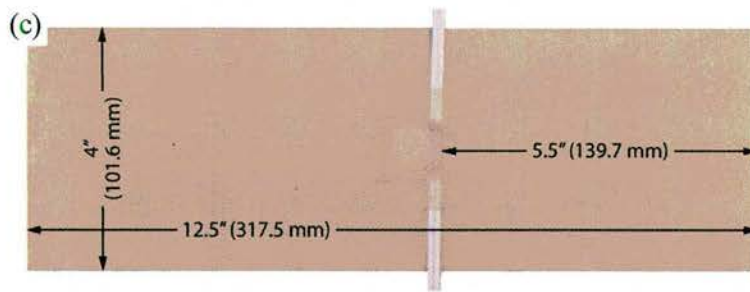


Figure D26. Photos of a battery (a) before and (b) after embedding within a GFRP laminate. (c) Panel with the embedded battery

They are connected to the TFB electrodes using MG Chemicals silver conductive epoxy 8331-14G. Toray AGATE prepreg glass fiber FGF7781/2510, 8 Harness Satin Weave Fabric is used for the embedding test. The 4-ply laminate is cured at 132°C and 520 kPa for two hours through heated press molding. The laminate stacking sequence is  $[0,90]_4$ . The battery is located at the panel mid-span, Figure D26. A second embedding test is performed using the Toray AGATE prepreg carbon fiber tape T700/2510 with stacking sequence  $[0/90]_{2s}$ , Figure D27. The aforementioned fabrication process is adopted with the addition of a localized application of MG Chemicals silicone conformal coating 422-55 at battery exposed leads to insulate the connections. Attempts of embedding the TFB without insulated connections have failed due to electrical shorting with the CFRP.

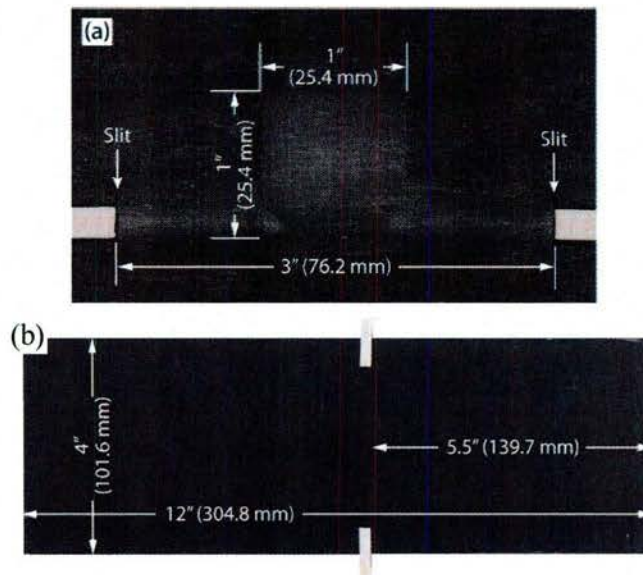


Figure D27. Photos of a battery embedded in a CFRP laminate showing (a) a close-up of the battery and (b) the whole panel.

## 2.3 ELECTROMECHANICAL CHARACTERIZATION

A list of the tests performed is shown in Table D3. All the specimens are manufactured by press molding of IM7/977-3 prepreg material. Based on the results obtained in the thermal processing tests, a 2 hours curing cycle at 132°C and 85 psi has been adopted. For the externally bonded TFB configuration the structural adhesive film 3M AF163-2 has been cured for 1.5 hours at 121°C in the vacuum bag. The double cantilever beam test (DCB) is conducted according to the ASTM D5528 standard. Specimens are 25.4 mm wide, which is equal to the TFB width. Three specimens have been tested to determine the mode I fracture toughness of the plane laminate. Other three specimens with a TFB embedded at the laminate mid-plane are then tested. The crack is started at the mid-plane of the loaded end of the specimen, as in a standard DCB test, and propagated towards the TFB, which is located at specimen mid-span.

Test	Description
Double cantilever beam (DCB) (ASTM D5528)	Measure mode I interlaminar fracture toughness (GIC) of laminates with and without embedded TFB (3 repetitions)
Uniaxial tension with full field strain monitoring (modified ASTM D3039)	Digital Image Correlation (DIC) monitoring of laminate strain to detect strain concentration produced by embedded and externally bonded TFB with different laminate lay-ups. (7 laminate stacking sequences tested; 2 repetitions).
TFB full field thickness monitoring during charge/discharge cycling	Test conducted on TFB alone to characterize battery thickness vs. charge level. (2 repetitions)
Uniaxial tension with TFB capacity monitoring	Monitor capacity of embedded battery during and following tension test to identify strain at electric failure and failure modes. (2 repetitions)
Four point bend with TFB capacity monitoring	Monitor capacity of embedded or externally bonded TFB during and following 4PB flexure test to define strain and curvature at electric failure as well as failure modes. (4 configurations; 2 repetitions)

Table D3. Summary of mechanical testing activity

The goal of the test is to determine the fracture toughness of the multifunctional laminate and the crack propagation path when crossing the TFB. In order to characterize the stress/strain field for different laminate configurations, uniaxial tension testing with full field strain monitoring have been performed. A Digital Image Correlation (DIC) technique has been adopted to monitor the surface strain on the specimen. The load is applied up to failure in order to assess the mechanical strength, whereas the electrical failure is not considered. The procedure is compliant to ASTM D3039, except for a specimen width of 76.2 mm to minimize the interaction between the edge effect and the stress concentration caused by the TFB. Seven laminate layups have been tested, which include externally bonded battery, interlaminar embedding, Figure D28, and cut out embedding, which consists in locating the battery inside a cutout in the mid-plane ply.



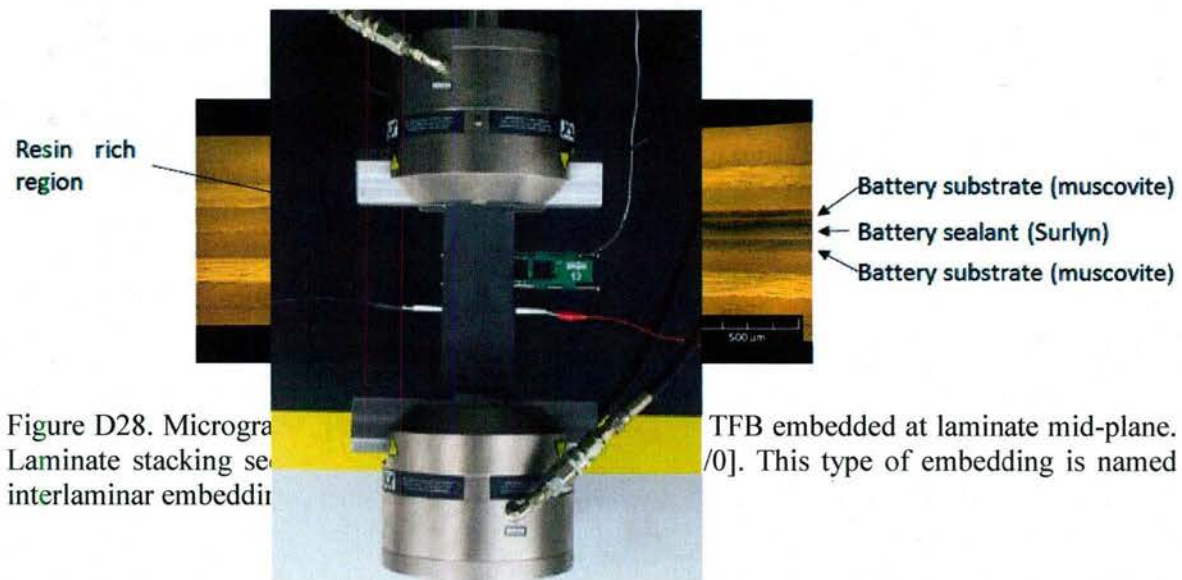


Figure D29. Uniaxial tension test setup of a composite specimen with embedded TFB and capacity monitoring. The strain applied with a test frame (only hydraulic grips shown) is measured with an extensometer.

Two repetitions per configuration have been tested. The DIC has been also employed for monitoring the thickness increase of a TFB alone during a single, full discharge and followed by a full charge cycle. The Li-ion insertion is expected to cause anode volume increase during charge. Therefore the difference in thickness between the fully discharged and the fully charged battery status has to be assessed carefully in order to avoid excessive interlaminar normal stress inside the laminate and inside the battery packaging layers. Finally uniaxial tension and four point bending tests with TFB capacity monitoring are conducted to assess the electric integrity. Two tension test specimens are tested with an interlaminar embedding in order to apply a uniform strain to the battery. The specimens are 304.8 mm long and 76.2 mm wide. The battery is connected to the charge/discharge circuit by means of FFCs, Figure D29. The four point bend

tests are conducted for applying curvature or combined curvature and in-plane strain. This is achieved by interlaminar embedding and external secondary bonding respectively: while the first leads to pure curvature, the second leads to curvature plus compressive or tensile strain depending on which side of the specimen the TFB is bonded on. For the four point bending test a plane laminate is also tested. The mechanical properties of the TFB packaging materials and the CFRP are listed in Table D4.

Material	Density	Modulus of elasticity	In-plane modulus of elasticity	shear of	Mode I fracture toughness	Strain to failure
Surlyn	0.96 g/cm <sup>3</sup>	282 Mpa	106 MPa		1250 J/m <sup>2</sup> <sup>1)</sup>	80000 µstrain
Muscovite	2.60 g/cm <sup>3</sup>	176 GPa	64.3 GPa		891 mJ/m <sup>2</sup> <sup>2)</sup>	unknown
IM7/977-3	1.63 g/cm <sup>3</sup>	90° - 8.34 GPa 0° - 162 GPa	4.96 GPa		316 J/m <sup>2</sup>	90° - 7700 µstrain 0° - 14600 µstrain

1) Compston P. et al., J Mater Sci Lett, 21, 383-386 (2002)

2) Giese Jun R.F., Nature, 248, 580-581 (1974)

Table D4. Mechanical properties of TFB packaging components and prepreg composite material

### 3. RESULTS

#### 3.1 LIMITS OF PROCESSABILITY

Typical temperature and voltage profiles for the thermal processing test are shown in Figure D30. During ramp-up the resin temperature shows a spike due to the exothermic reaction associated to the resin crosslinking. However the maximum difference between the resin and the oven temperature during ramp-up never exceeds 15°C. Moreover the temperature peak at crosslinking always occurs during temperature ramp-up and it never exceeds the isothermal hold temperature, which is therefore the maximum temperature experienced by the TFB. The battery voltage decreases with increasing temperature and it recovers its initial level when the batteries are removed from the oven at the end of the one hour long isothermal phase. The voltage of the battery embedded in neat resin, however, shows a negative spike which corresponds with the beginning of the exothermic event. The spike exists for all TFBs processed in the neat resin, lasting 3 to 9 seconds, without having a detrimental effect on survivability. While the reason for the voltage drop is unknown, electric conductivity in epoxy resins, which could cause electronic flow between the battery exposed leads, is known to be caused by impurities, with Na<sup>+</sup> and Cl<sup>-</sup> ions normally being the charge carriers (Gallone, 2001).



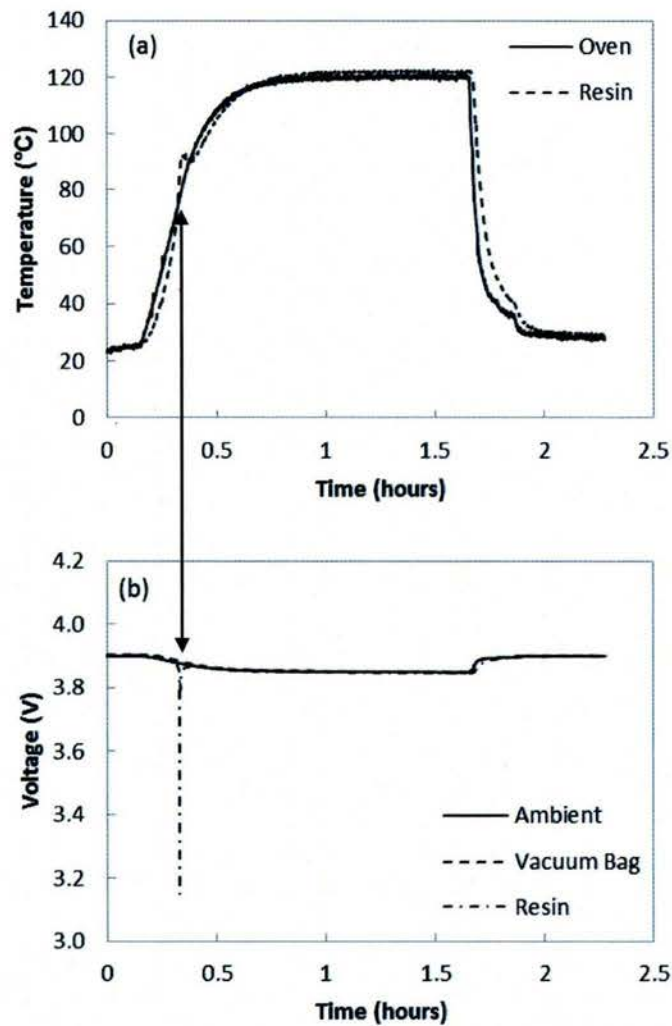


Figure D30. (a) Typical temperature cycle for TFB thermal processing test. The temperature profile for the oven and neat resin is shown for a 1 hour isotherm at 121°C. (b) Voltages of the three batteries shown in Figure D23 undertaking the thermal treatment recorded in (a). A voltage drop of the battery embedded within the resin coincides with heat generation by the resin due to exothermal crosslinking reaction

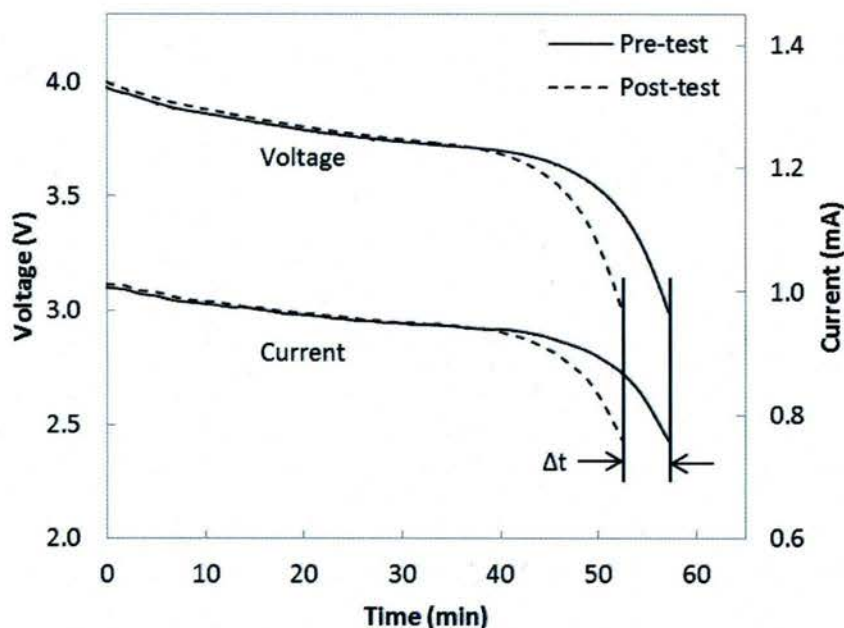


Figure D31. A discharge profile from the survivability test for a fully charged battery subjected to a 1 hour isotherm at 121°C under ambient pressure. The decrease in the discharging time is proportional to the 6% decrease in capacity retention after processing (see Table D3)

The voltage drop does not occur with the embedding in the Toray 2510 resin system. Thermal testing at 121°C of fully charged batteries always leads to battery capacity reduction, as summarized in Table D5, leading to an average capacity reduction of 9%. A reduction in discharge time, proportional to the capacity reduction, is noted, while the cell voltage and power are unchanged, Figure D31.

	Fully Charged		Partially Charged	
	Capacity Retention	Survival Rate	Capacity Retention	Survival Rate
Ambient	94%	1/1	102%	1/1
Vacuum Bag	95%	1/1	102%	1/1
Neat Resin	84%	1/1	102%	1/1

Table D5. Capacity retention of batteries undergoing a 1 hour isothermal hold at 121°C in either a fully charged state or partially charged to 3.9 V<sub>OC</sub> (open circuit voltage)

When TFBs are partially discharged to 3.9 V before being tested, they withstand thermal processing up to 149°C without any detrimental effect on their electric performance. The detailed summary of the results, shown in Table D6 and D7, shows that the short term and long term capacity after thermal processing oscillates within  $\pm 3\%$  with respect to the baseline capacity measured before the test. The capacity variation is associated to a slight offset of the discharge current and voltage curves, Figure D32. Either the liquid resin or the vacuum bag environment does not seem to have an effect at this processing temperature.



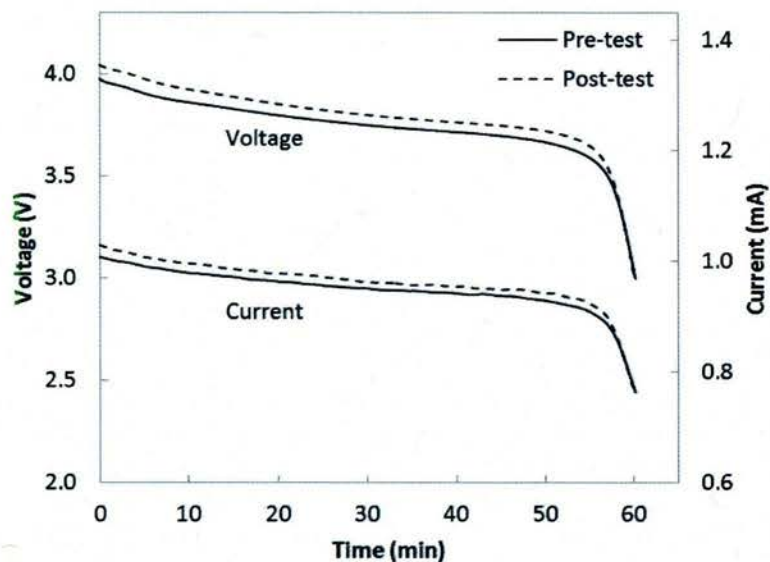


Figure D32. A discharge profile from the survivability test for a partially charged battery subjected to a 1 hour isotherm at 121°C under ambient pressure. The battery had 102% capacity retention after processing (see Table D3)

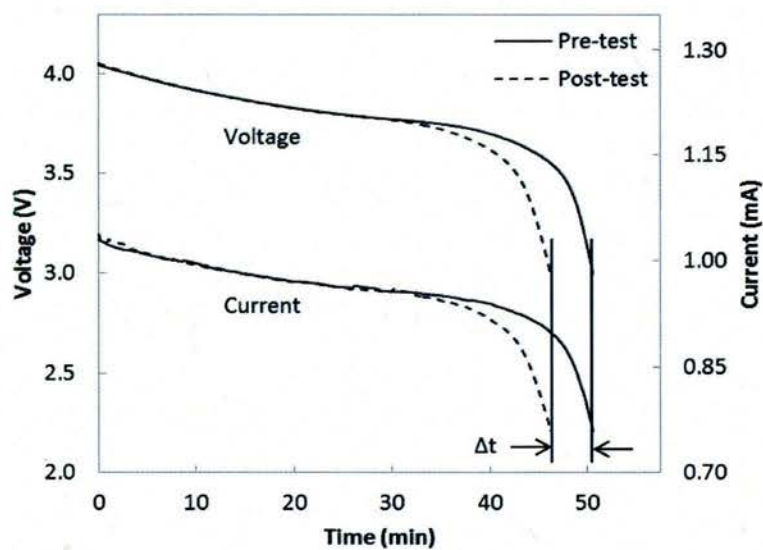


Figure D33. A discharge profile for a partially charged battery subjected to a 1 hour isotherm at 177°C under vacuum. The battery had 91% capacity retention after processing, ultimately failing with aging (see Table D4)

	Isothermal Temperature			
	121°C	149°C	177°C	199°C
Ambient	1/1	1/1	1/2	0/1
Vacuum				
bag	1/1	1/1	(2)/2	0/1
Neat Resin	1/1	1/1	0/2	0/1

Table D6. Survival rate of partially charged batteries subjected to temperatures, pressures and liquid resin environment typical of composite manufacturing. Parentheses indicate failure after two months of aging

	Isothermal Temperature			
	121°C	149°C	177°C	199°C
Ambient	102%	100%		
Vacuum	(100%)	(100%)	76% (70%)	0%
bag	102%	103%		
	(100%)	(100%)	87% (0%)	0%
Neat Resin	102%			
	(100%)	98% (98%)	0%	0%

Table D7. Average discharge capacity retention of survived batteries from Table D4. Values in parenthesis measured two months after test

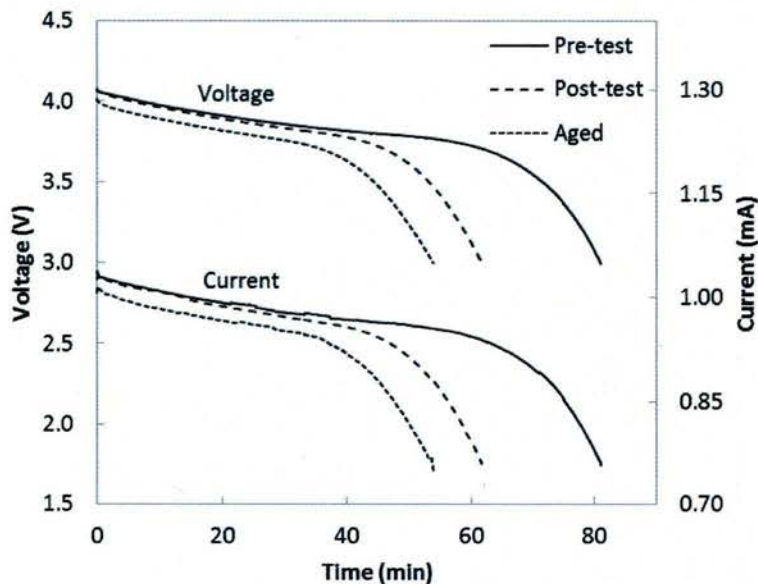


Figure D34. A discharge profile from the survivability test for a partially charged battery subjected to a 1 hour isotherm at 177°C under ambient pressure. The battery had 76% capacity retention after processing, reducing to 70% with two months of aging



All the batteries tested at 177°C, either at ambient pressure or in the vacuum bag, are affected by partial or total capacity loss, Table D6 and D7, associated to a decreased discharge time and a negative translation of the current and voltage discharge profile, Figure D33 and D34. The batteries embedded in neat resin at 177°C, as well as all the ones processed at 199°C failed during testing. Three distinct types of failures have been recognized and characterized based on optical microscopy at anode side and capacity retention, Figure D35(a-d). Type I failure, Figure D35(b,bb), is observed as a localized grey spot on the Li-anode with complete loss of grain boundaries. FrontEdge attributes these observations as electronic failures consisting of local breakdown of the electrolyte. The grey spot is always associated to bubbling of the overlaying Surlyn sealant layer at failure location. This failure occurs in batteries processed at ambient pressure or within the vacuum bag. The affected batteries are operational but with a reduced capacity. Type II failure produces a neutral grey discoloration, which contacts at least one edge of the active component, Figure D35(c,cc). The micrographs reveal dark patches intermixing with the pristine anode. It is believed that this failure is caused by the reaction of the Li-anode with contaminants diffusing through the Surlyn sealant and entering into the battery. The appearance of Type II failure is always associated to total battery failure. This failure is observed after thermal processing of batteries embedded in neat resin, or in aged batteries previously processed at 177°C. The Type III failure shown in Figure D35(d,dd) has occurred for all the batteries tested at 199°C.

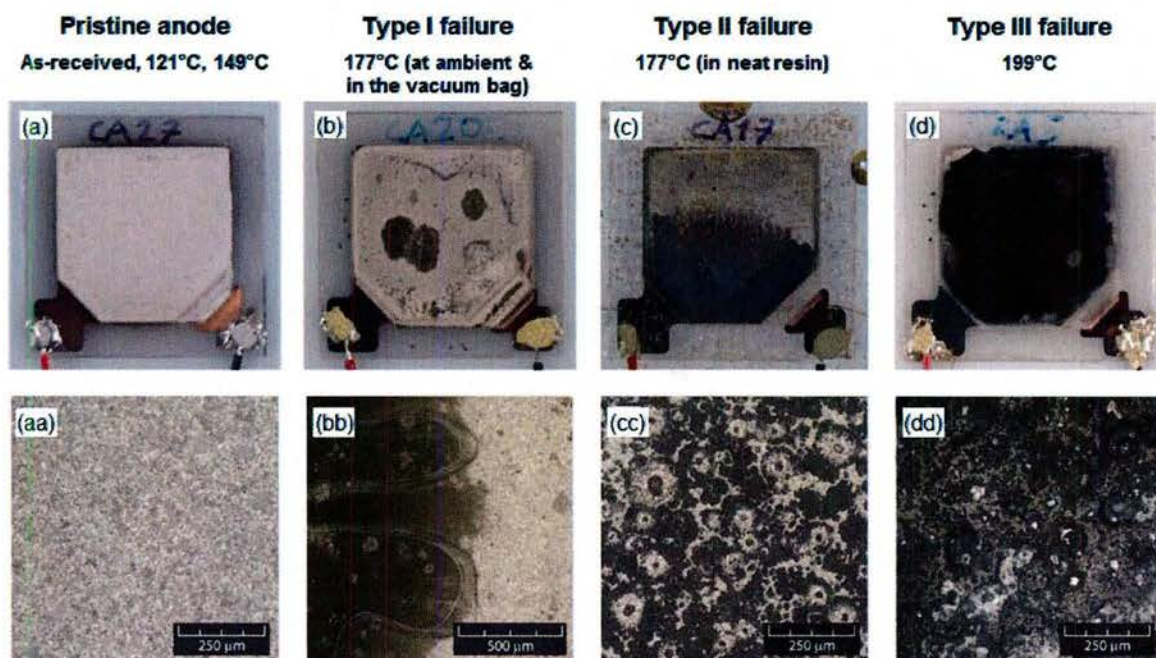


Figure D35. Anode side photos of the three observed types of failures ((b), (c) and (d)) compared to an as-received battery (a). Corresponding dark-field optical micrographs are shown in (aa) through (dd). Type I failure is associated with a local breakdown of the electrolyte and bubbling of the sealant (Surlyn M.P. of 98°C). Reaction of the anode with contaminants results in a Type II failure. Type III failure occurs above the Li melting temperature (181°C). Type I leads to partial capacity loss; Type II and III lead to total capacity loss.

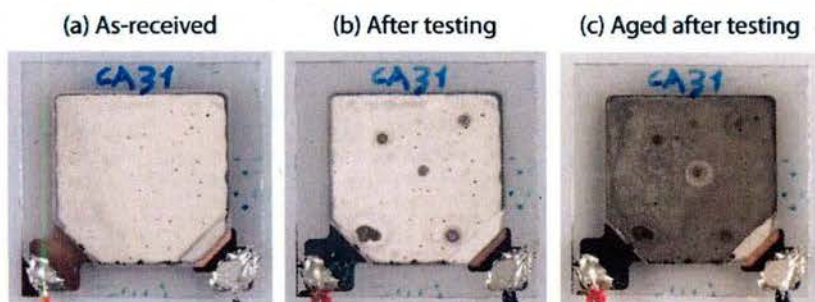


Figure D36. A battery thermally tested at 177°C in the vacuum bag for an hour showing (b) the formation of Type I failures immediately after testing, followed by (c) Type II formations with two months of aging. Immediately after testing, the cell exhibited 87% capacity retention, however, completely failed with aging

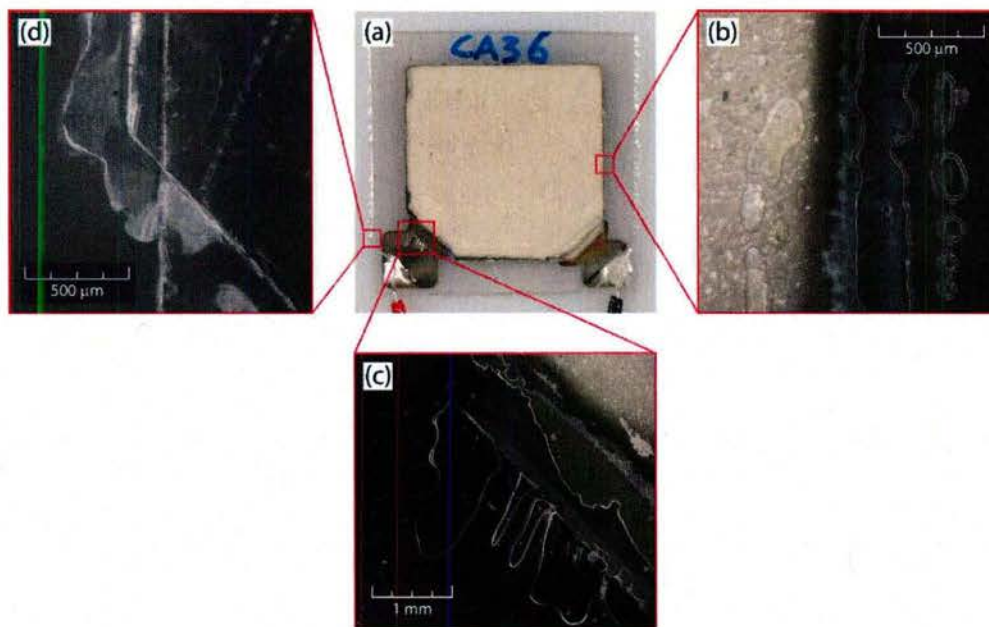


Figure D37. The appearance of bubbles and a disbonded front (b) along the edge the active components and (c) over the leads after 121°C processing. In some as-received batteries, bubbles are apparent along the edge of the active components. (d) shows the Surlyn which has been squeezed out of between the muscovite layers (exhibiting a slight offset); this is typical of the vacuum bagged specimens.

The failure occurs above 177°C during temperature ramp-up, leading to sudden loss of voltage and battery failure. The failure is due to lithium melting (M.P. 181°C). The TFB becomes black at the anode side, occasionally showing gray spots which are probably Type I failures formed before the anode melting. The battery shown in Figure D36 is affected by Type I failure and associated capacity reduction immediately after processing at 177°C in the vacuum bag, but



completely fails by Type II failure with aging. This indicates that the failure Type II is time-dependent. Additionally, a similar result is observed when the battery seal is artificially compromised in the ambient. Hence the low temperature thermoplastic sealant (M.P. 98°C) seems to be the limiting factor for survivability from a processing standpoint. Further observation of treated batteries reveals sealant bubbling and flowing even for TFBs tested at 121°C, leading to the formation of a disbonded front along the edges of the active components (Figure D37(b)) and over the leads (Figure D36(c)). For the TFBs processed under vacuum bag the Surlyn is seen to have been squeezed out of the battery edges (Figure D37(d)). However the functionality of these batteries, as tested for survivability after testing and after two months aging, is not affected. Inspection of as-received batteries revealed that some batteries have long strands of bubbles along the edges of the active components. Heating of the battery leads to melting of the Surlyn allowing for mass and void diffusion. However, no correlation has been found between the appearance or location of bubbles and battery survivability. Finally successful embedding tests with full capacity retention are performed by co-curing the TFB within a composite laminate through press molding of prepreg materials at 132°C and 517 kPa, with a cure time of 2 hours, Figure D27-29, Table D8.

	Capacity Retention	Survival Rate
CFRP	103%	1/1
GFRP	102%	1/1

Table D8. Survival of partially discharged batteries embedded in either a GFRP or CFRP laminate cured at 132°C and 520 kPa

### 3.1 ELECTROMECHANICAL PERFORMANCE

When the delamination that propagates through the CFRP laminate reaches the battery it propagates with an unstable fashion throughout the battery, Figure D38. Further data reduction of the DCB test show that the average fracture toughness of the laminate, calculated over the net crack surface, defined as the CFRP surface only, is equal to the average fracture toughness of the plane laminate. Therefore the TFB behaves as a perfect defect, similarly to a Teflon insert. As expected from the very low fracture toughness of the muscovite, Table D4, the crack propagates through the muscovite substrate, Figure D39. The uniaxial test under DIC monitoring shows that the interlaminar embedding does not lead to surface strain concentrations, Figure D40. Moreover the strain distribution is reasonably well predicted by the Classical Laminate Theory (CLT), Figure D40 and Table D9. The good agreement between the experimental and calculated strain seems to confirm that the TFB shares load with the laminate as desired.

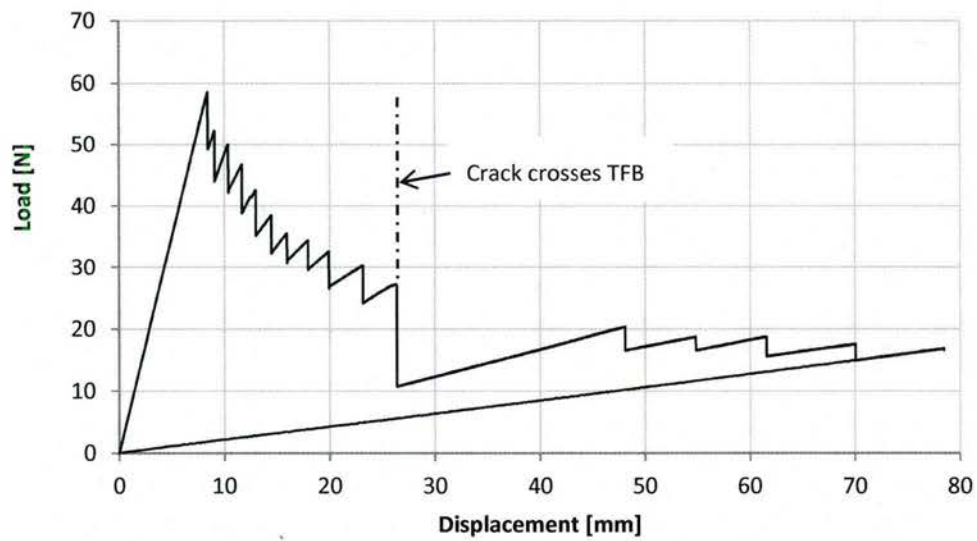


Figure D38. Typical DCB load displacement curves for a laminate with embedded TFB at the mid-plane

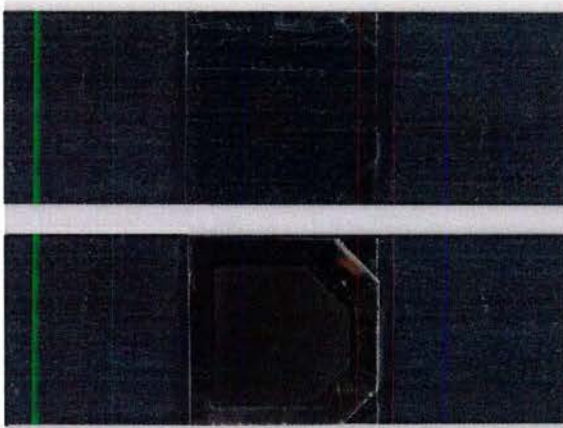


Figure D39. Crack surfaces of DCB specimen with embedded TFB showing the muscovite substrate left on both sides.



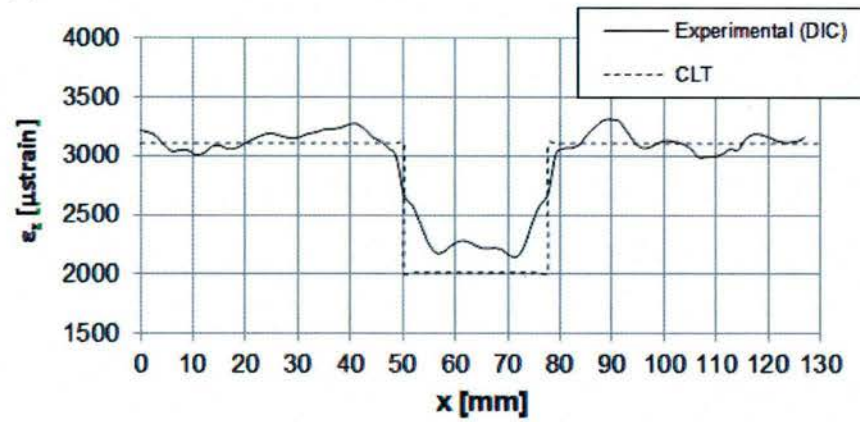
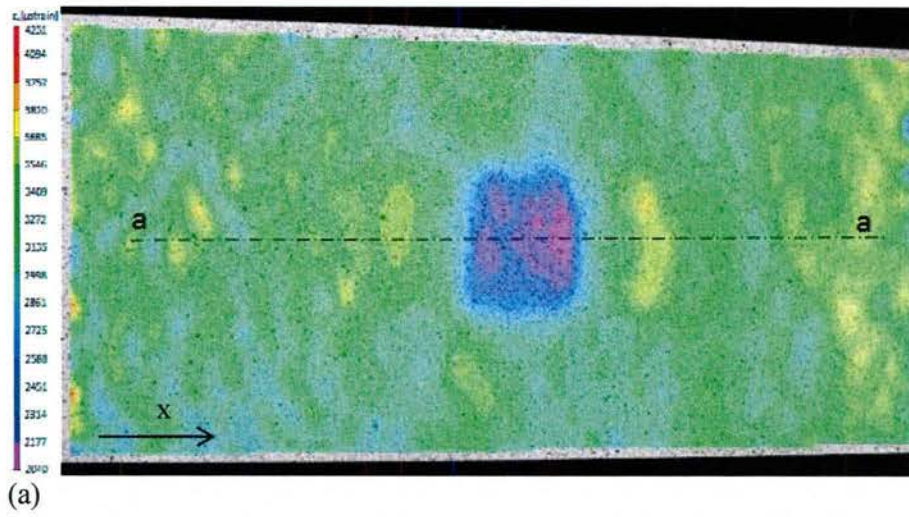


Figure D40. Uniaxial tension test of laminate with interlaminar embedding at laminate mid-plane; Laminate stacking sequence is [0/90/TFB/90/0]. (a) Surface strain field  $\varepsilon_x$  measured with Digital Image Correlation (DIC). (b) Comparison between measured strain at section a-a and calculated strain with Classical Laminate Theory (CLT)

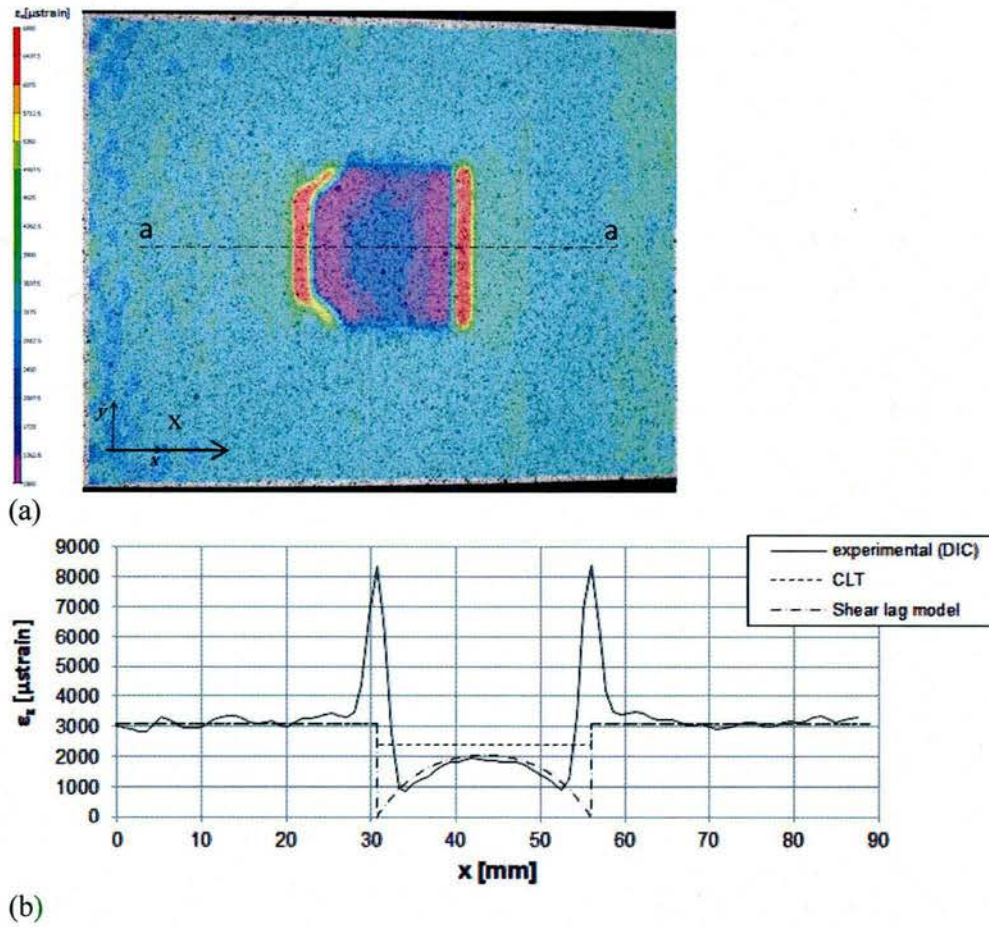


Figure D41. Uniaxial tension test of laminate with externally bonded TFB. Laminate stacking sequence is [TFB/(0/45/90/-45)S]. (a) Surface strain field  $\varepsilon_x$  measured with Digital Image Correlation (DIC). (b) Comparison between measured strain at section a-a and calculated strain with Classical Laminate Theory (CLT) and shear lag theory

Lay-up	$\bar{\varepsilon}_{TFB}/\bar{\varepsilon}_0$	
	Experimental (DIC)	CLT
[0/90/TFB/90/0]	0.75	0.65
[0 <sub>2</sub> /TFB/0 <sub>2</sub> ]	0.89	0.79
[0/45/90/-45/TFB/-45/90/45/0]	0.80	0.74

$\bar{\varepsilon}_{TFB}$ : average strain over TFB  
 $\bar{\varepsilon}_0$ : average far field strain

Table D9 . Uniaxial tension testing with interlaminar embedding. Comparison between measured and calculated strain with classical laminate theory (CLT)



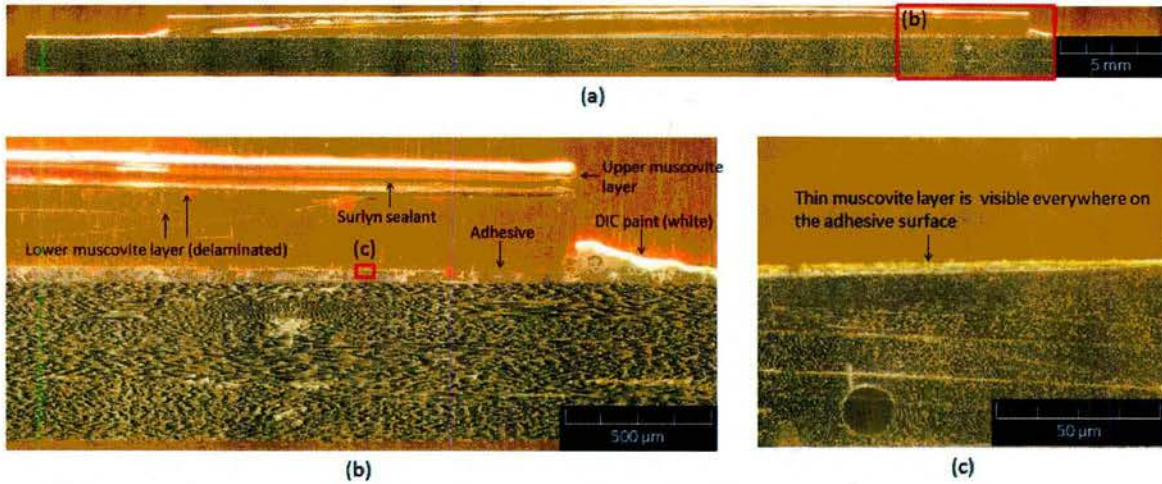


Figure D42. Micrographs showing delamination failure of the TFB substrate under uniaxial tension. (a) Full specimen section with TFB lifted apart from the laminate throughout the entire battery length. (b) Multiple delaminations propagated through the lower substrate. (c) A thin muscovite layer left over the adhesive film throughout the whole crack surface.

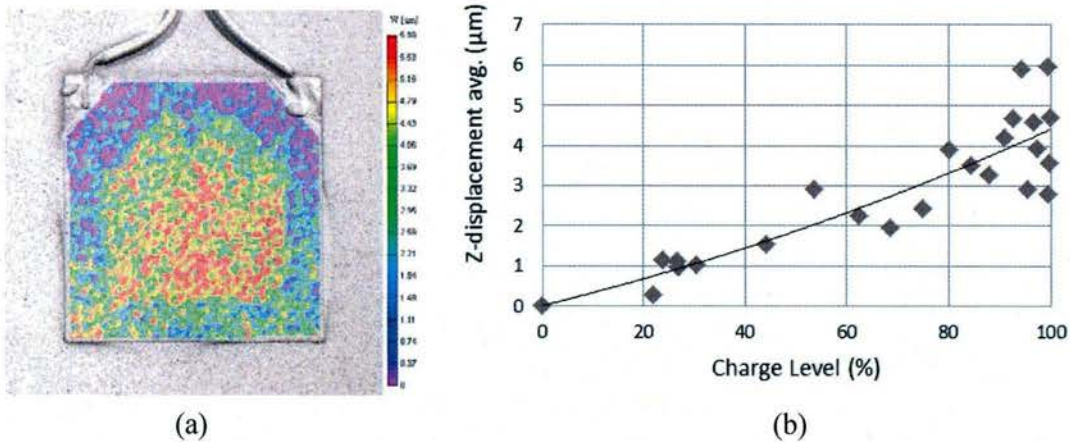


Figure D43. (a) DIC contour plot of z-displacement at battery full charge level. (b) Average z-displacement at the anode surface, measured at increasing charge levels.

The slightly higher values of measured strain, with respect to the calculated ones, might be due to the higher stiffness of the center section of the specimen compared to the side section. This local increase of stiffness caused by the TFB, concentrates the stress towards the center of the specimen and decreases the average stress along the edges. Another reason could be the uncertainty in the muscovite modulus of elasticity utilized as input for the CLT calculation. The strain distribution relevant to the cutout embedding is affected by strain concentrations. The strain increase ranges from the 16% of the unidirectional laminate to the 38% of the crossply laminate. The concentrations are along the transverse TFB edges. The reason of the strain

concentrations seems to be the stiffness mismatch between the TFB and the cutout ply. Hence the cutout embedding is not recommended. The externally bonded TFB shows a non-uniform strain distribution because the TFB is in a shear lug condition. In fact the battery length is not enough to allow for the stress/strain field to stabilize and recover a plane stress condition, Figure D41. This is also due to the low shear modulus of elasticity of the Surllyn sealant. The two strain spikes located at the battery edges are apparent strain caused by the relative displacement between the upper and lower TFB substrate. From the strength point of view the TFB does not have detrimental effects on the laminate strength, but mechanical failure occurs at the battery substrate when the applied strain reaches 4898  $\mu\text{strain}$ , Table D10. The failure mode is muscovite delamination, which is due to shearing at the battery edges and low fracture toughness. The micrograph of the crack surfaces demonstrates that the muscovite adherent failure occurs across the entire crack surface, while the adhesion at the adhesive/muscovite interface remains intact, Figure D42. The TFB thickness increase during a full charge has been measured using the DIC. As shown in Figure D43, although the measurement is affected by a fairly high noise level, the trend has been clearly captured. The total increase is about 4  $\mu\text{m}$ , which is equal to the 40% of the total thickness of the active components. Therefore this expansion has to be considered as a design load case for the next generation of structural batteries. The mechanical tests conducted with TFB capacity monitoring demonstrate that the applied strain and curvature does not affect battery operation.

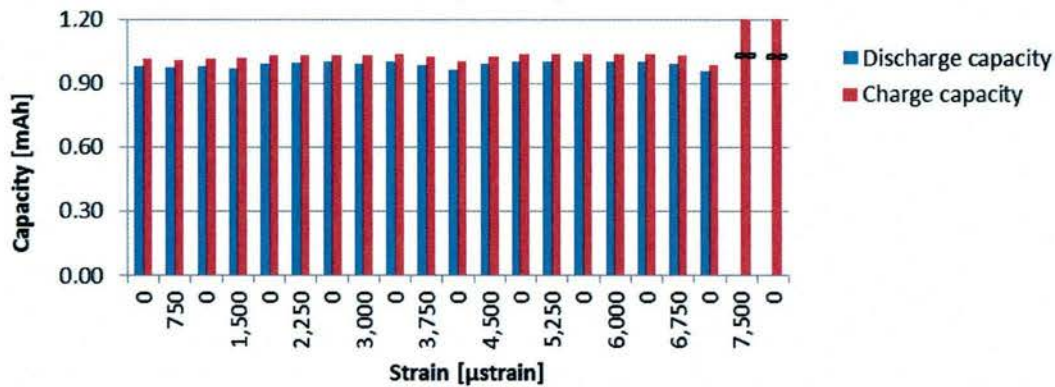


Figure D44. TFB capacity measured under increasing applied strain cycles up to electric failure.



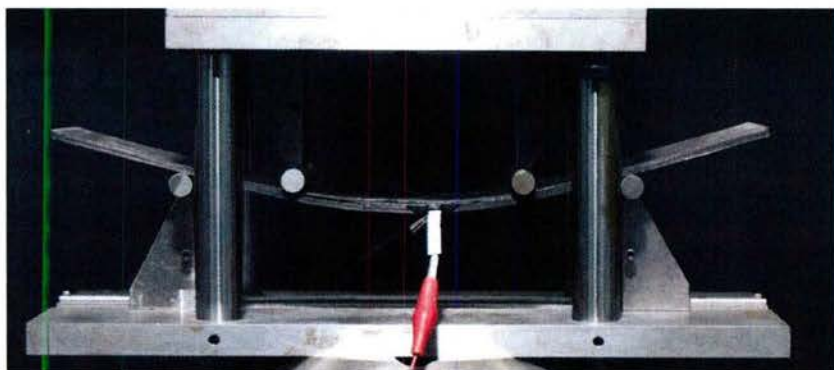


Figure D45. Four point bend test with standard 60:1 span/thickness ratio at incipient laminate failure. Stacking sequence  $[(0/45/90/-45)_3/\text{TFB}]_S$

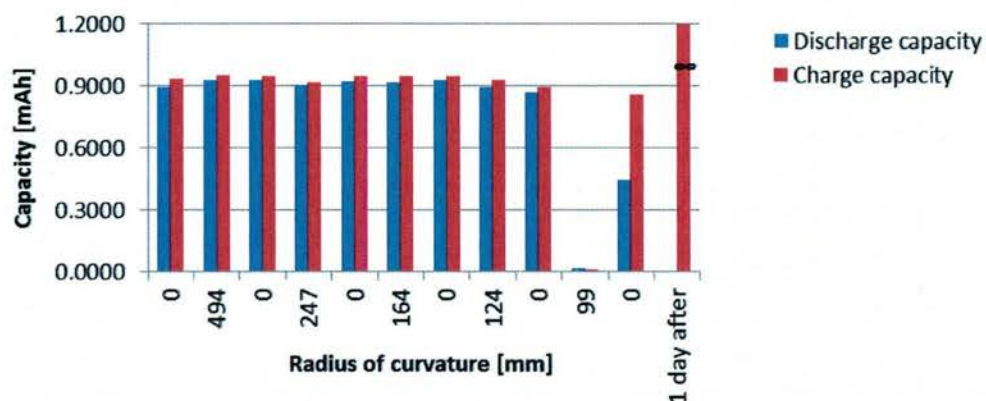
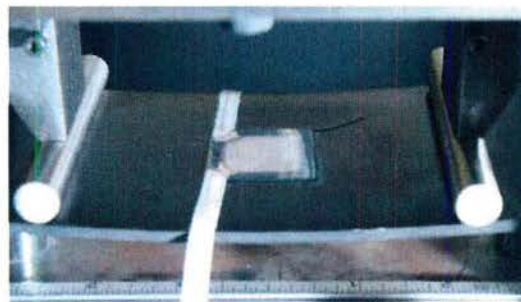
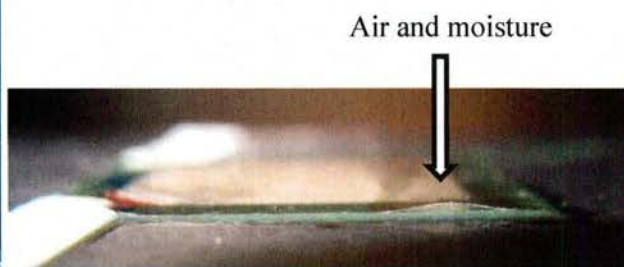


Figure D46. TFB capacity measured under cycles of increasing curvature up to electric failure



(a)



(b)

Figure D47. (a) Four point bend test with standard 60:1 span/thickness ratio at TFB failure. Stacking sequence  $[\text{TFB}/(0/45/90/-45)3S]$ . The battery is externally bonded onto the specimen surface that faces compression. (b) Failure occurs by disbonding buckling of the upper TFB substrate and subsequent battery contamination.

	Strain
Rep. 1	5072 $\mu$ strain
Rep. 2	4724 $\mu$ strain
Avg.	4898 $\mu$ strain

Table D10 . Uniaxial tension test with externally bonded TFB; strain values at TFB mechanical failure

	Strain
Rep. 1	6000 $\mu$ strain
Rep. 2	6750 $\mu$ strain
Avg.	6375 $\mu$ strain

Table D11. Uniaxial tension test with TFB capacity monitoring; strain values at electric failure

	Radius of curvature	of strain
Rep. 1	124 mm	0 $\mu$ strain
Rep. 2	99 mm	0 $\mu$ strain
Avg.	112 mm	0 $\mu$ strain
Rep. 1	504 mm	-2091 $\mu$ strain
Rep. 2	557 mm	-1890 $\mu$ strain
Avg.	531 mm	-1990 $\mu$ strain
Rep. 1	204 mm	5160 $\mu$ strain
Rep. 2	224 mm	4688 $\mu$ strain
Avg.	214 mm	4924 $\mu$ strain

Table D12 . Four point bend test with TFB capacity monitoring; TFB curvature and strain values at electric failure

When the uniaxial strain is applied the battery capacity remains constant, Figure D44, up to failure, which occurs on average at 6375  $\mu$ strain. The causes of the failure are unknown since the battery, being embedded in the specimen, is not accessible. However the strain at electric failure is only slightly higher than the strain at mechanical failure of the muscovite reported above, which can be an indication that in this case a mechanical failure of the packaging has caused TFB contamination. Curvature without strain is applied through a four point bending of a specimen with the TFB embedded at the laminate mid-plane. This is the only loading case where the laminate mechanical failure, which occurs at a radius of curvature of 159 mm, Figure D45, is more critical than the electrical failure which occurs at 112 mm, Table D12. The laminate critical radius of curvature is relevant to a quasi-isotropic laminate tested at a span to thickness ration of 60:1. In order to achieve the critical radius of curvature for the TFB the ratio has been increased to a non-standard 145:1. In the other cases of combined curvature and in-plane strain, electrical failure has been obtained with a 60:1 ratio and the results are shown in Table D12. As is can be see by the very low absolute value of the critical strain, the compressive case is particularly critical because it leads to early failure by TFB substrate disbonding buckling and subsequent battery contamination failure, Figure D47. This is due to the low modulus and large thickness of



the sealant, and furthermore it is possibly related to the sealant bubbling and disbonding that occurs during curing, as documented in Figure D37.

#### 4. CONCLUSIONS

This study identified the limits of processing-ability of solid state thin film lithium batteries embedded into composite laminates. Cure temperature is the most influential parameter for battery survivability during composites manufacturing. Successful embedding tests, with full capacity retention, have been performed with glass fiber/epoxy and carbon fiber/epoxy cured at 132°C and 517 kPa. With proper procedures it is possible to successfully cure the battery inside the laminate up to 149°C. If higher processing temperatures are reached, either locally, due to resin exothermic reaction, or by design, the battery's electrical performance will deteriorate. Failures are associated either to the TFB polymeric sealant failure, or to physical-chemical degradation of the electrolyte or the Li-anode. Ongoing research is focused on the mechanical and electrical characterization of laminates with embedded batteries under applied strain and curvature. The substrate (muscovite) brittleness and low fracture toughness is most important limiting factor for the battery integrity under mechanical loading. The sealant (surlyn) low-modulus is second-most important limiting factor. Embedded TFB do not have a detrimental effect on mechanical properties, they show good adhesion and load sharing with the composite structure. The adhesion to the laminate is stronger than the fracture toughness of the muscovite substrate. The electrical failure occurs at about 50% of the strain at failure of structural composite. In addition the embedding method and the relative stiffness mismatch between battery (both sealant and substrate) and CFRP laminate are critical parameters for strain concentration. A more ductile substrate and a sealant with higher modulus would increase load share and limits of utilization of externally-bonded or embedded batteries. TFB shape can also be optimized to minimize strain concentration. The successful embedding of all-solid-state thin-film batteries into composite laminates can find applications in commercial, military and aerospace industries. Based on the findings of this study a prototype of energy self-sustained structure, which incorporates flexible solar arrays and TFBs to harvest and store energy, has been manufactured, Figure D48.



Figure D48. Working prototype of energy self-sufficient CFRP stiffened panel with integrated TFBs and flexible solar array

#### D3 Study on the residual properties of thin film EHSS (Chasiotis)

##### Introduction

In this research program we: (a) investigated the residual stresses of Transparent Conductive Oxide (TCO) and the p-n junction diode thin film layers in commercial thin film solar cells by taking advantage of straight and “zig-zag” blister formation and by measurements of the curvature TCO-Si and Si thin films with 1  $\mu\text{m}$  thickness; (b) conducted a series of electrochemical and mechanical tests with thin-film composite Si (Si + acetylene black + PVDF) anodes and lithium cobalt oxide ( $\text{LiCoO}_2$  + acetylene black + PVDF) cathodes. In the first task, we observed that when both the TCO and p-n junction were present, telephone cord delaminations were formed, while when the TCO was removed, only straight delaminations formed. Calculations of the mean residual stresses from straight delaminations of Si films resulted in  $-463 \pm 115$  MPa, while telephone cord delaminations of TCO-Si layers provided a residual stress of  $-742 \pm 104$  MPa. Using strips of the TCO/p-n junction and the p-n junction alone the residual stress gradient of the bilayer was found to be  $170 \pm 15$  MPa/ $\mu\text{m}$ , while for the Si monolayer was  $172 \pm 12$  MPa/ $\mu\text{m}$ . In the second task we evaluated the interlaminar shear strength between the composite Si layer and the Cu substrate in an anode as  $123 \pm 48$  MPa. Si anodes were lithiated and delithiated under galvanostatic and potentiostatic conditions, and the morphological surface changes were optically recorded. The surface morphology changed mainly during lithiation but there were no significant changes observed in the surface images for the cathode samples after lithiation and delithiation. In-situ observations showed a thick solid-electrolyte interphase (SEI) forming on the electrode surface. Finally, the  $\text{LiCoO}_2$  composite layer was found to be structurally weak under small tensile stresses.



Thin film photovoltaic cells require a fraction of the material used in conventional solar cells while maintaining relatively high efficiency (Fthenakis, 2009). Thin film photovoltaic cells are comprised of a semiconductor p-n junction diode which is responsible for converting the energy of photons to electricity, a transparent conductive oxide (TCO) which acts as a protective layer, and a bottom contact. The circuit is completed with a metallic grid on the surface of the cell acting as the top contact. The most common semiconductor p-n junction material is silicon (Si), which is investigated in this project, while the TCO that provides a top metallic transparent contact, enables the transport of charge carriers, and acts as a protective layer for the p-n junction was zinc oxide (ZnO). A Kapton bottom contact and a thick Al substrate, with approximate thicknesses of 100 nm and 50  $\mu\text{m}$ , respectively, completed the thin film solar cells which were obtained from commercial sources. Figure D66(a) shows a cross-section of the solar cell film. Quantification of the mechanical properties of the thin film materials in a solar cell is a cumbersome task due to the small film thicknesses and the formation of cracks when bending or extensional loads were applied. Figures D67(a,b) show a region of the thin film photovoltaic cell which was subjected to bending and tension, resulting to fragmentation.

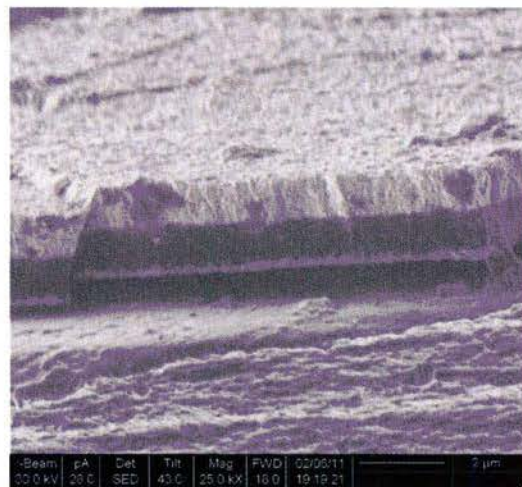
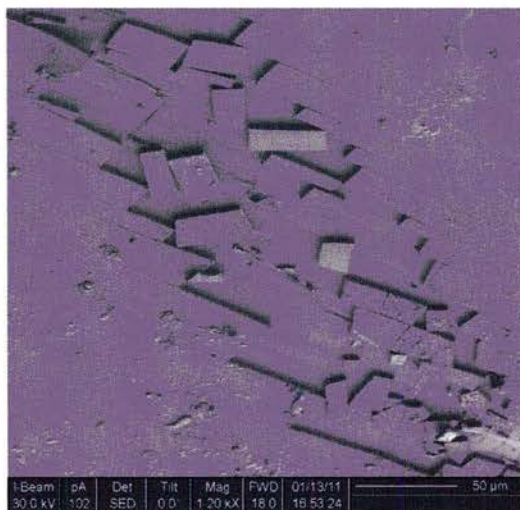
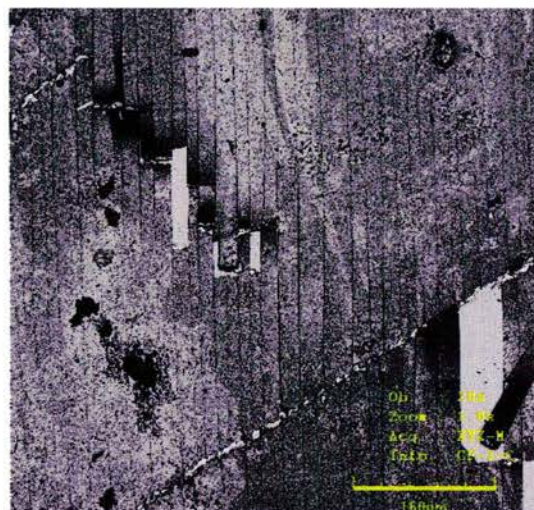


Figure D66. Cross-section of solar cell thin film showing the TCO at the top (light gray), the p-n junction diode in the middle (dark gray), and contact at the bottom (thin light gray layer).



(a)



(b)

Figure D67. Fragmentation of brittle thin film layers in a solar cell under (a) bending and (b) tension.



We quantified the film residual mean and gradient stresses, through an analysis of the blister profiles of delamination and by curvature measurements of freestanding film strips. Delamination was induced by immersing the photovoltaic cells in acetic acid to etch the polymeric contact and release the TCO and p-n junction. Application of bending to the photovoltaic films while immersed in acetic acid was adequate to peel the top ZnO layer from Si. Thus, the interfacial adhesion between the Si and ZnO layers was weak. When the ZnO layer was removed, the Si film (still attached to the substrate) formed straight delamination columns, Figure D68, due to the residual stresses in the Si layer. The mechanics of straight delamination have been analyzed before by modeling the thin film as a clamped-clamped buckled beam (Hutchinson, 1992), which leads to the following expressions for the buckling and the residual stresses (Volinsky, 2003):

$$\sigma_B = \frac{\pi^2}{12(1-\nu^2)} \frac{E}{\left(\frac{h}{b}\right)^2} \quad (D1)$$

$$\sigma_r = \frac{3}{4} \sigma_B \left( \frac{\delta^2}{h^2} + 1 \right) \quad (D2)$$

where E is the arithmetic mean of the elastic moduli of the two thin layers,  $\nu$  is the harmonic mean of Poisson's ratios, h is the film thickness,  $\delta$  is the blister height and b is the blister half-width. From Equations (D1) and (D2),  $\sigma_B = 160 \pm 49$  MPa and  $\sigma_r = 466 \pm 110$  MPa (residual mean stress).

When the photovoltaic films were simply immersed in acetic acid solution without the application of bending, the ZnO remained attached to the Si surface. However, the ZnO layer delaminated at edges where the photovoltaic films were cut, pointing out to the weak ZnO-Si interface. The same conditions that resulted in straight delaminations of only the Si layer in Figure D68, produced the "zig-zag" delaminated patterns shown in Figure D69(b), commonly known as telephone cord delaminations. Figure D69(a) is a close up of the ZnO surface showing its grain structure.

In order to calculate the residual stresses responsible for the formation of the telephone cord delaminations, the approximate values of the buckling and the residual stresses were calculated by using the same method as for the straight delaminations (Hutchinson, 1992). These calculations averaged  $128 \pm 30$  MPa and  $742 \pm 104$  MPa for the buckling and the residual stress, respectively.

The mean residual stress computed from the aforementioned delaminations is based on the Euler buckling theory and it does not account for the effect of the residual stress gradient which also contributes to the formation of a buckling delamination. Instead, the stress gradient can be calculated from the curvature of freestanding Si/ZnO strips. While the Si/ZnO bilayer is detached from the substrate, the cracks on the ZnO surface either propagate into the Si layer, creating a crack through the entire thickness of the bilayer, or in the weak interface causing delamination.

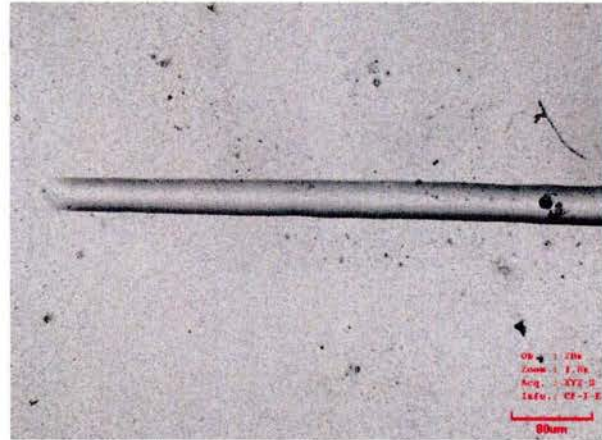


Figure D68. Straight delamination column propagating to the left of this image.



Figure D70(a) shows a Si mono-layer strip, and Figure D70(b) a Si/ZnO bi-layer strip that are the result of the aforementioned processes. The residual stress gradient is then calculated using curvature measurements. For the bi-layer sample, the composite moment of inertia is computed as (Timoshenko, 1925):

$$I^* = h^3 w \left( \frac{7}{24n} + \frac{1}{24} - \frac{\left(\frac{3}{n} + 1\right)^2}{32\left(1 + \frac{1}{n}\right)} \right) \quad (D3)$$

where  $h$  is the total thickness,  $w$  is the width of the beam and  $n$  is the ratio of the elastic moduli. The stress gradient in the Si monolayer was found equal to  $171 \pm 12$  MPa/ $\mu\text{m}$ , while for the bi-layer it was computed as  $170 \pm 15$  MPa/ $\mu\text{m}$ . While the two values appear to be the same it should be emphasized that they correspond to 1  $\mu\text{m}$  and 2  $\mu\text{m}$  thick layers and as a result, the latter were subject to a larger curvature.

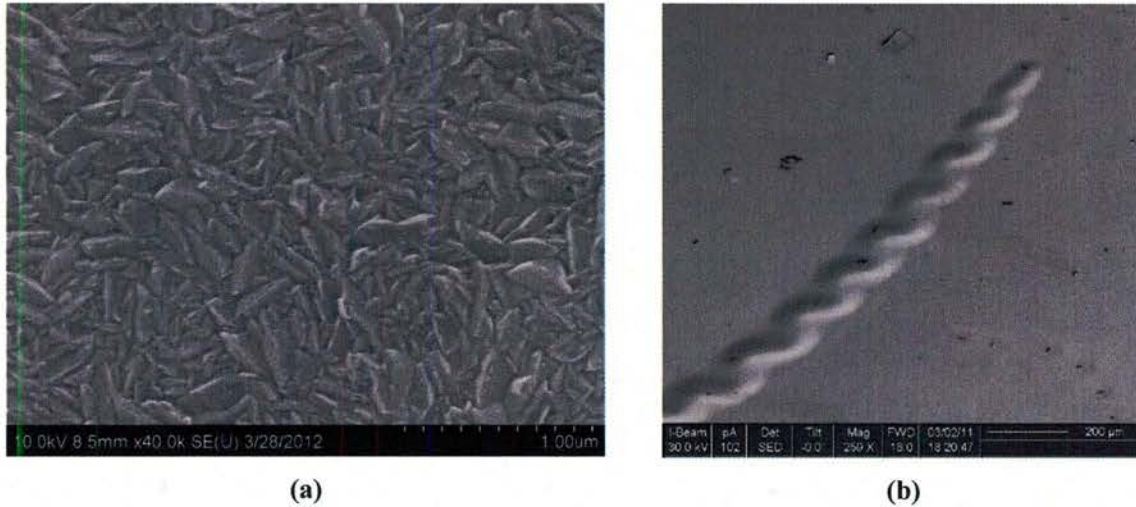


Figure D69. (a) Surface texture of ZnO, and (b) telephone cord delamination.

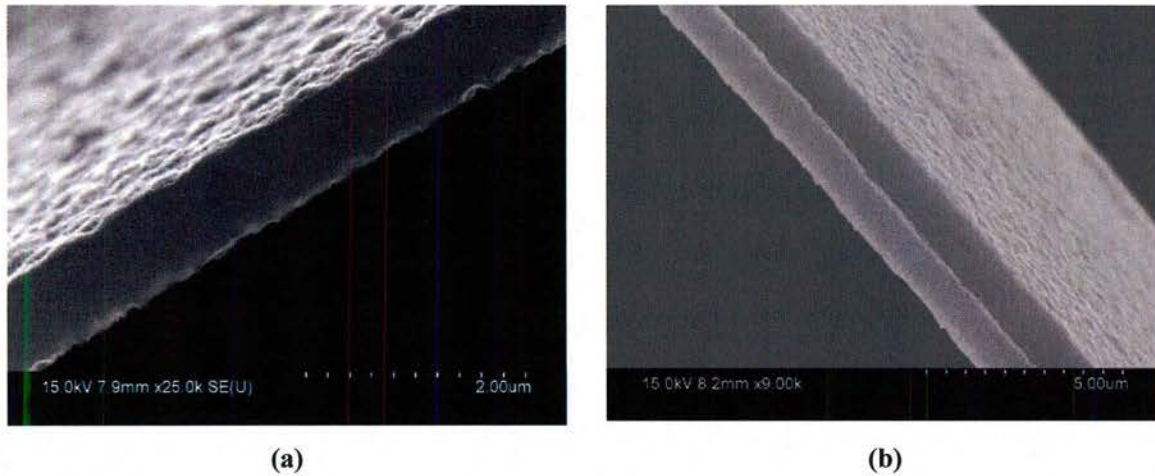


Figure D70. Cross-sections of (a) Si and (b) ZnO/Si bilayer films.

---

COMPOSITE ANODES AND CATHODES FOR  $\text{Li}^+$  BASED BATTERIES

---

The objective of this task was to investigate the failure of composite anode and cathodes for thin film batteries. The electrode materials were obtained in the Spring and in the Summer of 2011 from the University of Colorado at Boulder. Given the short duration of this project (7 months plus 7 months of no cost extension) we focused on the assembly and characterization of battery cells and in situ observations of the surface of the electrodes during lithiation/delithiation. Composite Si anode and  $\text{LiCoO}_2$  cathode samples were prepared by the research group of Prof. Se-Hee Lee (Associate Professor, Mechanical Engineering) at the University of Colorado at Boulder. They were composite aggregates spread over the surface of a Cu or an Al substrate, as shown in Figures D71(a,b). The anode were comprised of a mixture of 60%wt. Si particles, 20%wt acetylene black (AB), and 20%wt polyvinylidene difluoride (PVDF) binder, deposited as a slurry on a ( $\sim 19 \mu\text{m}$ ) Cu foil (total thickness  $\sim 50\text{--}55 \mu\text{m}$ ). The exact thickness of the composite Si layer varied significantly between different samples and within each sample. The cathode samples were made in a similar manner and were comprised of a mixture of  $\text{LiCoO}_2$  (83%wt), AB (7.5%wt) and PVDF (9.5%wt), on an Al foil. Figures D72, D73 show the surface details of the anode films.

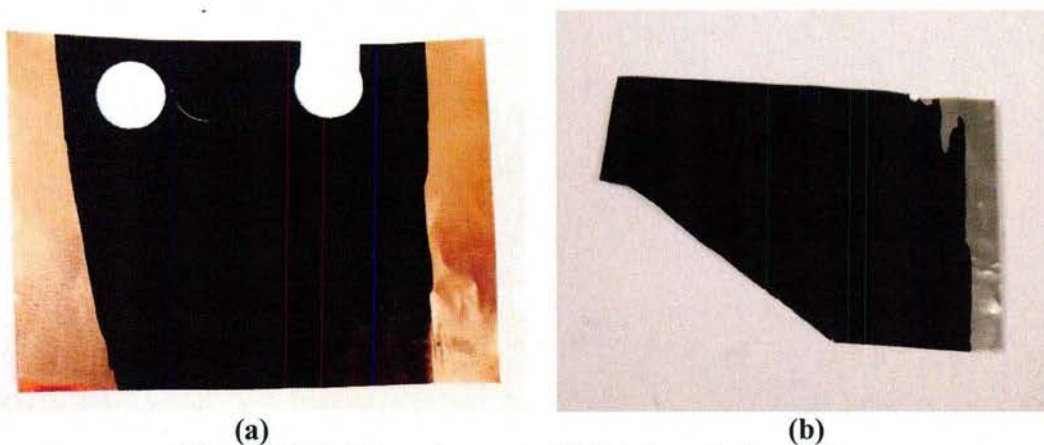


Figure D71. (a) Si anode sample (b)  $\text{LiCoO}_2$  cathode sample.

Experiments were carried out to measure the interlaminar shear strength between the active layer of the electrode (Si+AB+PVDF, henceforth referred to as the composite Si layer) and the Cu substrate. The tests were performed using a Bose ElectroForce® 3200. In total, 15 samples were prepared, shaped as long, narrow rectangular pieces. However, only 7 samples provided reliable results (as concluded from the load-displacement curves). The sample width was  $1.06 \pm 0.047 \text{ mm}$  and the length was  $\sim 10 \text{ mm}$ , with an actual gage length of  $\sim 8 \text{ mm}$ . The samples were bonded to the grips through the Si layer on one side using super-glue (Elmer's Fix-all adhesive), while on the other side the entire film was bonded using a 12-hour cure time epoxy. When subjected to tension, the end bonded through the Si layer delaminated from the Cu layer. The force at failure was used to calculate the shear strength of the Cu - composite Si interface. While the stress at the point of failure might also include the tensile strength of the Si layer alone, this was neglected in



our calculation as the Si layer was observed to have low strength. The results are tabulated in Table D13.

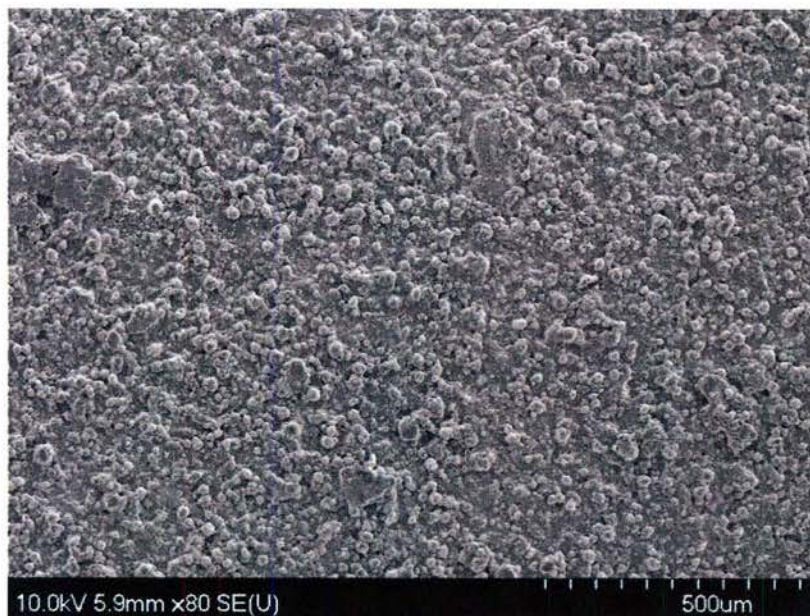


Figure D72. Texture of Si anode material (Si layer is visible).

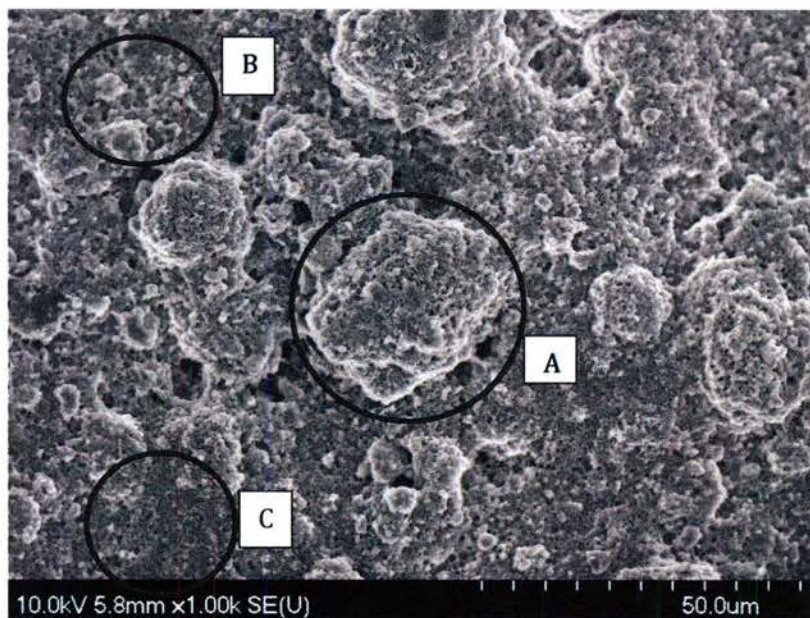


Figure D73. A. Si particles, B. acetylene black (AB) and C. PVDF binder.

Table D13. Shear strength of composite Si – Cu interface.

Sample	Width (mm)	Strength (MPa)
1	1.04	164.58
2	1.17	68.32
3	1.09	75.42
4	1.08	97.92
5	1.06	102.24
6	0.95	183.08
7	1.02	172.86
<b>Average</b>	1.06	123+48

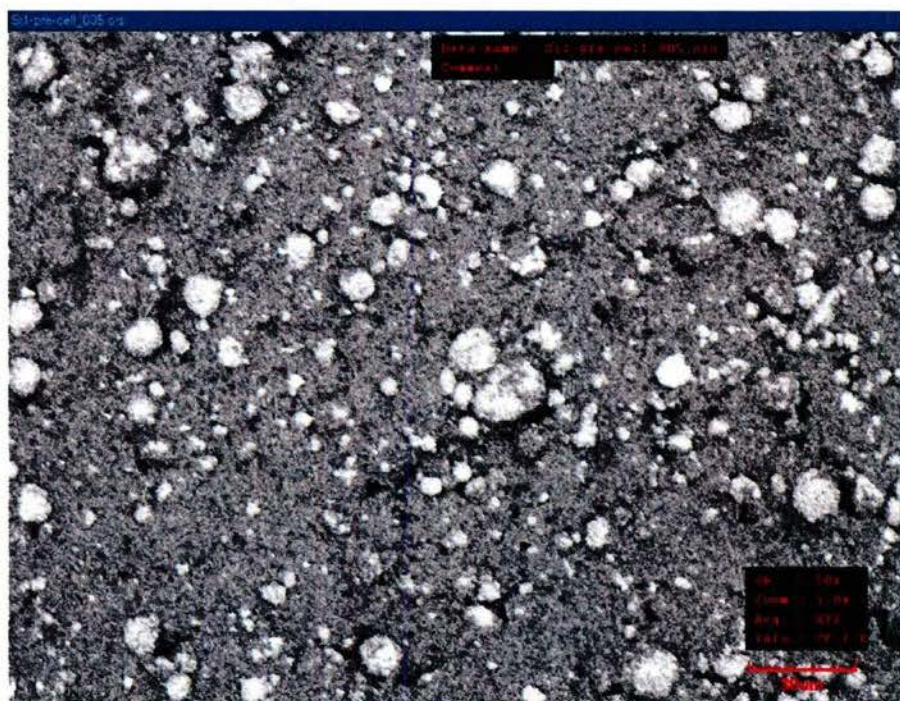
It should be noted that the interfacial strength values in Table D13 are quite high when compared to common engineering material systems. This may be the result of the unaccounted tensile force in the composite Si layer, and uncertainties in the calculation of the effective area subjected to interfacial shear stress. Nevertheless the particular experiment provides the means to test such interfaces and obtain quantitative results about the quality of bonding between the electrode (PVDF composite) and the current collector (metal).

In order to measure strain in the composite Si layer during lithiation and de-lithiation, the electrodes were subjected to both conditions under different electrochemical conditions and charge/discharge regimes. Subsequently, the surface topography was compared before and after each test using a confocal laser microscope. Comparative images from 5 different samples are presented in Figures D74-D79. A variety of failure modes were observed, varying from matrix surface cracking taking place during the first lithiation, to the formation of a form of SEI which covered almost the entire electrode.

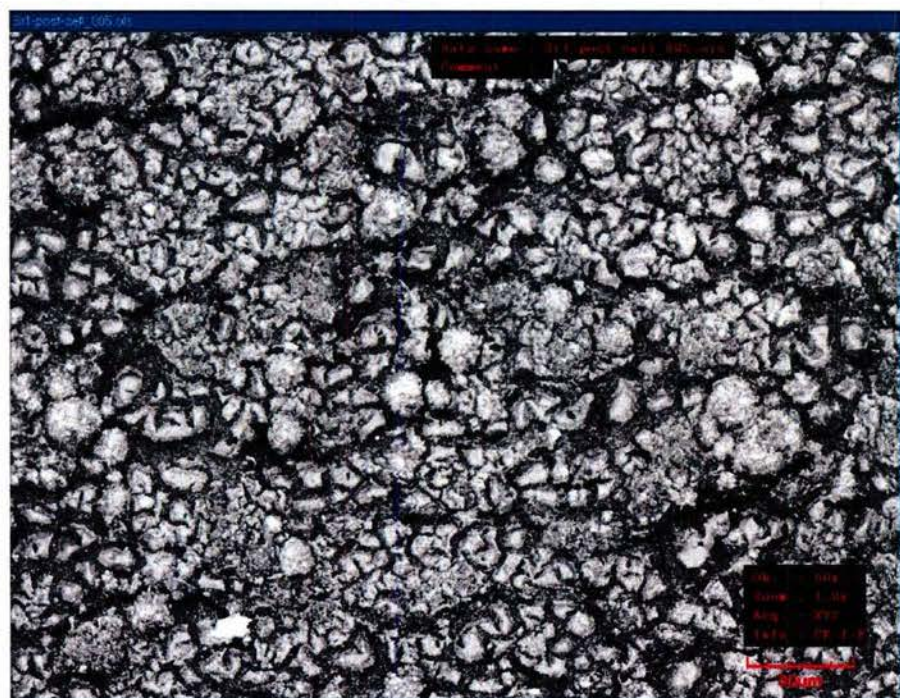
The average interlaminar shear strength between the electrode layer and the substrate was found to be of the order of 120 MPa for the composite Si anode samples. This implies that the metal-polymer composite layers were bonded well, thus loss in efficiency or failure of the cell or electrode due to debonding of these layers is unlikely.

The composite  $\text{LiCo}_2$  cathode samples on the other hand, could not be tested for interlaminar shear strength. The specimens failed under tension before the two layers could separate or debond. The peak stresses at failure were much lower than the interlaminar shear strength of the composite Si samples, due to the low strength of the Al substrate.





(a)



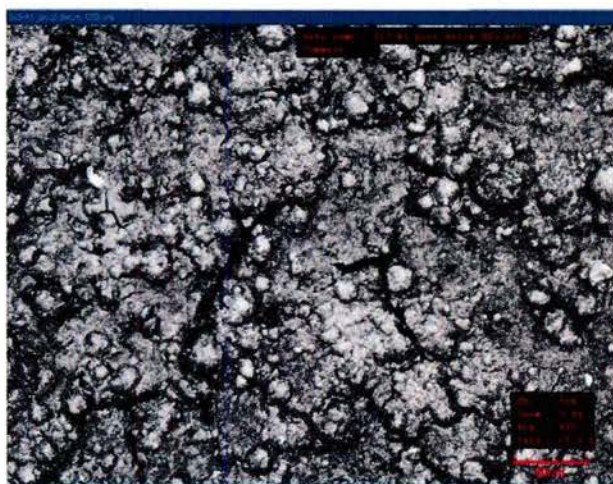
(b)

Figure D74. Surface of Si composite electrode sample 1 (a) before and (b) after lithiation at 50 $\times$  magnification (lithiated under potentiostatic conditions, with an applied voltage of 0.1 V).

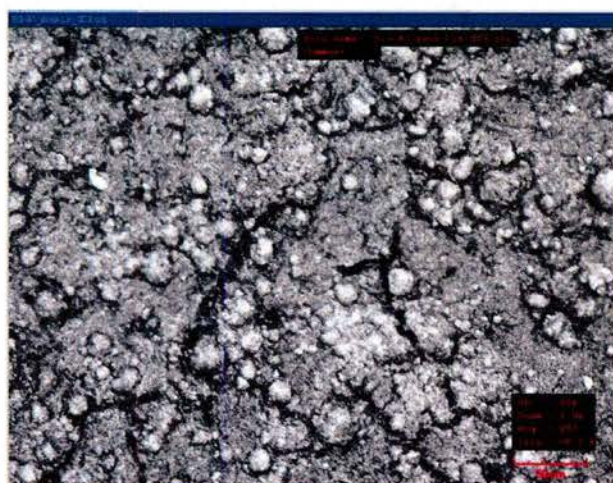




(a)



(b)



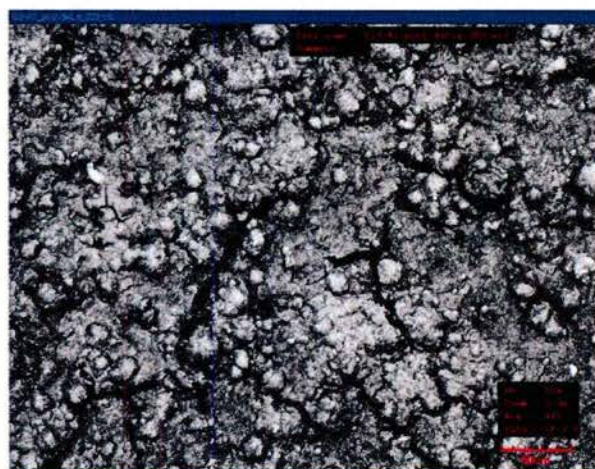
(c)

Figure D75. Surface of Si composite electrode sample 2 (a) before lithiation, (b) after lithiation and (c) after de-lithiation, at 100x magnification (lithiated for 10 minutes under potentiostatic conditions, with an applied voltage of 0.1 V, then fully de-lithiated at 1.5 V).

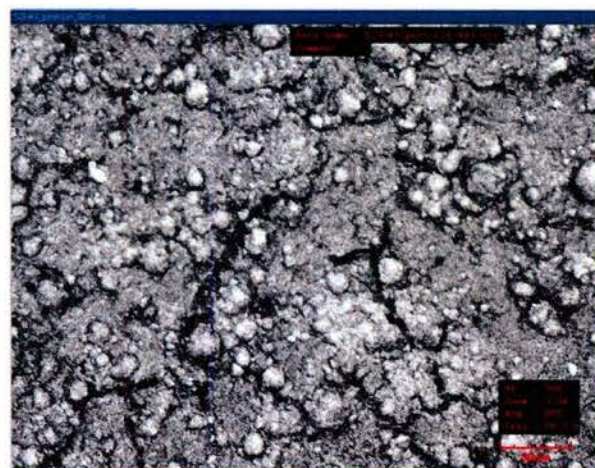




(a)



(b)

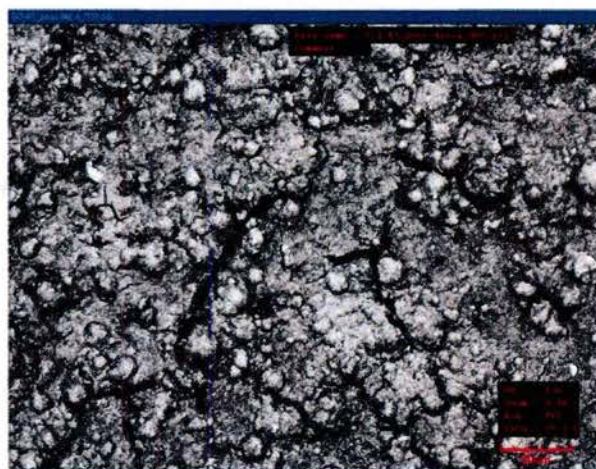


(c)

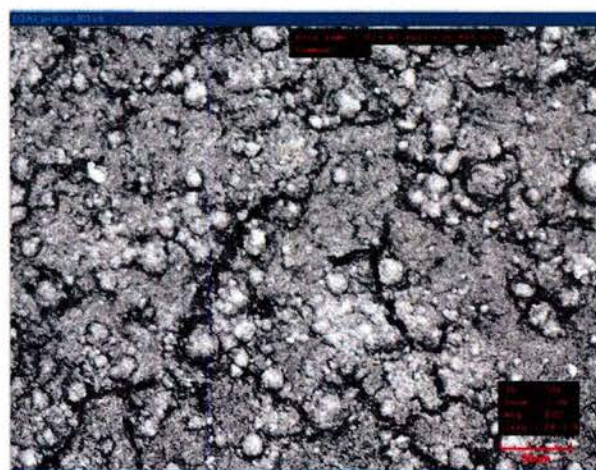
Figure D76. Surface of Si composite electrode sample 3 (a) before lithiation, (b) after lithiation and (c) after de-lithiation, at 50x magnification (lithiated for 20 minutes under potentiostatic conditions, with an applied voltage of 0.1 V, then fully de-lithiated at 1.5 V).



(a)



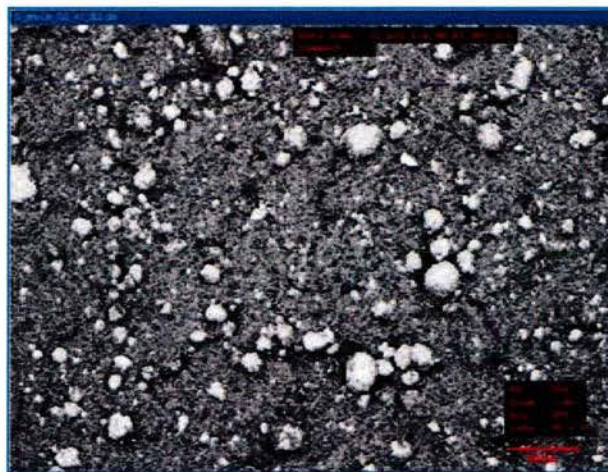
(b)



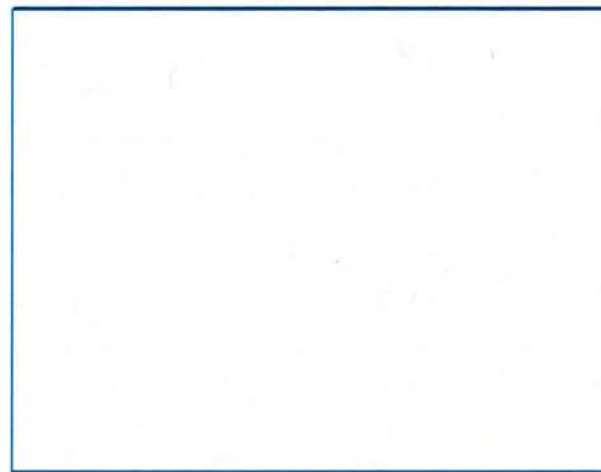
(c)

Figure D77. Surface of Si composite electrode sample 3 **(a)** before lithiation, **(b)** after lithiation and **(c)** after de-lithiation, at 100x magnification (lithiated for 20 minutes under potentiostatic conditions, with an applied voltage of 0.1 V, then fully de-lithiated at 1.5 V).

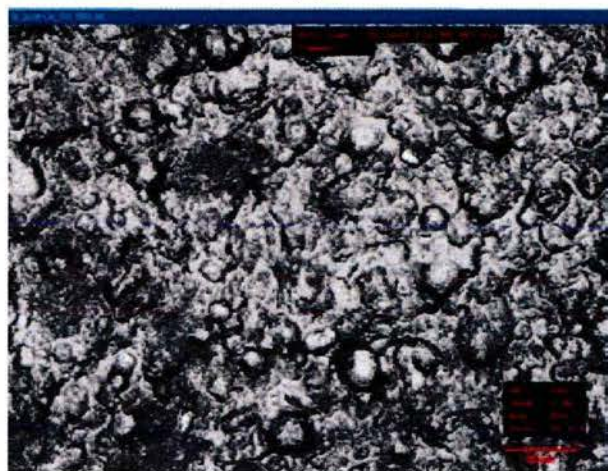




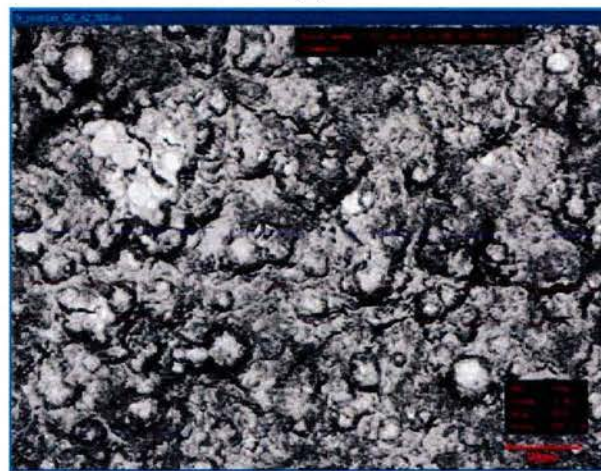
(a)



(b)



(c)



(d)

Figure D78. Two regions on the surface of Si composite electrode sample 4 (a,b) before and (c,d) after lithiation at 50 $\times$  magnification; (lithiated under galvanostatic conditions at very low charging rate,  $\sim C/300$ ).



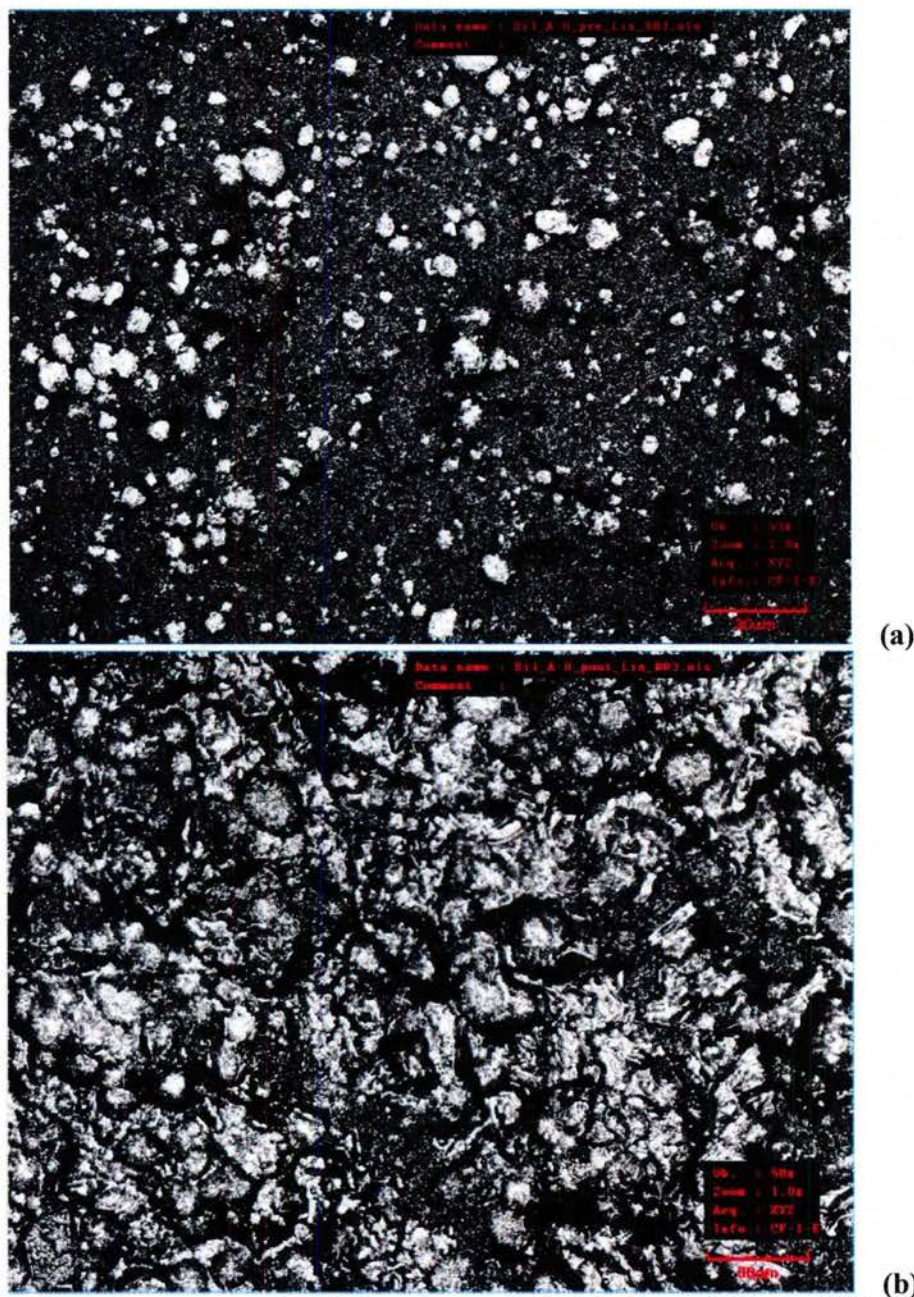


Figure D79. Surface of composite Si electrode sample 5 (a) before and (b) after lithiation at 50 $\times$  magnification (lithiated under galvanostatic conditions at 2C/3 charging rate).

The surfaces of the Si anode and the LiCoO<sub>2</sub> cathode supplied by the University of Colorado was significantly rough. In the case of Si based anodes, the peak-to-valley surface roughness was as high as 70  $\mu\text{m}$  (ignoring the occasional spikes often seen in confocal microscopy images) as shown in Figure D80. Whereas, in the LiCoO<sub>2</sub> cathode samples, the peak-to-valley surface roughness was of the order of 45  $\mu\text{m}$ , as shown in Figure D81. Due to the large surface features,



the use of an AFM to perform surface measurements, as was initially proposed, was ruled out. Instead, the electrode surfaces were compared using confocal laser microscopy. During the initial electrochemical experiments, no optically discernible changes occurred on the electrodes' surfaces (both Si and LiCoO<sub>2</sub>). This was attributed to incomplete lithiation/delithiation during the charge/discharge cycle. Experiments were then conducted using constant current and constant voltage. While the surface features changed drastically during lithiation, very limited changes took place upon de-lithiation. Furthermore, the Si particles rarely expanded or contracted, whereas the PVDF binder changed dramatically, as shown in Figures D74-D79. In-situ imaging of the Si electrode's surface revealed a dynamically forming and expanding surface layer which interfered with the optical analysis of the sample surface. After the charge-discharge cycle was over, this layer was deposited onto the surface accounting for the large changes in the surface morphology. The charging rate determined the extent of such changes on the electrode's surface, and barely any change was seen for very low charging rates ( $\sim C/100$  or less). This is expected, since the SEI would have sufficient time at low charging rates to dissolve back into the electrolyte without a residue.

An in-depth analysis of the relationship and interdependence between the electrochemical performance and mechanical properties of the Si anode and LiCoO<sub>2</sub> cathode materials would require well-prepared samples that would allow individual particles to be observed by time resolved microscopy techniques.

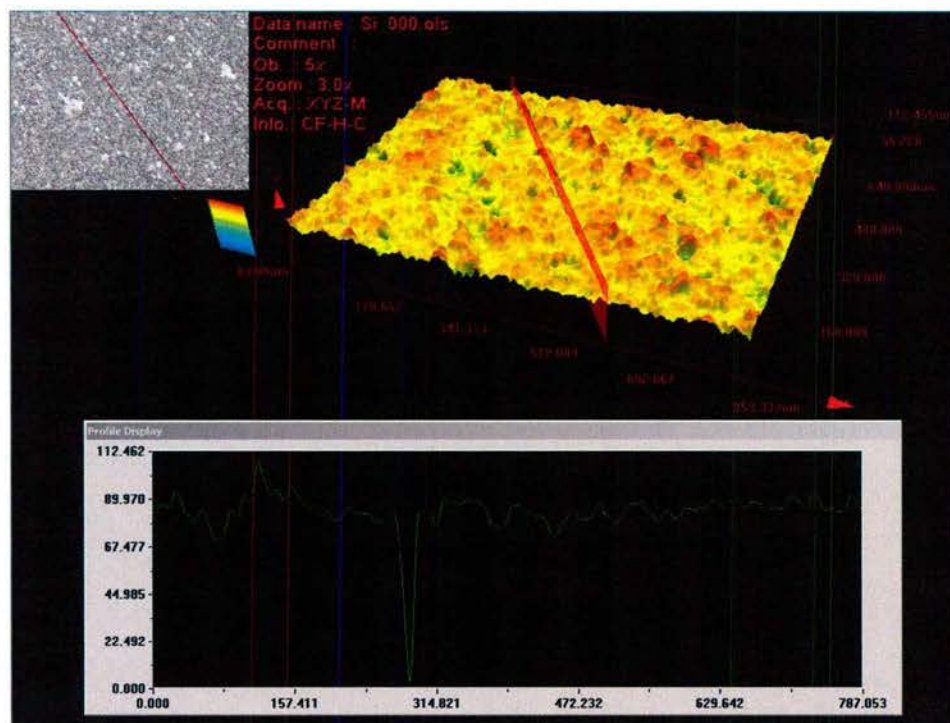


Figure D80. Surface roughness of composite Si anode.

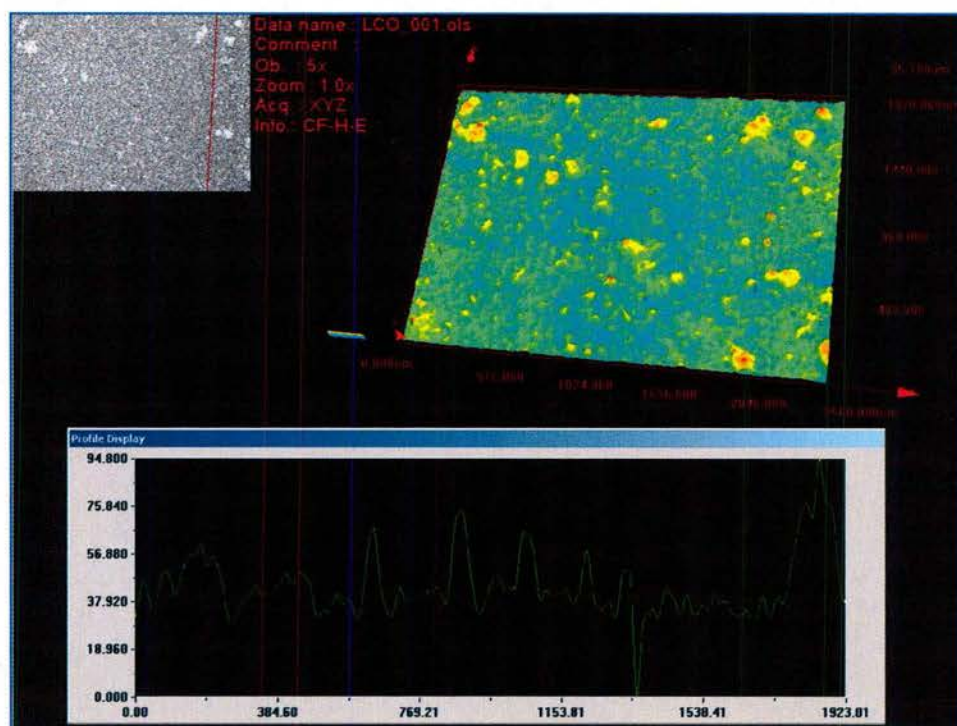


Figure D81. Surface roughness of composite  $\text{LiCoO}_2$  cathode.



## Task E: Design of Energy Storage System

This task includes the subtasks of designing Li-ion battery cathodes and super capacitors which have higher performance and durable in airborne use conditions.

### E-1: Design of new electrode materials (Cao, UW)

Li ion battery research can be divided into two parallel efforts: (1) developing coherent carbon cryogel – vanadium pentoxide nanocomposite electrodes for both enhanced specific power and specific energy and (2) new chemical compositions and new nanostructures. Three approaches have been taken to incorporate vanadium oxide to mesoporous carbon cryogels: (a) electrochemical deposition, (b) water electrolysis induced deposition of vanadium oxides due to the pH change at the vicinity of the carbon surface, and (c) sol electrophoretic deposition. Such coherent nanocomposites would offer excellent energy storage performance; however, so far no sufficient amount of vanadium oxide has been successfully incorporated into carbon cryogels yet. On a parallel effort,  $\text{MnO}_x$  nanowall arrays and  $\text{TiO}_2$  nanotube arrays have been successfully fabricated and tested for Li ion intercalation and demonstrated some promising results. Figure E1 shows the SEM images of both  $\text{MnO}_x$  nanowall arrays fabricated by water electrolysis induced deposition, and  $\text{TiO}_2$  nanotube arrays by means of acidic anodization.

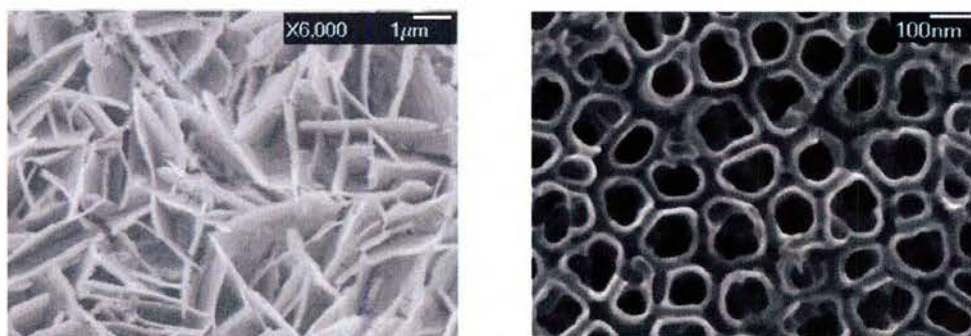


Figure E1. SEM images of  $\text{MnO}_x$  nanowall arrays and  $\text{TiO}_2$  nanotube arrays.

### E-2: Carbon Cryogel supercapacitors (Cao, UW)

The research in the past year has been focused on the understanding of the determining factors on the capacitance: microstructure or bonding. Our prior research has demonstrated that the capacitance varies significantly with the processing conditions. Different processing conditions result in different meso and microporous structures; however, the capacitance does not find linear relationship with porous structure. Our recent X-ray Raman spectroscopy experiments have ruled out the possibility that the different processing conditions may result in different chemical bonds in carbon cryogels (see Figure E2). It is concluded that the capacitance in carbon cryogel is solely dependent on meso and microporous structure; however, it is controlled by a combination of surface area, pore size and pore volume.

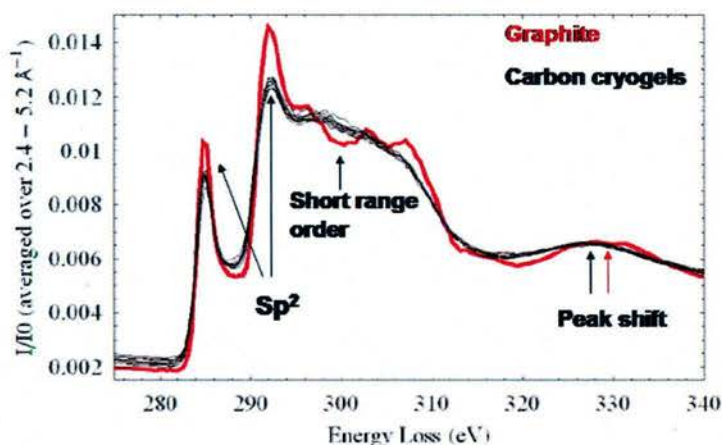


Figure E2. X-ray Raman scattering spectra of carbon cryogels fabricated under various processing conditions, showing all the samples have identical local structure and chemical bonding.

### E-3: Design of high performance electrolytes (Xu, UW)

Accomplishments:

12.5 mS/cm ion conductivity obtained in solution state

~3 mS/cm ion conductivity obtained in gel state

2.3 mS/cm ion conductivity obtained in solid state. See Fig. E3

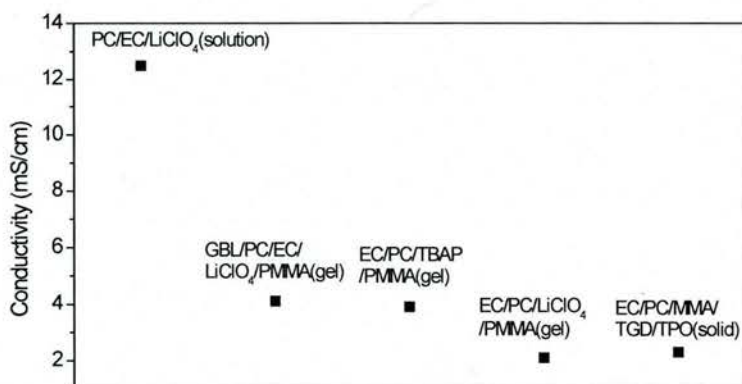


Figure E3 Ionic conductivity of different compositions and states (measured at room temperature).

### E-4 Microstructural Studies of Li Insertion(Lee, CU)

#### 1. Objectives

Traditional Li-ion batteries employ carbonaceous anodes, but projected performance targets for next-generation Li-ion batteries require new, higher capacity materials that can be electrochemically cycled in a stable manner. The most attractive candidate to replace carbon is silicon; it has the highest known capacity, is relatively low-cost, and is physically abundant. At present, the drawback with silicon is that a volume expansion on the order of ca. 300% occurs upon Li insertion that leads to rapid capacity fade during cycling. Creative approaches to realize highly-reliable electrodes are being pursued with nanometer-scale materials and geometric architectures; impressive results have been



obtained, but a fundamental understanding is still lacking. To this end, this project has focused on understanding the complex phenomena of Li insertion and extraction from Si, and developing novel nanostructured Si-based anodes which can address these critical technical issues with Si anodes.

## 2. Brief summary of the CU team progress toward the above objectives

We have reported the direct observation of microstructural changes of  $\text{Li}_x\text{Si}$  electrode with lithium insertion. HRTEM experiments confirm that lithiated amorphous silicon forms a shell around a core made up of the unlithiated silicon and that fully lithiated silicon contains a large number of pores of which concentration increases toward the center of the particle. Chemomechanical modeling has been employed in order to explain this mechanical degradation resulting from stresses in the  $\text{Li}_x\text{Si}$  particles with lithium insertion. Because lithiation-induced volume expansion and pulverization are the key mechanical effects that plague the performance and lifetime of high-capacity Si anodes in lithium-ion batteries, our observations and chemomechanical simulation provide important mechanistic insight for the design of advanced battery materials.

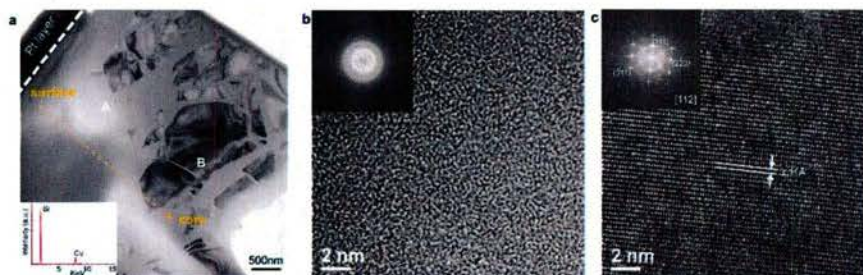


Figure E4. TEM images of  $\text{Li}_2\text{Si}$ . (a) BF image of  $\text{Li}_2\text{Si}$ . (b) HR and corresponding FFT of area A indicates that amorphous. (c) HR and corresponding FFT of area B indicates that Si crystalline phase along the [112] direction.

Figure E4a shows the bright field (BF) TEM image of the one single particle  $\text{Li}_2\text{Si}$  sample which has been known to exhibit a two-phase region. Energy dispersive X-Ray spectroscopy (EDS) measurements shown in inset of Figure E4a reveal that samples are mostly composed of Si, with a small amount of Cu detected. No signal from oxygen is detected, which implies that the TEM sample is never exposed to air. It is observed that the majority of the surface (which contacts the Pt) is amorphous phase while the inside area of the particle is filled with crystalline. Fig. E4b shows HR TEM image and corresponding FFT of area A, clearly indicating the area A is amorphous region. BF image, HR images and FFTs in Figure 1b and Figure 1c support that each area is formed with amorphous and crystalline Si phase (along [112] zone axis), respectively. This confirms that a two-phase region is formed with amorphous  $\text{Li}_x\text{Si}$  at the surface and crystalline Si phase in the core of particle as previously proposed. As shown in Figure 1a, amorphization due to Li insertion in Si begins from the surface. While it is widely accepted that amorphous  $\text{Li}_x\text{Si}$  initially forms at the surface with crystalline Si being maintained in the core of particles, there has never been precise observation of this phenomenon using TEM. Here, a  $\text{Li}_x\text{Si}$  particle maintaining a crystalline core with amorphization at the surface during Li insertion is confirmed. This observation also infers that Li concentration in the Si particle is surface dominant which explains mechanical



failure of Si anodes upon Li insertion. Thermodynamically stable Li-Si crystalline phases such as  $\text{Li}_{12}\text{Si}_7$ ,  $\text{Li}_7\text{Si}_3$  and  $\text{Li}_{13}\text{Si}_4$  are not shown in this region because the energy barrier for nucleation which is combined with surface and volume energy of nucleus, is higher when it is about to nucleate and thus makes meta-stable amorphous  $\text{Li}_x\text{Si}$ .

### 3. Accomplishments/New findings

- 1) Direct observation of microstructural transformations of lithiated Si anodes in all-solid-state Li half cells.
- 2) It has been shown that crystalline Si undergoes amorphization during lithiation and forms a crystalline phase after full discharge, known as  $\text{Li}_{15}\text{Si}_4$ . Two-phase regions have been observed by HRTEM showing amorphous  $\text{Li}_x\text{Si}$  at the surface and crystalline Si phase at the core of particles for the first time.
- 3) HRTEM observation of fully discharged Si anode samples revealed that particles consisting of high concentrations of pores in the Si particle are responsible for cracks and pulverization of Si during Li insertion.
- 4) The chemomechanical modeling has been employed to explain the generated stresses during Li insertion in relation to observed porosity pattern in detailed TEM study.

### E-5 Electrospinning fabrication and electrochemical properties of $\text{LiCoO}_2$ and $\text{Li}(\text{Ni}_{1/3}\text{Co}_{1/3}\text{Mn}_{1/3})\text{O}_2$ for cathodic material of Li-ion battery (Taya)

we have successfully fabricated single-wall carbon nanotubes embedded  $\text{LiCoO}_2$  nanofibers by electrospinning technique from a precursor solution containing lithium acetate/cobalt acetate/PVP (Polyvinylpyrrolidone) with different concentration of single wall carbon nanotubes (SWCNT). XRD (x-ray diffraction), Fig. E6, and SEM (scanning electron microscope), see Fig. E5 were performed to investigate the phase and microstructure of the electrospinning fibers respectively.

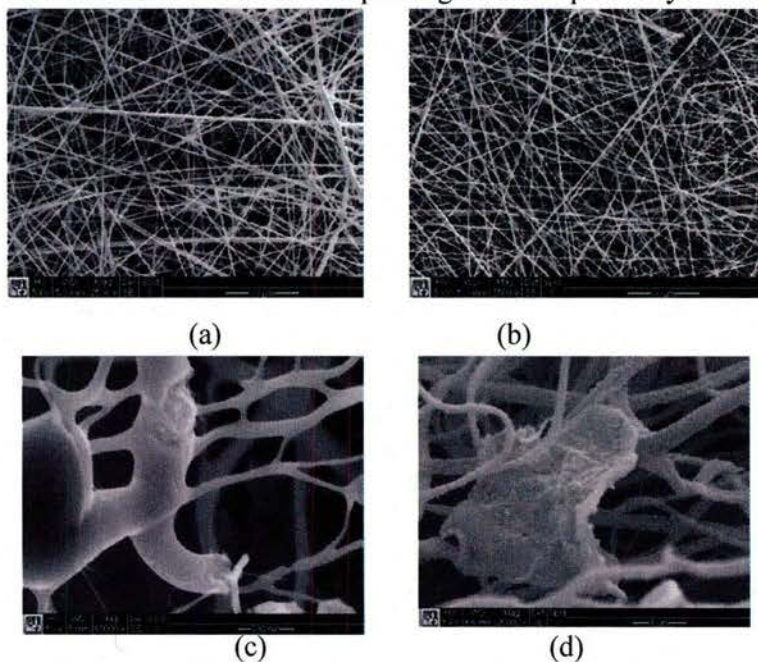


Fig. E5 SEM images of  $\text{LiCoO}_2$ -SWCNT with (a)(c) before calcine, (b)(d) after calcine



Fig.E5 shows the SEM photographs of the collected  $\text{LiCoO}_2$ -SWCNT nanofibers by electrospinning followed by calcination at  $500^\circ\text{C}$  for 30min. All the nanofibers are randomly distributed on the substrate. A closer look of pre-calcined nanofiber shown in Fig.E5(c) reveals that carbon nanofibers could be observed from a breaking point of composite fibers. Whereas Fig.E5(d) shows that nano-sized  $\text{LiCoO}_2$  particles was formed an junction points from which other nanofibers are branched

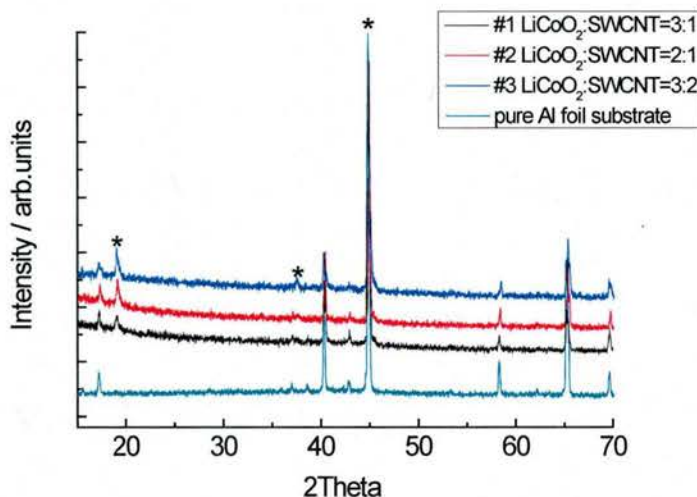


Fig. E6 XRD results for  $\text{LiCoO}_2$  nanofibers deposited on Al substrate after calcination at  $500^\circ\text{C}$  for 30 min

Fig.E6 shows the XRD patterns for  $\text{LiCoO}_2$  nanofibers with different  $\text{Li}^+/\text{Co}^{2+}/\text{SWCNT}$  starting ratio deposited on Al substrate after calcinations at  $500^\circ\text{C}$  for 30min. As shown in Fig.E6, the Al substrate has very strong background peak intensity in all samples, the three peaks marked with star indicated the three strongest peaks of the hexagonal  $\text{LiCoO}_2$ . Our previous report based on thick layer of  $\text{LiCoO}_2$  electrospun nanofibers indicates that  $\text{LiCoO}_2$  fabricated by similar method exhibited a pure crystalline  $\text{LiCoO}_2$  after calcination at  $500^\circ\text{C}$  for 30min. In our previous work, the impurity concentration in SWCNT (graphite, iron oxide) was too low, there was no peak in XRD corresponding these contaminants.

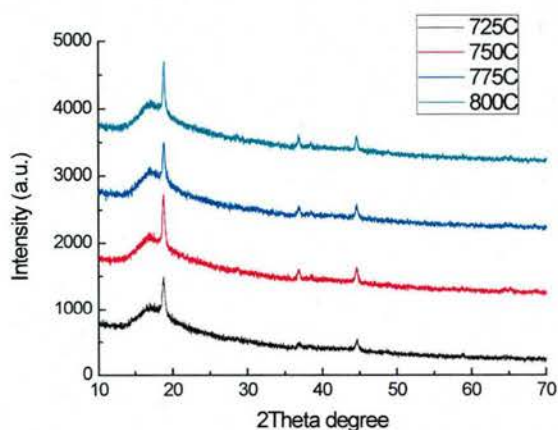


Fig.E7 XRD results for  $\text{Li}(\text{Ni}_{1/3}\text{Co}_{1/3}\text{Mn}_{1/3})\text{O}_2$  nanofibers deposited on Al substrate after calcination at different temperatures for 6 hours

Fig.E7 shows the XRD patterns for  $\text{Li}(\text{Ni}_{1/3}\text{Co}_{1/3}\text{Mn}_{1/3})\text{O}_2$  nanofibers after calcinations at 725 to 800°C for 6 hours. The patterns of three strongest peaks coincide very well with  $\text{LiCoO}_2$ . In fact, the peak pattern of  $\text{Li}(\text{Ni}_{1/3}\text{Co}_{1/3}\text{Mn}_{1/3})\text{O}_2$  was very similar to  $\text{LiCoO}_2$  and  $\text{LiNiO}_2$ , except that the peak position was in between of  $\text{LiCoO}_2$  and  $\text{LiNiO}_2$  due to its lattice parameter. Furthermore CV (cyclic voltammetry) and charge-discharge experiments were applied to characterize the electrochemical properties of composite nanofibers. To improve the capacity of cathode materials, more recent work of  $\text{Li}(\text{Ni}_{1/3}\text{Co}_{1/3}\text{Mn}_{1/3})\text{O}_2$  nanofiber based on electrospinning method has been done and the capacity has been dramatically improved. It is noteworthy that this nanostructured cathode offers high charge-discharge capacity even under high charge-discharge rate compared with conventional micro powder or film cathodes, therefore  $\text{SWCNT-LiCoO}_2$  composite nanofiber as well as  $\text{Li}(\text{Ni}_{1/3}\text{Co}_{1/3}\text{Mn}_{1/3})\text{O}_2$  nanofiber cathode may become promising candidates for high energy density cathodic materials of lithium-ion batteries.

The morphology of  $\text{Li}(\text{Ni}_{1/3}\text{Co}_{1/3}\text{Mn}_{1/3})\text{O}_2$  nanofiber by SEM was very similar to  $\text{LiCoO}_2$ -SWCNT nanofiber. Due to resolution limitation of SEM, identification of embedded SWCNT will be examined later by TEM. The average diameter of these fibers was found to be 200-500nm after calcination. The diameter of the nanofibers would depend on the PVP concentration as well as electrospin parameters.

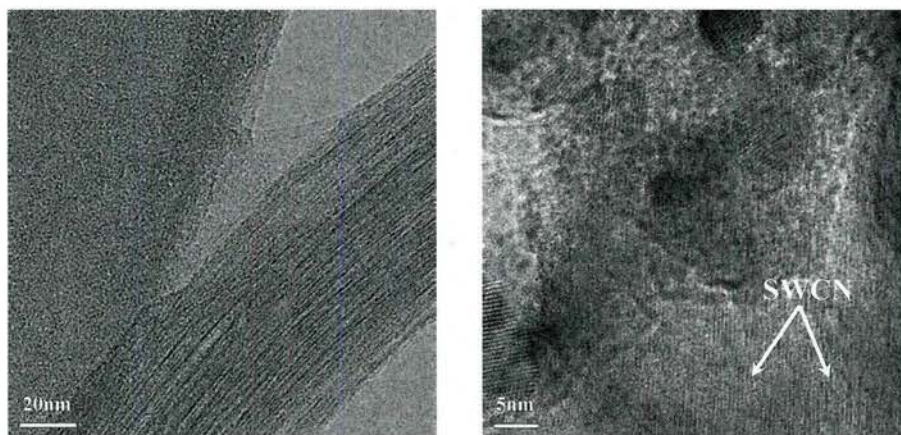


Fig.E8 TEM image of pure SWCNT (a) and SWCNT embedded within  $\text{LiCoO}_2$  (b)

Fig.E8 shows the TEM image of pure SWCNT and a bundle of SWCNT among  $\text{LiCoO}_2$  crystals. The SWCNT is characterized by rough tube wall morphology with low contrast, compared with higher contrast, sharp crystal planes of  $\text{LiCoO}_2$ . However, during the observation, the concentration of SWCNT was not as high as proposed according to material starting ratio, which means that only a small amount of SWCNT in electrospinning precursor solution was embedded into  $\text{LiCoO}_2$  nanofibers. This problem could be attributed to highly aggregated bundles of SWCNT, which was difficult to isolate even by ultrasonication.



In order to improve the capacity of cathode materials, the novel material with higher capacity such as  $\text{Li}(\text{Ni}_{1/3}\text{Co}_{1/3}\text{Mn}_{1/3})\text{O}_2$  was very promising candidate for lithium-ion battery. The discharge capacities at 2C of  $\text{Li}(\text{Ni}_{1/3}\text{Co}_{1/3}\text{Mn}_{1/3})\text{O}_2$  nanofiber with 5wt% MWCNT under different calcinations temperatures were tested and the best result with calcination temperature at 800°C are shown in Fig.9.

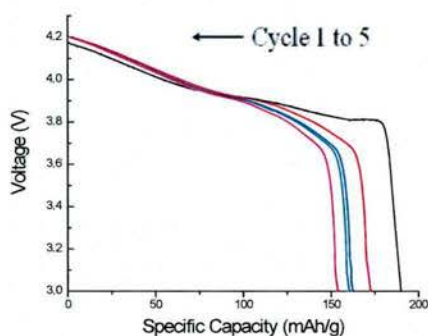


Fig.E9 Discharge capacity of the cathode based on  $\text{Li}(\text{Ni}_{1/3}\text{Co}_{1/3}\text{Mn}_{1/3})\text{O}_2$ -MWCNT nanofibers under current rate 2C

With the first discharge capacity of almost 190mAh/g, it clearly indicated that  $\text{Li}(\text{Ni}_{1/3}\text{Co}_{1/3}\text{Mn}_{1/3})\text{O}_2$ -MWCNT nanofibers show dramatically capacity improvement compared with  $\text{LiCoO}_2$ -SWCNT nanofiber. Even with some degradation after 5 cycles, the discharge capacity is still higher than 150mAh/g, indicating that  $\text{Li}(\text{Ni}_{1/3}\text{Co}_{1/3}\text{Mn}_{1/3})\text{O}_2$ -MWCNT nanofibers is a very promising candidate for high energy density lithium-ion batteries. In future, more work should be focused on how to improve the discharge stability for better cycleability.

## Progress Report: Task F Circuit Design for EHSS (Kuga)

### Objectives and Proposed tasks during the 1st year

During the first year, we have conducted the following projects under Task F: (1) Development of HF-VHF MMD antennas for a small UAV, (2) development of the control circuits for ECW and other conductive polymer devices, and (3) Integration of energy harvesting circuits and study of energy efficiency using the testbed.

#### (1) Development of HF-VHF MMD antennas for a small UAV

The unlicensed HF (27 MHz) or VHF (72 MHz) bands can be utilized for long distance communications or for beyond light-of-sight (BLOS) communications. BLOS communication is often called upon when hills and building are in the landscape. To attach an HF-VHF antenna to a small UAV (the wing span is less than 2 m), we have studied the modified meanderline dipole (MMD) antennas. The length of the existing dipole antennas was not suitable for small UAVs. For size efficiency, we designed the MMW antenna such that this antenna would fold into the top and bottom surfaces of the main wing. This folding would allow it to be embedded into the main wings. To optimize the antenna's performance, the design must include realistic air-frame materials such as composite wings.

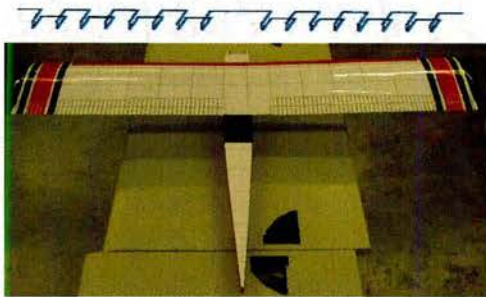


Fig. F-1 An example of a small UAV (bottom) and layout of the MMD antenna (top).

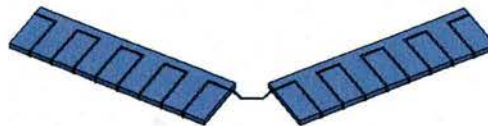


Fig. F-2 The 120° MMD antenna on dielectric material ( $\epsilon_r = 4$ )

Fig. F-1 shows an example of a small UAV as well as the layout of an MMD antenna. The width of the trace is 5 mm and the thickness is 0.5 mm of the MMD antenna. The total length of the MMD antenna is 1200 mm while the total width is 140 mm. The folded length in the MMD antenna is 20 mm. This antenna is designed at 50 MHz and the simulated antenna responses are shown in Fig. F-3.

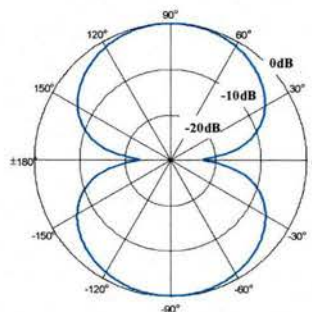
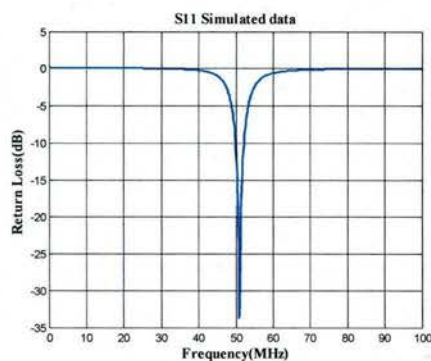


Fig. F-3 (left) Simulated  $S_{11}$  of the MMD antenna as shown in Fig. F-1. (right) Simulated E-plane radiation patterns of the MMD antenna at 50 MHz as shown in Fig. F-1

(2) Development of the control circuits for ECW and other conductive polymer devices  
We have developed a driving circuit for ECW which can accommodate solar cells.

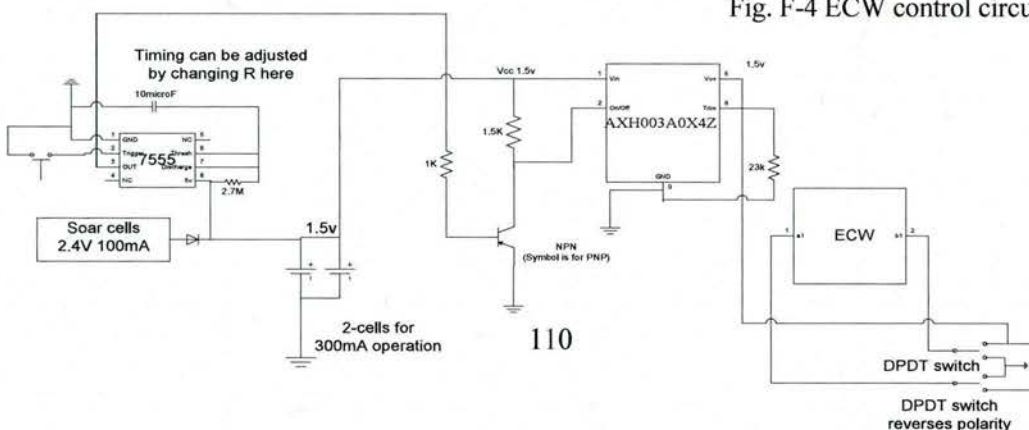


Fig. F-4 ECW control circuit



(3) Integration of energy harvesting circuits and study of energy efficiency  
To test the performance of the energy harvesting system, we have developed the testbed using existing devices.

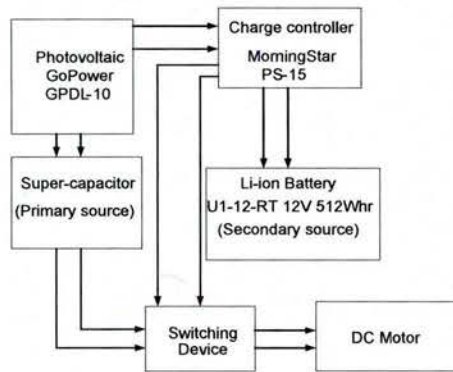


Fig. F-5 Testbed for energy harvesting system

#### Task G. Multimode Energy Harvesting for ISR/MAV Missions (Inman)

**Goals** Our subcontracted task is to examine the use of piezoelectric materials for harvesting ambient energy. Our goals this period included examining the state of the art in piezoceramic based harvesting and discovering the best predictive models for harvesters. The follow on goal is to form these predictive models into useful design rules and to transition these to AF applications. An additional goal is to characterize ambient energy sources for mechanical harvesting.

#### Main findings

The main discoveries and inventions are summarized as follows:

Piezoelectric cantilever harvesters as currently existing at the beginning of this MURI where modeled in correctly. So in the first year of the MURI new, higher fidelity models where derived and experimentally clarified which corrected the existing models.

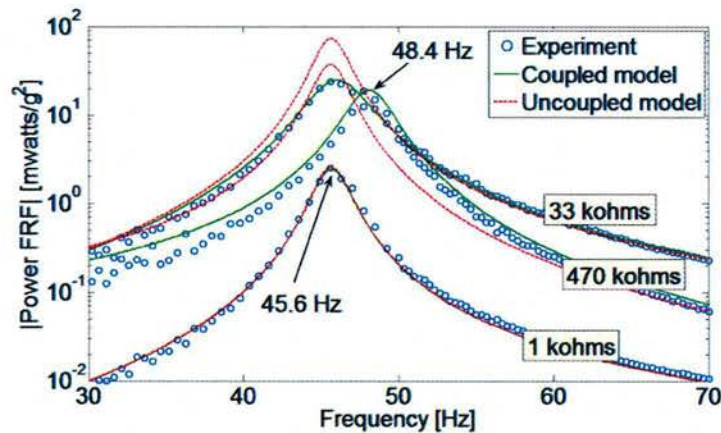


Figure G-1 Plots showing the error of over prediction of early energy harvesting models and the corrective model developed under the MURI which agrees with experimental data. The red dashed line is the previous theory based on uncoupled modeling and the green line is the improved model, which agrees with experiments.

During the second year we addressed structural integration of harvesting materials. The idea developed was that each wing has a spar. The spar has a designed volume, mass and stiffness. We kept these three parameters fixed while we adjusted the amount of piezoelectric material (PZT) in the spar to optimize the energy we can extract as the spar vibrations. Our initial flight test resulted in 50 micro watts but this was not optimized. Our colleagues at Colorado the used this model to optimize the distribution of PZT throughout the spar. We provided them with a mechanics model that they used their code on. We also performed some flight tests in order to determine how much vibration energy was available in a UAV. We also discovered the concept of strain nodes which leads to cancellation of power out and restricts the design space.

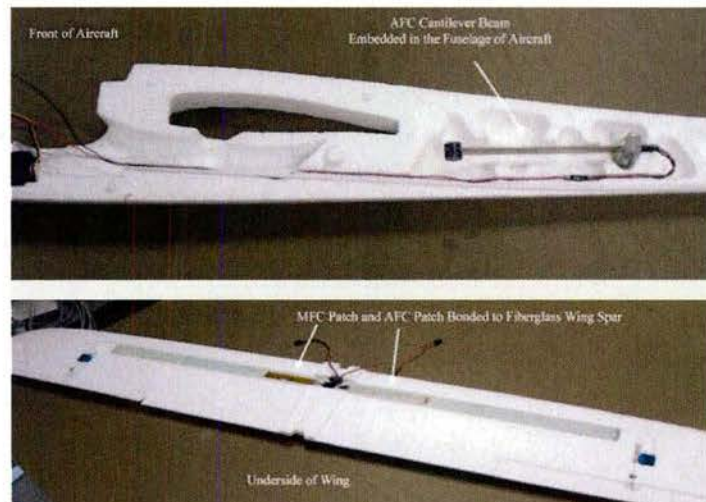


Figure G-2 Piezoelectric harvesting devices integrated in the body of a small UAV as a cantilever (top photo) and layered into the spar (bottom picture).



During the third year we investigated the concept of using “L-shaped” piezoceramic transducers to try and improve the amount of energy obtained from a given input vibrations. We also investigated using both piezoceramic transduction and electromagnetic transduction in the same device. The PZT produces high voltage but low current where as the electromagnetic transduction produces high current but low voltage at small levels of vibration. Hence the combination provides a high enough voltage to charge a battery and a high enough current to increase the charge time.

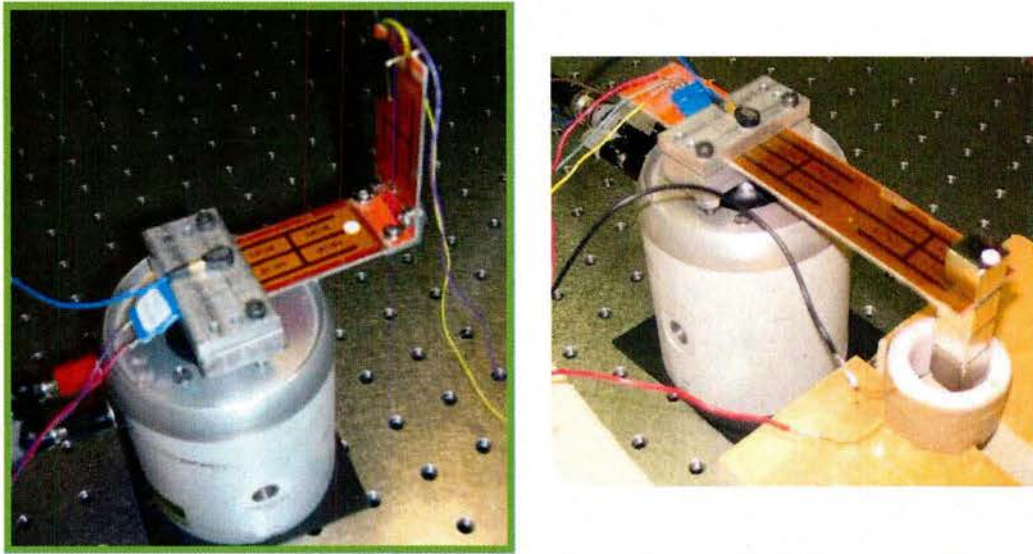


Figure G-3 On the right is the L-shaped configuration used to introduce nonlinear behavior and on the left is the combined piezoelectric and electromagnetic harvester.

During the forth year we integrated thin film batteries into our wing spar along with PZT for harvesting and developed the concept of a “self-charging” structure. We looked and strength tests and characterized the multifunctionality of the self charging spar in terms of weight, strength and performance.

During the last year several new discoveries where made and several new devices designed and fabricated. First it was discover through a series of experiments and analytical derivations that the amount of energy harvested from mechanical motion could be increased an order of magnitude by introducing nonlinear behavior into a cantilever-harvesting configuration. This was further expanded to structural systems by using by-stable composite materials. Last we derived the mathematical models for and experimentally validated the harvesting of energy through aeroelastic phenomena.

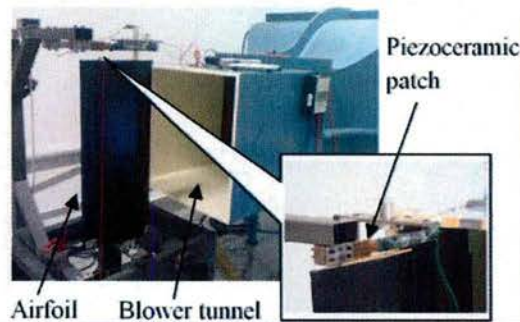


Figure G-4 Experiment to validate the theory that energy harvested from light through wing vibration produces usable electrical energy and increases the flutter speed.

Our second group of achievements consisted of designing, modeling and fabricating self charging structures which gather energy from both solar arrays and from mechanical vibrations. This system level approach to multifunctional structures forms a multi-mode harvesting and storage device consisting of

1. A piezoceramic energy harvesting device
2. A thin film solar panel
3. A thin film battery
4. Electronics to combine both forms of energy into a single battery

The result was fashioned into a wing spar of a model airplane and flown. The spar itself was tested in the laboratory illustrating the proof of concept. Strength analysis was performed along with a measure of multifunctionality based on the flight formulation put forth by Thomas, et. al.

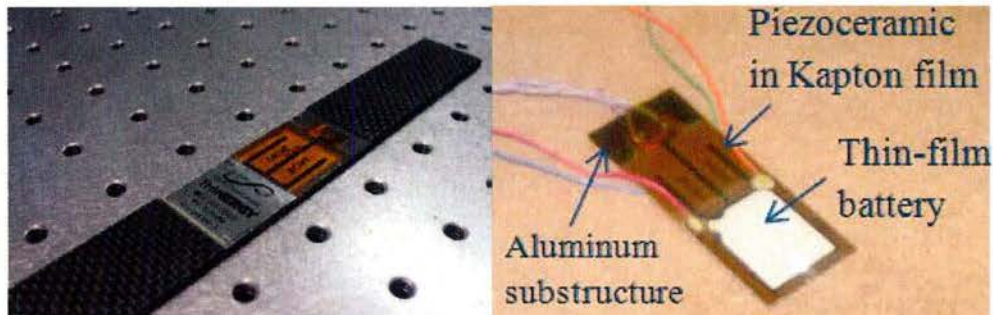


Figure G-5 Integrated self charging with spar including harvesting element as well as storage element.



### **Chapter 3 List of personnel supported by this grant**

University of Washington team:

#### **3. List of Personnel**

##### **3.1. University of Washington**

ME department: The faculty being supported are Taya (2006-2011), Xu(2006-2009), while the post doctors being supported are , Kikuchi(2006-2008), Nagata(2006-2009), Furukawa (2009), and graduate students being supported are: PhD student, HeeSeok Kim(2006-2011), MS students , Eli Baldwin (2008-2009), Erin Black (2007-2009).

MSE department: Faculty supported is Cao, the graduate students supported are Ying Wang (PhD, 2006) ,Tammy Chou (PhD, 2006), Saghar Sepehri (PhD, 2008), Dawei Liu (PhD, 2010), Betzaida Garcia (PhD, 2010)

EE department: Faculty supported is Kuga, graduate student supported is Jun-ho Cha (Completed Ph.D. 2006) who was supported as post doc thereafter through 2007. UG students supported are J. Spaulding and M. Stonebeck.

ChemE department: Faculty supported is Jenekhe, the post doctor supported is Hao Xin,, the PhD graduate students supported partially are Yan Zhu, PhD ,Tricia Bull, Pei-Tzu Wu,

AA department: the faculty supported is Feraboli, and the PhD student supported is Federico Gasco(2009-2011).

##### **3.2 UCLA**

The faculty supported are Hahn, and Ju, the graduate students supported are Jin Sung Kang, Gilhwan Cha, Yujie Tang, Yujia Zhan.

##### **3.3 University of Colorado**

The faculty supported are Dunn, Maute, Yang, Lee while the graduate students supported are Stephanie Golmon, Chris Deluca and Anton Evgrafov

##### **3.4 Virginia Tech**

The faculty supported is Inman, while the graduate students supported are

##### **3.5 University of Illinois at Urbana-Champaign**

The faculty supported is while the graduate students supported are Dimitrios Antartis, and Ankit Verma.

## 4. List of Publications

### 4.1 University of Washington

#### Jenekhe's publications

1. Zhu, Y.; Champion, R. D.; Jenekhe, S. A. "Conjugated Donor-Acceptor Copolymer Semiconductors with Large Intramolecular Charge Transfer: Synthesis, Optical Properties, Electrochemistry, and Field Effect Carrier Mobility of Thienopyrazine-Based Copolymers." *Macromolecules* **2006**, *39*, 8712-8719.
2. Zhu, Y.; Kulkarni, A. P.; Wu, P.-T.; Jenekhe, S. A. "New Ambipolar Organic Semiconductors. 1. Synthesis, Single-Crystal Structures, Redox Properties, and Photophysics of Phenoxazine-Based Donor-Acceptor Molecules." *Chem. Mater.* **2008**, *20*, 4200-4211.
3. Kulkarni, A. P.; Zhu, Y.; Babel, A.; Wu, P.-T.; Jenekhe, S. A. "New Ambipolar Organic Semiconductors. 2. Effects of Electron Acceptor Strength on Intramolecular Charge Transfer Photophysics, Highly Efficient Electroluminescence, and Field-Effect Charge Transport of Phenoxazine-Based Donor-Acceptor Materials." *Chem. Mater.* **2008**, *20*, 4212-4223.
4. Liu, C. L.; Tsai, J. H.; Lee, W. Y.; Chen, W. C.; Jenekhe, S. A. "New Didecyloxyphenylene-Acceptor Alternating Conjugated Copolymers: Synthesis, Properties, and Optoelectronic Device Applications." *Macromolecules* **2008**, *41*, 6952-6959.
5. Wu, P. T.; Kim, F. S.; Champion, R. D.; Jenekhe, S. A. "Conjugated donor-acceptor copolymer semiconductors. synthesis, optical properties, electrochemistry, and field-effect carrier mobility of pyridopyrazine-based copolymers." *Macromolecules* **2008**, *41*, 7021-7028.
6. Xin, H.; Kim, F. S.; Jenekhe, S. A. "Highly Efficient Solar Cells Based on Poly(3-butylthiophene) Nanowires." *J. Am. Chem. Soc.* **2008**, *130*, 5424-542.
7. Xin, H.; Ren, G. Q.; Kim, F. S.; Jenekhe, S. A. "Bulk Heterojunction Solar Cells from Poly(3-butylthiophene)/Fullerene Blends: In Situ Self-Assembly of Nanowires, Morphology, Charge Transport, and Photovoltaic Properties." *Chem. Mater.* **2008**, *20*, 6199-6207.
8. Wu, P. T.; Xin, H.; Kim, F. S.; Ren, G. Q.; Jenekhe, S. A. "Regioregular Poly(3-pentylthiophene): Synthesis, Self-Assembly of Nanowires, High-Mobility Field-Effect Transistors, and Efficient Photovoltaic Cells." *Macromolecules* **2009**, *42*, 8817-8826.
9. Wu, P. T.; Ren, G. Q.; Li, C. X.; Mezzenga, R.; Jenekhe, S. A. "Crystalline Diblock Conjugated Copolymers: Synthesis, Self-Assembly, and Microphase Separation of Poly(3-butylthiophene)-b-poly(3-octylthiophene)." *Macromolecules* **2009**, *42*, 2317-2320.
10. Xin, H.; Guo, X. G.; Kim, F. S.; Ren, G. Q.; Watson, M. D.; Jenekhe, S. A. "Efficient solar cells based on a new phthalimide-based donor-acceptor copolymer semiconductor: morphology, charge-transport, and photovoltaic properties." *J. Mater. Chem.* **2009**, *19*, 5303-5310.
11. Wu, P. T.; Bull, T.; Kim, F. S.; Luscombe, C. K.; Jenekhe, S. A. "Organometallic Donor-Acceptor Conjugated Polymer Semiconductors: Tunable Optical, Electrochemical, Charge Transport, and Photovoltaic Properties." *Macromolecules* **2009**, *42*, 671-681.



12. Bull, T. A.; Pingree, L. S. C.; Jenekhe, S. A.; Ginger, D. S.; Luscombe, C. K. "The Role of Mesoscopic PCBM Crystallites in Solvent Vapor Annealed Copolymer Solar Cells." *ACS Nano* **2009**, 3, 627-636.

**Cao's list of publications:**

1. Y. Wang and G.Z. Cao, "Synthesis and Electrochemical Properties of InVO<sub>4</sub> Nanotube Array Electrode," *Journal of Materials Chemistry* **17**, 894-899 (2007).
2. T.P. Chou, Q.F. Zhang, G.E. Fryxell, B. Russo, and G.Z. Cao, "Dependence of Dye Adsorption and Energy Conversion Efficiency on Titania Particle Morphology and Size," *Journal of Physical Chemistry C* **111**, 6296-6302 (2007).
3. T.P. Chou, Q.F. Zhang, G.E. Fryxell, and G.Z. Cao, "Dye-Sensitized Hierarchically Structured ZnO Solar Cells for Highly Efficient Energy Harvesting," *Advanced Materials* **19**, 2588-2592 (2007).
4. T.P. Chou, Q.F. Zhang, and G.Z. Cao, "Influences of Dye Loading Conditions on Energy Conversion Efficiency in ZnO and TiO<sub>2</sub> Dye Sensitized Solar Cells," *Journal of Physical Chemistry C* **111**, 18804-18811 (2007).
5. G.Z. Cao and D.W. Liu, "Template-based Synthesis of Nanorod and Nanowire Arrays," (*Review Article*), *Advances in Colloid and Interface Science* **136**, 45-64 (2008).
6. D.W. Liu, Q.F. Zhang, P. Xiao, B.B. Garcia, Q. Guo, R. Champion, and G.Z. Cao, "Hydrous Manganese Oxides Nanowall Electrodes for Enhanced Lithium Ion Intercalation," *Chemistry of Materials* **20**, 1376-1380 (2008).
7. Y. Wang and G.Z. Cao, "New Developments of Nanostructured Cathode Materials for Highly Efficient Lithium Ion Batteries," (*Review Article*), *Advanced Materials* **20**, 2251-2269 (2008). (*The Best Paper of Advanced Materials in 2008, 12 out of ~1,000 papers*)
8. Q.F. Zhang, T.P. Chou, B. Russo, S.A. Jenekhe, and G.Z. Cao, "Light Scattering Enhanced Energy Conversion Efficiency in Hierarchically-Structured ZnO Dye Sensitized Solar Cells," *Advanced Functional Materials* **18**, 1654-1660 (2008).
9. B.B. Garcia, A. Feaver, G.T. Seidler, and G.Z. Cao, "Effect of Pore Morphology on Electrochemical Properties of Carbon Cryogel Supercapacitors," *Journal of Applied Physics* **104**, 014205 (9p) (2008).
10. D.W. Liu, P. Xiao, Y.H. Zhang, B.B. Garcia, Q.F. Zhang, Q. Guo, R. Champion, and G.Z. Cao, "Lithium Ion Intercalation Properties of TiO<sub>2</sub> Nanotube Arrays Annealed in N<sub>2</sub>," *Journal of Physical Chemistry, C* **112**, 11175-11180 (2008).
11. J. Liu, G.Z. Cao, Z.G. Yang, D. Dubois, X.D. Zhou, D.H. Wang, and G.L. Graff, "Oriented Nanostructures for Energy Conversion and Storage," *ChemSusChem* **1**, 676-697 (2008). (*cover article*)
12. T.P. Chou, B. Russo, Q.F. Zhang, and G.Z. Cao, "Significant Enhancement of Energy Conversion Efficiency of Dye-Sensitized TiO<sub>2</sub> Solar Cells with the Addition of ITO and FTO," *Journal of Nanophotonics* **2**, 023511 (11 pages) (2008).
13. S. Sepehri, B.B. García, and G.Z. Cao, "Influences of Surface Chemistry on Dehydrogenation in Carbon Cryogel - Ammonia Borane Nanocomposites," *European Journal of Inorganic Chemistry*, 599-603 (2009)

14. S. Sepehri, B.B. García, Q.F. Zhang, and G.Z. Cao, "Enhanced Electrochemical Properties of Carbon Cryogels by Surface Chemistry Alteration with Boron and Nitrogen," *Carbon* **47**, 1436-1443 (2009).
15. D.W. Liu, P. Xiao, Q.F. Zhang, B.B. Garcia, Q. Guo, Y.H. Zhang, and G.Z. Cao, "Mesoporous Hydrous Manganese Dioxide Nanowall Arrays with Large Lithium Ion Intercalation Capacity," *Advanced Functional Materials* **19**, 1015-1023 (2009). (*Editor's highlight in Science* **324**, 1242 (2009))
16. T.P. Chou, X.Y. Zhou, and G.Z. Cao, "SiO<sub>2</sub>-TiO<sub>2</sub>Xerogels for Tailoring the Release of Brilliant Blue FCF," *Journal of Sol-Gel Science and Technology* **50**, 301-307 (2009).
17. Y. Wang and G.Z. Cao, "Developments in Nanostructured Vanadium Oxides for Advanced Li-Ion Rechargeable Batteries," *IEEE Nanotechnology Magazine* (June 2009), 14-20, (2009).
18. Q.F. Zhang, C. Dandeneau, X.Y. Zhou, and G.Z. Cao, "ZnO Nanostructures for Dye-Sensitized Solar Cells," (*Invited Review*), *Advanced Materials* **21**, 4087-4108 (2009).
19. D.W. Liu, Y.Y. Liu, B.B. Garcia, Q.F. Zhang, A.Q. Pan, Y.H. Jeong, and G.Z. Cao, "V<sub>2</sub>O<sub>5</sub>Xerogel Electrodes with Much Enhanced Lithium-ion Intercalation Properties after Annealing in N<sub>2</sub> Gas," *Journal of Materials Chemistry* **19**, 8789-8795 (2009).

#### **Taya's list of publications**

Mori, S., Nagata, M., i Nakahata. Y., Yasuta, K., Goto, R., Kimura, M., and Minoru Taya, 2010, "Enhancement of Incident Photon-to-Current Conversion Efficiency for Phthalocyanine-Sensitized Solar Cells by 3D Molecular Structuralization", *J. Amer. Chem. Soc. Communications*, 132, 4045-4055.

Nagata, M, Kimura, M and Taya, M, 2008, "Design of dye-sensitized solar cells with new light-harvesting dyes", *Electroactive Polymer Actuators and Devices (EAPAD) 2008*, edited by Yoseph Bar-Cohen, Proc. of SPIE Vol. 6927, 692718

Nagata, M., Baldwin, E., Kim, S.Y., Taya, M., 2012, Design of dye-sensitized solar cells integrated in composite panel subjected to bending, *Journal of Composite Materials* (Submitted, Jan. 2012 ) under review.

Kim, H.S., Kikuchi, K., Itoh, T., Iida, T. and Taya, M., 2012, "Design of segmented thermoelectric generator based on cost-effective and light-weight thermoelectric alloys", *J. Electronic Materials*. Under review.

#### **Kuga's list of publications**

Cha, J., Kuga, Y., Ishimaru, A. and Lee, S., 2007, "A 20 GHz steerable array antenna using 3-bit dielectric slab phase shifters on a coplanar waveguide," *IEEE Transactions on Antennas and Propagation*, Vol. 55, No. 2, pp. 290-7, February 2007.



Cha, J. and Kuga, Y., 2007, "A Steerable Phased-Array Antenna Using Mechanically Controllable 4-bit Dielectric Slab Phase Shifter on a Coplanar Waveguide at 24 GHz," *Microwave and Optical Technology Letters*, vol. 49, no. 12, pp. 3118-3122, 2007.

#### **Feraboli's Publications**

The following publications have been produced under the award funding.

Gasco F., Feraboli P., "Assessment of Manufacturing Limits and Process-Ability for Composite Structures with Embedded Energy Devices", Presented at the 18th International Conference on Composite Materials, August 21-26, 2011

F. Gasco, P. Feraboli, "Assessment of Manufacturing Limits and processability for composite structures with embedded energy devices", Japan International SAMPE Symposium and Exhibition (JISSE), Tokyo, Japan, Nov. 2011, Presenter: Feraboli

F. Gasco, P. Feraboli, "Assessment of Manufacturing Limits and processability for composite structures with embedded energy devices", American Society for Composites 26th Annual Technical Conference, Montreal, CAN, Sept. 2011, Presenter: Gasco.

Gasco F., Feraboli P., "Manufacturing process-ability of composite laminates with integrated thin film Li-ion batteries", *Journal of Composite Materials*, currently in submission

Gasco F., Feraboli P., "Electromechanical performance of composite laminates with integrated thin film Li-ion batteries", currently in preparation

#### **4.2 UCLA**

[1] T. Pereira, R. Scaffaro, S. Nieh, J. Arias, Z. Guo, and H. Thomas Hahn, "The performance of thin-film Li-ion batteries under flexural deflection," *Journal of Micromechanics and Microengineering*, vol. 16, p. 2714, 2006.

[2] Y. S. Ju, "Impact of interface resistance on pulsed thermoelectric cooling," *Journal of Heat Transfer*, vol. 130, p. 014502, 2008.

[3] T. Pereira, Z. Guo, S. Nieh, J. Arias, and H. T. Hahn, "Embedding thin-film lithium energy cells in structural composites," *Composites Science and Technology*, vol. 68, no. 7, pp. 1935–1941, 2008.

[4] T. Pereira, R. Scaffaro, Z. Guo, S. Nieh, J. Arias, and H. T. Hahn, "Performance of Thin-Film Lithium Energy Cells under Uniaxial Pressure," *Advanced Engineering Materials*, vol. 10, no. 4, pp. 393–399, 2008.

[5] H. S. Kim, S. R. Dhage, D. E. Shim, and H. T. Hahn, "Intense pulsed light sintering of copper nanoink for printed electronics," *Applied Physics A: Materials Science & Processing*, vol. 97, no. 4, pp. 791–798, 2009.

[6] H. S. Kim, J. S. Kang, J. S. Park, H. T. Hahn, H. C. Jung, and J. W. Joung, "Inkjet printed electronics for multifunctional composite structure," *Composites Science and Technology*, vol. 69, no. 78, pp. 1256–1264, 2009.

- [7] T. Pereira, Z. Guo, S. Nieh, J. Arias, and H. T. Hahn, "Energy storage structural composites: a review," *Journal of composite materials*, vol. 43, no. 5, pp. 549–560, 2009.
- [8] G. Cha and Y. S. Ju, "Reversible thermal interfaces based on microscale dielectric liquid layers," *Applied Physics Letters*, vol. 94, p. 211904, 2009.
- [9] G. Cha, Y. S. Ju, L. A. Ahur , and N. M. Wereley, "Experimental characterization of thermal conductance switching in magnetorheological fluids," *Journal of Applied Physics*, vol. 107, no. 9, p. 09B505–09B505, 2010.
- [10] K. Jason Maung, H. T. Hahn, and Y. S. Ju, "Multifunctional integration of thin-film silicon solar cells on carbon-fiber-reinforced epoxy composites," *Solar Energy*, vol. 84, no. 3, pp. 450–458, 2010.
- [11] J. S. Kang, H. S. Kim, J. Ryu, H. Thomas Hahn, S. Jang, and J. W. Joung, "Inkjet printed electronics using copper nanoparticle ink," *Journal of Materials Science: Materials in Electronics*, vol. 21, no. 11, pp. 1213–1220, 2010.
- [12] S. R. Dhage, H. S. Kim, and H. T. Hahn, "Cu (In, Ga) Se 2 Thin Film Preparation from a Cu (In, Ga) Metallic Alloy and Se Nanoparticles by an Intense Pulsed Light Technique," *Journal of electronic materials*, vol. 40, no. 2, pp. 122–126, 2011.
- [13] J. S. Kang, J. Ryu, H. S. Kim, and H. T. Hahn, "Sintering of Inkjet-Printed Silver Nanoparticles at Room Temperature Using Intense Pulsed Light," *Journal of electronic materials*, pp. 1–10, 2011.
- [14] J. Ryu, H. S. Kim, and H. T. Hahn, "Reactive sintering of copper nanoparticles using intense pulsed light for printed electronics," *Journal of Electronic Materials*, vol. 40, no. 1, pp. 42–50, 2011.
- [15] T. Saotome, H. Kim, D. Lashmore, and H. Thomas Hahn, "Transparent conducting film: Effect of mechanical stretching to optical and electrical properties of carbon nanotube mat," *Bulletin of Materials Science*, vol. 34, no. 4, pp. 615–622, 2011.
- [16] T. Saotome, K. Kokubo, S. Shirakawa, T. Oshima, and H. T. Hahn, "Polymer nanocomposites reinforced with C60 fullerene: effect of hydroxylation," *Journal of Composite Materials*, vol. 45, no. 25, pp. 2595–2601, 2011.
- [17] K. E. Bulgrin, Y. S. Ju, G. P. Carman, and A. S. Lavine, "An Investigation of a Tunable Magnetomechanical Thermal Switch," *Journal of Heat Transfer*, vol. 133, no. 10, p. 101401, 2011.
- [18] H. S. Kim, Y. M. Lee, S. Dhage, J. S. Kang, and H. T. Hahn, "NANOCOMPOSITES FOR POWER LAMINATES."



- [19] J. S. Kang, H. S. Kim, Y.M. Lee, and H. T. Hahn, "Analysis on Performances of Lithium-Ion Polymer Battery for Unmanned Aircraft System," *Composites Science and Technology* (submitted)
- [20] Y. Zhan, G. Cha, J. Zhuang, Y. Jia, and Y. S. Ju, "Microscale liquid-based mechanical elements for multi-functional integration," *Journal of Composite Materials* (submitted).

#### **4.3 University of Colorado Publications**

- Rupp, C. J., Dunn, M. L., and Maute, K., 2010, "Analysis of Piezoelectric Energy Harvesting Systems with Non-linear Circuits Using the Harmonic Balance Method," *Journal of Intelligent Materials and Structures*, Vol. 2, pp. 1383-1396.
- Rupp, C. J., Maute, K., and Dunn, M. L., 2010, "Switchable Phononic Devices via Wave Filtering and Guiding in Polarization-Patterned Piezoelectric Solids," *Applied Physics Letters*, Vol. 96, Paper No. 111902.
- Rupp, C. J., Evgrafov, A., Maute, K., and Dunn, M. L., 2009, "Design of Piezoelectric Energy Harvesting Systems: A Topology Optimization Approach Based on Multilayer Plates and Shells," *Journal of Intelligent Materials and Structures*, Vol. 20, pp. 1923-1939.
- Evgrafov, A., Rupp, C. J., Dunn, M. L., and Maute, K., 2008, "Optimal Synthesis of Tunable Elastic Waveguides," *Computer Methods in Applied Mechanics and Engineering*, Vol. 198, pp. 292-301.
- Rupp, C. R. Evgrafov, A., Maute, K., and Dunn, M. L., 2008, "Optimal Design of Piezoelectric energy Harvesters Based on Multilayer Plates and Shells," in *Proceedings of the ASME Conference on Smart Materials, Adaptive Structures and Intelligent Systems*.
- Rupp, C. J., Evgrafov, A., Dunn, M. L., and K. Maute, "Large-Scale Topology Optimization of Phononic Meta-Materials for Surface Wave Devices," in *Proceedings of 7th World Congress on Structural and Multidisciplinary Optimization*, May 21-25, 2007, Seoul, Korea. (Selected as Finalist for Best Paper Award)
- S. Golmon, K. Maute, and M.L. Dunn. Multi-Scale Design Optimization of Lithium Batteries using Adjoint Sensitivity Analysis. *International Journal for Numerical Methods in Engineering*, in press, 2012.
- S. Golmon, C. DeLuca, M.L. Dunn, and K. Maute. Multi-scale Modeling and Optimization of Structurally Integrated Lithium-Ion Batteries. *Proceedings of the 18<sup>th</sup> International Conference on Composite Materials*, August 21-26, 2011, Jeju, Korea, 2011.
- K. Aifantis, K. Maute, M.L. Dunn, S. Hackney. Mechanics of Materials for Li-Battery Systems. Chapter 8 in *High Energy Density Lithium Batteries*, Weinheim: Wiley-Vch, 2010.
- S. Golmon, K. Maute, and M.L. Dunn. Numerical Modeling of Electrochemical-Mechanical Interactions in Lithium Polymer Batteries. *Computers & Structures*, 87:1567-1579, 2009.

## **Chapter 5. Interactions with DoD lab and industry**

### **a) DoD labs**

Taya of UW visited J. Thomas of Naval Research Laboratory to discuss the thermoelectric generator mounted on a small-sized UAV.

CU team interact with G. Reich, Adaptive Structures, Vehicles Directorate, AFRL, Dayton, OH.

### **b) DoD industry**

Taya of UW discussed with Bradley J Mitchell, Boeing Company, regarding possible technology transfer of the thermoelectric generator to Boeing commercial airplanes.

Taya gave a talk at GM headquarters on Energy-harvesting system including airborne applications

## **Chapter 6. Honors/awards**

Keynote Address: K. Maute and M.L. Dunn, 2012 Society of Engineering Science Annual Meeting, Atlanta, GA.

T. Hahn, World Fellow, International Committee on Composites, July 2009

T. Hahn, Scala Lecturer, International Committee on Composites, August 2011



## Chapter 7 References

- Aizawa, T., and Song, R., 2006, "Mechanically induced reaction for solid-state synthesis of  $\text{Mg}_2\text{Si}$  and  $\text{Mg}_2\text{Sn}$ ", *Intermetallics*, 14, 382-391
- Bates J.B., Dudney N.J., Gruzalsky G.R., Zuhr R.A., Choudhury A., Luck C.F., Robertson J.D., 1992, "Electrical properties of amorphous lithium electrolyte thin films", *Solid State Ionics*, 53-56, pp. 647-654
- Bates J.B., Dudney N.J., Neudecker B., Ueda A., Evans C.D., 2000, "Thin film lithium and lithium-ion batteries", *Solid State Ionics*, 135, pp. 33-45
- Bates J.B., Dudney N.J., Neudecker B.J., Hart F.X., Jun H.P., Hackhey S.A., 2000, "Preferred orientation of Polycrystalline  $\text{LiCoO}_2$  films" *Journal of the Electrochemical Society*, 147/1, pp. 59-70
- Chan C.K., Peng H., Liu G., McIlwrath K., Zhang X.F., Huggins R.A., Cui Yi, 2008, "High performance lithium battery anodes using silicon nanowires", *Nature Nanotechnology* 3, pp. 31 – 35
- Crane, D., Kossakovski, D., Bell, L., 2009, "Modeling the building blocks of a 10% efficient segmented thermoelectric power generator". *J Electron Mater* 38, 1382-1386
- D'Angelo, J., Case, E., Matchanov, N., Wu, C.I., Hogan, T., Barnard, J., Cauchy, C., Hendricks, T., Kanatzidis, M., 2011, "Electrical, thermal, and mechanical characterization of novel segmented-leg thermoelectric modules", *J Electron Mater* 40, 2051-2062
- El-Genk, M.S., Saber, H.H., Caillat, T., Sakamoto, J., 2006, "Tests results and performance comparisons of coated and un-coated skutterudite based segmented uniconouples", *Energy Convers Manage* 47, 174-200
- Fthenakis, V.M., 2009, "Sustainability of photovoltaics: The case for thin-film solar cells", *Renewable and Sustainable Energy Reviews*, Vol. 13, pp. 2746-2750
- Gallone G., Capaccioli S., Levita G., Rolla P., Corezzi S., 2001, "Dielectric analysis of the linear polymerization of an epoxy resin", *Polymer International*, 50, pp. 545-551
- Goldsmid, H.J., 1964, "Thermoelectric refrigeration", Plenum Press, New York
- Gu, Y.F. et al., 2002, "Microstructures and fracture behaviors of B-free and B-doped  $\text{Ir}_3\text{Nb}$  (L12) intermetallic compounds", *Mater. Sci. Eng.*, A329-331, 262-267
- Halman, T.C., Taylor, P.J. et al., 2002, "Quantum Dot Superlattice Thermoelectric Materials and Devices", *Science*, 297, 2229-2232
- Heikes, R.R., Ure, R.W., 1961, "Thermoelectricity: science and engineering", Interscience Publishers
- Hsu, K.F., Loo, S. et al., 2004, "Cubic  $\text{AgPbmSbTe}_{2+m}$ : Bulk Thermoelectric Materials with High Figure of Merit", *Science*, 303, 818-821
- Hutchinson, J.W., Suo, Z., 1992, "Mixed-mode cracking in layered materials", *Advances in Applied Mechanics*, Vol. 29, pp. 63-191

- Krasnov V., Nieh K. Li J., 2011, "Thin film battery and manufacturing method", US Patent No. 7862927.
- Krasnov V., Nieh K., Ting S., Tang P., Chang F., Lin C., 2005, "Sputter deposition of lithium phosphorous oxynitride material", US Patent No. 6863699
- Kulkarni, A.P., Zhu, Y., Babel, A., Wu, P.T. and Jenekhe, S.A., 2008, "New Ambipolar Organic Semiconductors. 2. Effects of Electron Acceptor Strength on Intramolecular Charge Transfer Photophysics, Highly Efficient Electroluminescence, and Field-Effect Charge Transport of Phenoxazine-Based Donor-Acceptor Materials." *Chem. Mater.* 20, 4212-4223.
- Liu E., Sherman E., Jacobsen A., 2008, "Design and fabrication of multifunctional structural batteries", *Journal of Power Sources*, 189/1, pp. 646-650.
- Liu Y., Taya M., 2009, "Electrospinning fabrication and electrochem prop of LiCo nanofibers li batt cathode", *Active and Passive Smart Structures and Integrated Systems*, Proc. Of SPIE Vol. 7288, pp. 728806 1-7
- Lotka. A.J., 1923, "Note on the relative abundance of the elements in the Earth's crust", *Proc Natl Acad Sci USA* 9, 87- 90
- Nagasubramanian G., Doughty D.H., 2004, "Electrical characterization of all-solid-state thin film batteries", *Journal of Power Sources*, 136, pp. 395-400
- Noda, Y., Kon, H., Furukawa, Y., Otsuka, N., Nishida, O.A., and Masumoto, K., 1992, "Preparation and thermoelectric properties of  $\text{Mg}_2\text{Si}_{1-x}\text{Ge}_x$  ( $x=0.0\sim0.4$ ) solid solution semiconductors", *Materials Transactions, JIM*, 33, 845-850
- Pereira T., Scaffaro R., Nieh S., Arias J., Guo Z., Hahn H.T., 2006, "The performance of thin-film Li-ion batteries under flexural deflection", *Journal of Micromechanics and Microengineering*, 16, pp. 2714-2721
- Pereira T., Scaffaro R., Nieh S., Arias J., Hahn H.T., 2008(a), "Performance of thin-film Lithium Energy cells under uniaxial pressure", *Advanced Engineering Materials*, 10/4, pp. 393-399
- Pereira T., Scaffaro R., Nieh S., Arias J., Hahn H.T., 2008(b), "Embedding thin-film lithium energy cells in structural composites", *Composites Science Technology*, 68/7-8, pp. 1935-1941
- Pereira T., Scaffaro R., Nieh S., Arias J., Hahn H.T., 2009, "Energy storage structural composites: a review", *Journal of Composite Materials*, 43/5, pp. 549-560
- Pogue, W.R., Baucom, N.J., Thomas, J.P., Qidwai, M.A., 2005, "Structure-power system for unmanned air vehicles". *Proc AUVSI Unmanned Systems North America*, Baltimore, MD, 1155-1169
- Riffel, M. and Schilz, J., 1998, "Mill setting and microstructural evolution during mechanical alloying of  $\text{Mg}_2\text{Si}$ ", *J Mater Sci*, 33, 3427-3431
- Roth E.P., Doughty D.H., 2003, "Thermal abuse performance of high-power 18650 Li-ion cells", *Journal of Power Sources*, 128, pp. 308-318



- Sales, B.C., Mandrus, D. et al., 1996, "Filled Skutterudite Antimonides: A New Class of Thermoelectric Materials", *Science*, 272, 1325-1328
- Saqr, K., Mansour, M., Musa, M., 2008, "Thermal design of automobile exhaust based thermoelectric generators: Objectives and challenges". *Int J Automot Technol* 9, 155-160
- Scott I.D., Jung Y.S., Cavanagh A.S., Yan Y., Dillon C.A., George S.M., Lee S.H., 2011, "Ultrathin coatings on nano-LiCoO<sub>2</sub> for Li-ion vehicular applications", *Nano Letters*, 11, pp. 414-418
- Snyder J.F., Carter R.H., Wetzel E.D., 2007, "Electrochemical and mechanical behavior in mechanically robust solid polymer electrolytes for use in multifunctional structural batteries", *Chemistry of Materials*, 19/3, 2007, pp. 3793-3801.
- Snyder J.F., Wetzel E.D., Watson C.M., 2009(a), "Improving multifunctional behavior in structural electrolytes through copolymerization of structure- and conductivity-promoting monomers", *Polymer*, 50, pp. 4906-4916
- Snyder J.F., Wong E.L., Hubbard C.W., 2009(b), "Evaluation of commercially available carbon fibers, fabrics and papers for potential use in multifunctional energy storage applications", *Journal of the Electrochemical Society*, 156/3, 2009, pp. 215-224
- Son S.B., Trevey J.E., Roh H., Kim S.H., Kim K.B., Cho J.S., Moon J.T., DeLuca C.M., Maute K.K., Dunn M.L., Han H.N., Oh K.H., Lee S.H., 2011, "Microstructure study of electrochemically driven Li<sub>x</sub>Si", *Advanced Energy Materials*, 1, pp. 1199-1204
- Taya, M., Kim, H.S., 2011, AFOSR MURI annual report, Washington DC
- Timoshenko, S., 1925, "Analysis of bi-metal thermostats", *J. Opt. Soc. Am*, Vol. 11, pp. 233-256
- Thomas J.P., Qidwai M.A., P. Matic P, Everett R.K, 2002, "Multifunctional structure-plus-power concepts", 43rd AIAA/ASME/ASCE/AHS/ASC Structures, Structural Dynamics, and Materials Conference, Apr. 2002, Denver, CO.
- Thomas J.P., Qidwai M.A., 2004, "Mechanical design and performance of composite multifunctional materials", *Acta Materialia*, 52, pp. 2155-64.
- Thomas J.P., Qidwai M.A., 2005, "The design and application of multifunctional structure-battery material systems", *Journal of the Minerals, Metals and Materials Society*, 57/3, pp. 18-24.
- Thomas E.V., Case H.L., Doughty D.H., Jungst R.G., Nagasubramanian G., Roth E.P., 2003, "Accelerated power degradation of Li-ion cells", *Journal of Power Sources*, 124, pp. 254-260
- Trevey J.E., Wang J., DeLuca C.M., Maute K.K., Dunn M.L., Lee S.H., Bright V.M., 2011, "Nanostructured silicon electrodes for solid-state 3-d rechargeable lithium batteries", *Sensors and Actuators A: Physical*, 167, pp. 139-145
- Qidway M.A., Baucom J.N., Thomas J.P., Horner D.M., 2005, "Multifunctional Applications of thin film Li polymer battery cells", *Material Science Forum*, 492-493, pp. 157-162 .

- Yu, C., Chau, K.T., 2009, "Thermoelectric automotive waste heat energy recovery using maximum power point tracking". *Energy Convers Manage* 50, 1506-1512
- Van Sluytman J.S., West W.C., Whitacre J.F., Alamgir F.M., Greenbaum S.G., 2006, "Cycling-induced degradation of LiCoO<sub>2</sub> thin-film cathodes at elevated temperature", *Electrochimica Acta*, 51, pp. 3001-3007
- Venkatasubramanian, R., Siivola, E. et al., 2001, "Thin-film thermoelectric devices with high room-temperature figures of merit", *Nature*, 413, 597-602
- Volinsky, A.A., 2003, "Experiments with In-situ Thin Film Phone Cord Delamination Propagation", *Materials Research Society Symposia Proceedings*, Vol. 749, W10.7
- Wang Y., Cao G., 2008, "Developments in nanostructured cathode materials for high-performance lithium-ion batteries", *Advanced Materials*, 20, pp. 2251-2269
- West W.C., Whitacre J.F., White V., Ratnakumar B.V., 2002, "Fabrication and testing of all solid-state microscale lithium batteries for microspacecraft applications", *Journal of Micromechanics and Microengineering*, 12, pp. 58-62
- Xu C., Ma C., Taya M, 2008, "Electrolyte for Laminated Polymer Lithium Rechargeable Battery", *Electroactive Polymer Actuators and Devices (EAPAD)*, Proc. Of SPIE Vol. 6927, pp. 692714 1-9
- Zhang, Q., Chou, T.P., Russo, B., Jenekhe, S.A, and Cao, G., 2008, " Aggregation of ZnO Nanocrystallites for High Conversion Efficiency in Dye-Sensitized Solar Cells,"*Angewandte Chemie International Edition* 47, 2402 –2406
- Zhu, Y.,Champion, R. D., Jenekhe, S. A. 2006, "Conjugated Donor–Acceptor Copolymer Semiconductors with Large Intramolecular Charge Transfer: Synthesis, Optical Properties, Electrochemistry, and Field Effect Carrier Mobility of Thienopyrazine-Based Copolymers." *Macromolecules* 39, 8712-8719.
- Zhu, Y.,Kulkarni, A. P., Wu, P.-T., Jenekhe, S. A.2008, "New Ambipolar Organic Semiconductors. 1. Synthesis, Single-Crystal Structures, Redox Properties, and Photophysics of Phenoxazine-Based Donor–Acceptor Molecules." *Chem. Mater.* 20, 4200-4211.



PI Name Daniel M. Neumark

Agency AFOSR

Project Year Start Date

Year One  
4/1/2016

Total

**Senior Personnel - Faculty**

Choose Acad. Yr. or Summer in the cell to the right

Summer Salary

0.00	0.00	0.00%	0	0	0
<b>Total Senior Personnel</b>				<b>0</b>	<b>0</b>

**Other Personnel**

<b>A. Total Salaries and Wages</b>	<b>0</b>	<b>0</b>
------------------------------------	----------	----------

**Benefits**

<b>B. Total Benefits Incl. Tuition</b>	<b>0</b>	<b>0</b>
--	----------	----------

<b>A. + B. Total Salaries and Benefits</b>	<b>0</b>	<b>0</b>
--	----------	----------

**Equipment**

Equipment	0	0
-----------	---	---

Fabricated Equipment	0	0
----------------------	---	---

<b>C. Equipment</b>	<b>0</b>	<b>0</b>
---------------------	----------	----------

**Travel**

Domestic	0	0
----------	---	---

Foreign	9,554	9,554
---------	-------	-------

<b>D. Travel</b>	<b>9,554</b>	<b>9,554</b>
------------------	--------------	--------------

**Other Direct Costs**

7. Other Direct Costs	0	0
-----------------------	---	---

<b>G. Total Other Direct Costs</b>	<b>0</b>	<b>0</b>
------------------------------------	----------	----------

<b>H. Total Direct</b>	<b>9,554</b>	<b>9,554</b>
------------------------	--------------	--------------

**Indirect Costs**

Modified total direct (BASE)	9,554	9,554
------------------------------	-------	-------

Indirect Cost	5,446	5,446
---------------	-------	-------

<b>I. Total Indirect Cost</b>	<b>5,446</b>	<b>5,446</b>
-------------------------------	--------------	--------------

<b>H. + I. Total Direct and Indirect</b>	<b>15,000</b>	<b>15,000</b>
--	---------------	---------------

 Cora  
BASADA

Contract and Grant Officer  
Sponsored Projects Office